Title
Manipulation Of Electron-Transfer Dynamics Of Nanoparticles Functionalized With Conjugated Metal-Ligand Bonds

Author
Hu, Peiguang

Publication Date
2016

UNIVERSITY OF CALIFORNIA
SANTA CRUZ

MANIPULATION OF ELECTRON-TRANSFER DYNAMICS OF NANOPARTICLES FUNCTIONALIZED WITH CONJUGATED METAL–LIGAND BONDS

A dissertation submitted in partial satisfaction
of the requirements for the degree of

DOCTOR OF PHILOSOPHY

in

CHEMISTRY

by

Peiguang Hu

September 2016

The Dissertation of Peiguang Hu
is approved:

_____
Professor Shaowei Chen, Chair

_____
Professor Ilan Benjamin

_____
Professor Scott Oliver

_____
Tyrus Miller
Vice Provost and Dean of Graduate Studies

Table of Contents

List of Figures

Chapter 1

Chapter 2

Chapter 3

Chapter 4

Chapter 5

Chapter 6

Chapter 7

List of Tables

Chapter 5

Chapter 7

MANIPULATION OF ELECTRON-TRANSFER DYNAMICS OF NANOPARTICLES FUNCTIONALIZED WITH CONJUGATED METAL–LIGAND BONDS

Peiguang Hu

Abstract

Noble metal nanoparticles represent a large class of functional nanomaterials with unique physical and chemical properties that are significantly different from those of their atomic or bulk forms. Traditionally, nanoparticle surface functionalization has been achieved by using mercapto derivatives as the ligands of choice by forming metal–thiolate covalent linkages, but such interfacial linkages lack interesting chemistry. In recent years, metal–carbon covalent bonds have been explored for surface functionalization of noble metal nanoparticles with the formation of, for instance, metal–carbon (sp^2 hybridized) single bond (M–Csp^2), metal–carbene (M=C), metal–acetylide (M–C≡C)/metal–vinylidene (M=C=C) bonds.

Because of the conjugated metal–carbon interfacial bonds, the resistance at the metal–ligand interface is significantly reduced, and intraparticle charge delocalization between the particle-bound functional moieties occurs, leading to the emergence of new optical and electronic properties that are analogous to those of their dimeric counterparts. More importantly, such electronic communication may be further manipulated by modifying the electronic structures of the nanoparticle cores and enabling specific interactions between the organic ligand shells and selective molecules/ions in local chemical environment. The fundamental insights may be

further developed for sensitive chemical/biological sensing as well as electrocatalysts in fuel cell electrochemistry with enhanced performance.

Within this thesis, detailed discussion will be focused on metal nanoparticles functionalized with alkyne and alkene derivatives with respect to their interfacial structure, manipulation of intraparticle charge delocalization, and futher exploration as electrocatalysts for oxygen reduction reaction (ORR).

By comparing the deuterium labelled platinum nanoparticles (PtDC12, stabilized with dodec-1-deuteroyne) with the unlabeled counterparts (PtHC12, capped by 1-dodecyne), the interfacial bonds at the metal–ligand interface of alkyne-functionalized metal nanoparticles have been identified as the Pt–vinylidene (Pt=C=C) bonds dominated rather than Pt–acetylide (Pt–C≡C) + platinum-hydride (Pt–H) bonds .

The manipulation of intraparticle charge delocalization was achieved for acetylene derivatives functionalized platinum nanoparticles. 4-Enthynylpheynyl boronic acid pinacol ester functionalized platinum nanoparticles (Pt–EPBAPE) were found to exhibit apparent photoluminescence due to the particle-bound acetylene moieties that behaved analogously to their dimeric derivatives. More importantly, the nanoparticle photoluminescence can be selectively modified with fluoride ions by forming B–F bonds, indicating the effective manipulation of the intraparticle charge delocalization within the Pt–EPBAPE nanoparticles by the local chemical environment. The manipulation of intraparticle electronic communication has also been accomplished by deliberately tuning the metal core size. This was demonstrated with spectroscopic and electrochemical studies of two types of ethynylferrocene

functionalized platinum nanoparticles with different sizes of the metal cores ($Pt_{314}eFc$ and $Pt_{10}eFc$, with metal core consisting of about 314 and 10 platinum atoms, respectively). As the particle size increased, infrared measurements showed a more pronounced red-shift of the C≡C/=C=C and ferrocenyl =C−H vibration bands, and electrochemical measurements demonstrated enhanced intervalence charge transfer by displaying two pairs of voltammetric peaks with a larger potential spacing. This strongly suggests the enhanced (weakened) intraparticle charge delocalization with increasing (decreasing) particle size, which can be accounted for by the different conductivity of the metal cores. Furthermore, $Pt_{10}eFc$ exhibited improved intervalence charge transfer under UV photoirradiation because of enhanced Pt_{10} core (semiconductor-like) conductivity, while no such effect was observed for the $Pt_{314}eFc$ (metal-like) sample.

Alkene derivatives were explored as new ligands of choice for platinum nanoparticle functionalization by self-assembly. It was first demonstrated with 1-octadecene functionalized Pt nanoparticles (PtODE). The Pt−acetylide (Pt−C≡C)/Pt−vinylidene (Pt=C=C) bonds were identified as one form of the interfacial interactions as a result of dehydrogenation and transformation of the olefin moieties catalyzed by platinum. This is suggested by the spectroscopic results showing apparent photoluminescence characteristics and a red-shift of the C≡C/=C=C vibration bands, similar with those of alkyne-functionalized platinum nanoparticles. This was then further confirmed with the selective reactivity of the nanoparticles with imine derivatives that was specific to Pt−acetylide (Pt−C≡C)/Pt−vinylidene (Pt=C=C) bonds,

as manifested by NMR and electrochemical measurements. Further X-ray absorption near-edge spectroscopy (XANES) suggested the Pt–ligand interfacial bonds were in intermediate between those of Pt–C≡C/Pt=C=C and Pt–Csp^2. The *para*-substituents effects were then examined by using *para*-substituted styrene derivatives (4-*tert*-butylstyrene, 4-methoxystyrene, and 4-(trifluoromethyl)styrene) functionalized platinum nanoparticles (PtTBS, PtMOS, and PtTFMS, respectively). The nanoparticle core size increases in the order of PtTFMS < PtMOS < PtTBS due to the reduced dehydrogenation rate with the decreasing Taft (polar) constants of the *para*-substituents. Apparent photoluminescence was also observed for all three nanoparticles, ascribed to the effective intraparticle delocalization between particle-bound functional moieties. More importantly, the emission peaks were found red-shifted with decreasing Hammett constant of the *para*-substituents. Additionally, electrochemical measurements suggested the PtTBS nanoparticles exhibited the best performance as ORR electrocatalysts, which may be accounted for by the optimal combination of the nanoparticle core size and ligand effects on the oxygen affinity of Pt metal cores.

A series of 1-dodecyne functionalized AgAu alloy nanoparticles with varied Ag/Au ratios were also synthesized and evaluated as electrocatalysts for ORR. The alloy nanoparticles exhibited a core size in the range of 3–5 nm with gold concentrations varied from 25 at% to 55 at%. The successful surface functionalization of 1-dodecyne was confirmed with IR measurements. Electrochemical studies displayed that all samples showed apparent catalytic activity for ORR in alkaline media, which was much enhanced compared with pure Ag catalysts, and the best performance

was observed from the one containing 35.5 at% gold, which was even comparable to that of commercial Pt/C catalysts. The improved electrocatalytic activity was accounted for by the enhanced oxygen affinity of the AgAu nanoparticles due to the alloy effect and an optimal affinity led to the best catalytic performance in the series.

DEDICATION

Dedicated

To

My Family

ACKNOWLEDGEMENTS

I would like to first express my appreciation to my advisor, Professor Shaowei Chen. Without him, I would not be able to join this lab, complete this thesis and finally obtain my PhD degree. Professor Chen always shares his research experience, instructs me with my research projects, encourages and inspires me to come up with my own research ideas. I have also benefited tremendously from his great suggestions and comments for my research, which significantly better my work. More importantly, Professor Chen also shared with me about his life experience, and provided advice for my future career.

I would also like to thank Professor Ilan Benjamin and Professor Scott Oliver to serve on my dissertation committee and offer support over my graduate career and during my job hunting. I also appreciate help and support from Professor Jinzhong Zhang and Professor Yat Li in the past years.

I also want to thank all of my labmates, Professor Zhiyou Zhou, Professor Jie Huang, Professor Yan Guo, Professor Yinghui Ren, Professor Fen Ran, Dr. Xiaoqin Niu, Professor Tizhuang Wang, Professor Fanli Lu, Professor Xiaohua Fan, Professor Weihua Yang, Dr. Xiongwu Kang, Dr. Yang Song, Dr. Guoqiang He, Dr. Chan Lin, Dr. Bruce Phebus, Dr. Ke Liu, Dr. Christopher Deming, Limei Chen, Mauricio Rajas-Andrade, Samantha Sweeney, Gabby Lu, Yi Peng, John Diniz, Rene Mercado, Gustavo Chata, Bingzhang Lu, Shannon Lee, Lewis Bonny, Stanley Chan and all the undergraduate student and high school student researchers. Special thanks to Dr. Xiongwu Kang and Dr. Yang Song, who helped me with my study and life when I

started in UC Santa Cruz, and had discussion with me on research from which I learned a lot, to Professor Yan Guo and Professor Yinghui Ren, who I collaborated with and accomplished our projects together, to my undergraduate student researchers, Shannon Lee, Lewis Bonny and Stanley Chan, who offered a great helping hand in my research.

I have to express my thanks to Paul Duchesne and Professor Peng Zhang from Dalhousie University, Canada, for contributing to my research by providing X-ray Absorption Spectroscopy measurements and analysis.

Many thanks to my friends from Professor Yat Li and Professor Jinzhong Zhang's lab, Xihong Lu, Gongming Wang, Feng Luan, Yichuan Ling, Hanyu Wang, Ying-Chih Pu, Yi Yang, Tianyi Kou, Tianyu Liu, Teng Zhai, Yang Yang, Feng Zhang Binbin Luo.

Last but not the least, I really want to thank my family. My parents raised me up with all their love, and without their encouragement and support I would never be able to achieve anything. I also would like to thank my wife, Limei Chen, who has been accompanying and supporting me for the past few years as labmate, friend, and partner.

The text of this dissertation includes reprints of the following previously published material:

Chapter 1: Peiguang Hu, Limei Chen, Xiongwu Kang, Shaowei Chen, "Surface Functionalization of Metal Nanoparticles by Conjugated Metal-Ligand Interfacial Bonds", submitted.

Chapter 2: Peiguang Hu, Limei Chen, Christopher P. Deming, Lewis W. Bonny, Hsiau-Wei Lee, Shaowei Chen, "Identification of the formation of metal–vinylidene

interfacial bonds of alkyne-capped platinum nanoparticles by isotopic labelling", in revision.

Chapter 3: Peiguang Hu, Yang Song, Mauricio Daniel Rojas-Andrade, Shaowei Chen, "Platinum Nanoparticles Functionalized with Ethynylphenylboronic Acid Derivatives: Selective Manipulation of Nanoparticle Photoluminescence by Fluoride Ions", *Langmuir*, **2014**, *30*, 5224–5229.

Chapter 4: Peiguang Hu, Limei Chen, Christopher P. Deming, Xiongwu Kang, Shaowei Chen, "Nanoparticle-Mediated Intervalence Charge Transfer: Core-Size Effects", *Angew. Chem. Int. Ed.* **2016**, *128*, 1477–1481.

Chapter 5: Peiguang Hu, Paul N. Duchesne, Yang Song, Peng Zhang, Shaowei Chen, "Self-Assembly and Chemical Reactivity of Alkenes on Platinum Nanoparticles", *Langmuir*, **2015**, *31*, 522–528.

Chapter 6: Peiguang Hu, Limei Chen, Christopher P. Deming, Jia-En Lu, Lewis W. Bonny, Shaowei Chen, "Effects of para-substituents of styrene derivatives on their chemical reactivity on platinum nanoparticle surfaces", *Nanoscale*, **2016**, *8*, 12013-12021.

Chapter 7: Peiguang Hu, Yang Song, Limei Chen, Shaowei Chen, "Electrocatalytic activity of alkyne-functionalized AgAu alloy nanoparticles for oxygen reduction in alkaline media", *Nanoscale*, **2015**, *7*, 9627–9636.

The co-author, Shaowei Chen, listed in the publications directed and supervised the research which forms the basis for the dissertation.

Chapter 1

Introduction

Adapted with permission from (Peiguang Hu, Limei Chen, Xiongwu Kang, Shaowei Chen, "Surface Functionalization of Metal Nanoparticles by Conjugated Metal-Ligand Interfacial Bonds"), submitted.

1.1 Background

Nanomaterials refer to materials with any external dimension in the regime of 1 to 100 nanometers (nm, 10^{-9} meter). It is well known that nanomaterials exhibit significantly different properties due to the surface effects (which means a high surface-volume ratio and low coordination numbers) and quantum confinement effect.[5] Thanks to the new properties, nanomaterials have been attracting plenty of attention from researchers, and a variety of technologies and strategies have been explored and developed for the design, preparation, and applications of nanomaterials.

One important class of nanomaterials is noble metal nanoparticles. Noble metal nanoparticles display unique physical and chemical properties which are significantly different from those of their atomic or bulk counterparts and thus noble metal nanoparticles have been used in diverse applications in sensing, catalysis, imaging, biology, medicine, and therapy, etc.[6, 11-27] For example, localized surface plasmon resonances (LSPR) can occur on noble metal (like Ag, Au) nanoparticles (a.k.a., plasmonic nanoparticles), which is largely controlled by the composition, size, and shape of the nanoparticles. LSPR induces strong absorption and scattering at a specific wavelength of light and strong electromagnetic near-field enhancements, which have been exploited for the development of chemical sensors by monitoring the variation of the spectroscopic responses as results of the interactions between target molecules and the plasmonic nanoparticles.[28, 29] Another example is that noble metal nanoparticles are promising catalyst candidates for various reactions, which are mainly due to the significantly large surface areas with abundant highly reactive sites as well as the ease

of recycle with good retention of the catalytic activity. Moreover, the catalytic activity of noble metal nanoparticles can be further manipulated by controlling the size, shape, and composition.[30, 31] However, surface modification is still necessary to further manipulate the nanoparticle properties, which may be achieved by inorganic coating or functionalization with organic ligands.

Organically capped noble metal nanoparticles have been attracting extensive interests in at least three aspects which are to stabilize nanoparticles from agglomeration, to render the nanoparticles compatible with different phases, and to enable the self-organization of nanoparticles.[32] Of these, mercapto derivatives have been used extensively as the ligands of choice for nanoparticle surface functionalization with the formation of metal−thiolate (M−S) interfacial bonds, and the nanoparticle materials properties have been found to be readily manipulated by the chemical nature of the metallic cores as well as the organic capping ligands.[33, 34] However, the impacts of the metal−ligand interfacial contact on the mercapto derivatives-functionalized metal nanoparticles have been largely ignored due to the lack of interesting chemistry of the metal−thiolate bond.

It is well known that strong interactions can be formed between noble metals and carbon based molecules. For example, organometallic complexes have been widely synthesized in organometallic chemistry.[35] By taking the advantage of the d orbitals, transition metals are able to bind to carbons and generate various M−C bonds, including metal−carbon (sp^2) bond, metal−olefin bond, metal−carbene bond, metal−carbyne bond, and metal−carbide bond.[35-37] In addition, the adsorption of the hydrocarbons

on clean metal surfaces has also been well studied.[38-41] The adsorbed hydrocarbon molecules may form π or σ M−C bonds with the metal surface atoms, and the generated moieties may undergo dehydrogenation and/or rearrangement to form varied M−C covalent bonds.[38-41] Furthermore, the generated M−C covalent bonds could be as strong as the M−S linkage. For example, the binding energy for the Pd−C single covalent bond was evaluated to be 436 kJ mol^{-1}, which is even higher than that for the Pd−S bond (380 kJ mol^{-1}).[42] Therefore, it is reasonable to imagine that noble nanoparticles can be stabilized with a variety of metal−carbon covalent bonds.

In the past few years, noble metal nanoparticles have been shown to be functionalized with various metal−carbon covalent bonds.[4, 43-46] These include metal−carbon (sp^2 hybridized) single bonds (M−Csp^2), metal−carbene bonds (M=C), and metal−acetylide (M−C≡C)/metal−vinylidene (M=C=C) bonds.[4, 43-46] The unique interfacial linkages endow the nanoparticles with unprecedented optical, electronic and electrochemical properties. For examples, with the metal−carbon covalent bonds, the formed nanoparticles exhibit significantly reduced interfacial resistance;[47-49] the conjugated metal−ligand interfacial bonds enable the extensive intraparticle charge delocalization so that the nanoparticle-bound functional moieties behave analogously to their dimeric counterparts;[2, 4, 10, 50] significantly, when multiple functional moieties are incorporated onto the same nanoparticle surface, the electronic interactions occurs between the various functional moieties, which may be exploited as a unique variable in gating intraparticle charge transfer,[3, 9, 51] a

platform that has the potential for chemical sensing of specific molecules/ions[6, 52] as well as deliberate manipulation of nanoparticle electrocatalytic activity in fuel cell electrochemistry.[23-27, 43, 53]

Within this context, the principal objectives of this dissertation are to identify the formation of the metal-vinylidene interfacial bonds at the interface of noble metal nanoparticles functionalized by intact terminal alkyne derivatives, explore new organic ligands (alkene derivatives) to passivate noble metal nanoparticles, and study the manipulation of electron-transfer dynamics of these nanoparticles.

1.2 Noble metal nanoparticles passivated with metal–carbon covalent bonds

As mentioned above, recent studies have shown that noble metal nanoparticles could be functionalized with a wide variety organic ligands by forming metal–ligand bonds at the interface, including metal–carbon (sp^2) single bonds (M–Csp^2, Scheme 1A), metal=carbene bonds (M=C, Scheme 1B), metal–acetylide bonds (M–C≡C, Scheme 1C) and metal–acetylide/metal–vinylidene bonds (M–C≡C/M=C=C, Scheme 1D).[4, 43-46, 54-57] This is mainly motivated by previous studies for metalorganic complexes and the adsorption of hydrocarbons on clean metal surfaces.[35, 38-41] The metal–carbon bonds are generally considered to involve dπ–pπ interactions between the transition metals and the terminal carbons of the ligands.[35-37]

Scheme 1.1

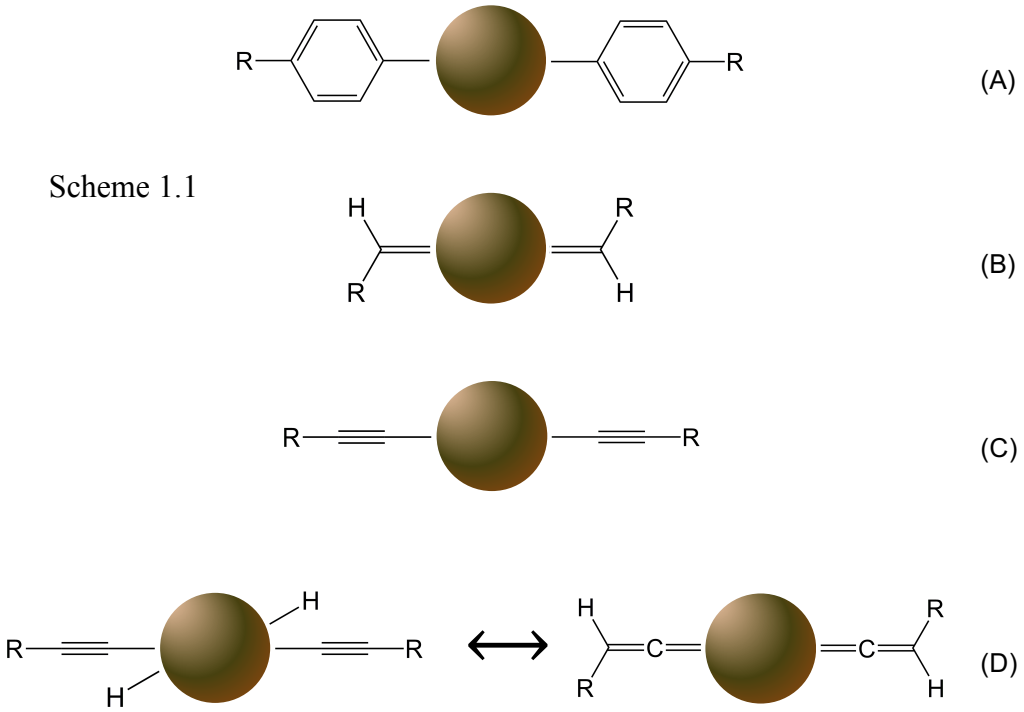

Metal nanoparticles functionalized with metal–carbon (sp^2) (M–Csp^2) single bonds can be synthesized by the coreduction of metal salts and diazonium derivatives, and the formed metal (e.g., Ru, Pt, Pd, and Ti) nanoparticles are very stable due to the strong metal–carbon covalent single bonds.[47-49, 54, 55] More importantly, due to the low contact resistance of the metal–carbon interactions, interparticle charge transfer is facilitated. For example, the solid film conductivity of palladium nanoparticles passivated with biphenyl fragments through metal–carbon(sp^2) covalent bonds (Pd–biphenyl) exhibited metallic temperature dependence in the temperature range from 80 to 320 K, and the ensemble conductivity of Pd–decylphenyl nanoparticles showed a transition from semiconductor to metal at the temperature of 180 K.[44] In

sharp contrast, the palladium nanoparticles protected by the alkanethiolate ligands only exhibited semiconductor-like conductivity.

Metal nanoparticles have also been stabilized by the formation of metal=carbene (M=C) π bonds and metal−acetylide/metal−vinylidene (M−C≡C/M=C=C) bonds through ligand self-assembly onto the "bare" metal nanoparticle colloids (stabilized with acetate groups). [2, 4, 10, 46, 49, 56-58] For instance, Ru−carbene (Ru=C) π bonds were generated with diazo derivatives as capping ligands by taking advantage of the affinity of the diazo functional groups to freshly synthesized metal nanoparticles.[45] Metal−acetylide (M−C≡C) interfacial bonds were first achieved on Ru nanoparticles protected with 1-octynide (Ru−OC), which were prepared by self-assembly of alkynyl lithium compounds onto the ruthenium nanoparticles synthesized from ruthenium salt reduced by superhydrides. [4] Later it was found that Metal−acetylide (M−C≡C) interfacial bonds can be also formed by self-assembly of intact terminal alkynes onto the surface of bare ruthenium nanoparticles.[46] Such chemistry has also been applied to other metal/alloy nanoparticles, such as Au, Pt, Pd, AuPd, and AgAu, to study the metal-carbon bond interfacial structures, new self-assembled monolayers, and their electronic, spectroscopic properties. [23, 27, 46, 49, 53, 56-64] Further ligand exchange reactions (like olefin metathesis reactions) with other ligands (such as alkynyl lithium, vinyl/acetylene derivatives) could generate more complicated functionalization of noble metal nanoparticles.[2-4, 46, 65]

Interestingly, the nanoparticle interfacial structure for nanoparticles stabilized by self-assembled intact terminal alkynes was found to involve the formation of both metal−acetylide (M−C≡C) and metal−vinylidene (M=C=C) bonds.[46] It is believed that the Ru−vinylidene (Ru=C=C) interfacial structures are generated through a tautomeric rearrangement process from Ru−acetylide (Ru−C≡C) and ruthenium hydride, and a dynamic equilibrium exists between these two interfacial structures at the metal−ligand interface. In fact, the formation of the Ru−vinylidene (Ru=C=C) interfacial bonds was confirmed by the specific reactivity of the nanoparticles with imine derivatives generating a heterocyclic complex at the metal−ligand interface, as demonstrated in ^{1}H NMR, photoluminescence, and electrochemistry studies (where ferrocenyl imine was applied as the labeling probe). Moreover, vinyl derivatives can also be involved by olefin metathesis reactions with the resulting nanoparticles, as manifested by the functionalization of the nanoparticles with 1-vinylpyrene. In comparison, the ruthenium nanoparticles capped with 1-dodecynide exhibited no such chemical reactivity with either imine or vinyl derivatives, meaning the sole formation of the Ru−acetylide (Ru−C≡C) interfacial bond at the metal−ligand interface of the (deprotonated) nanoparticles.

1.3 Intraparticle charge transfer

Thanks to the formation of the metal−carbon interfacial conjugated bonds, the prepared nanoparticles are found to exhibit effective intraparticle charge delocalization

between the particle-bound functional groups, which endow the nanoparticles with unprecedented optical, electronic, and electrochemical properties.[2, 4, 10, 48]

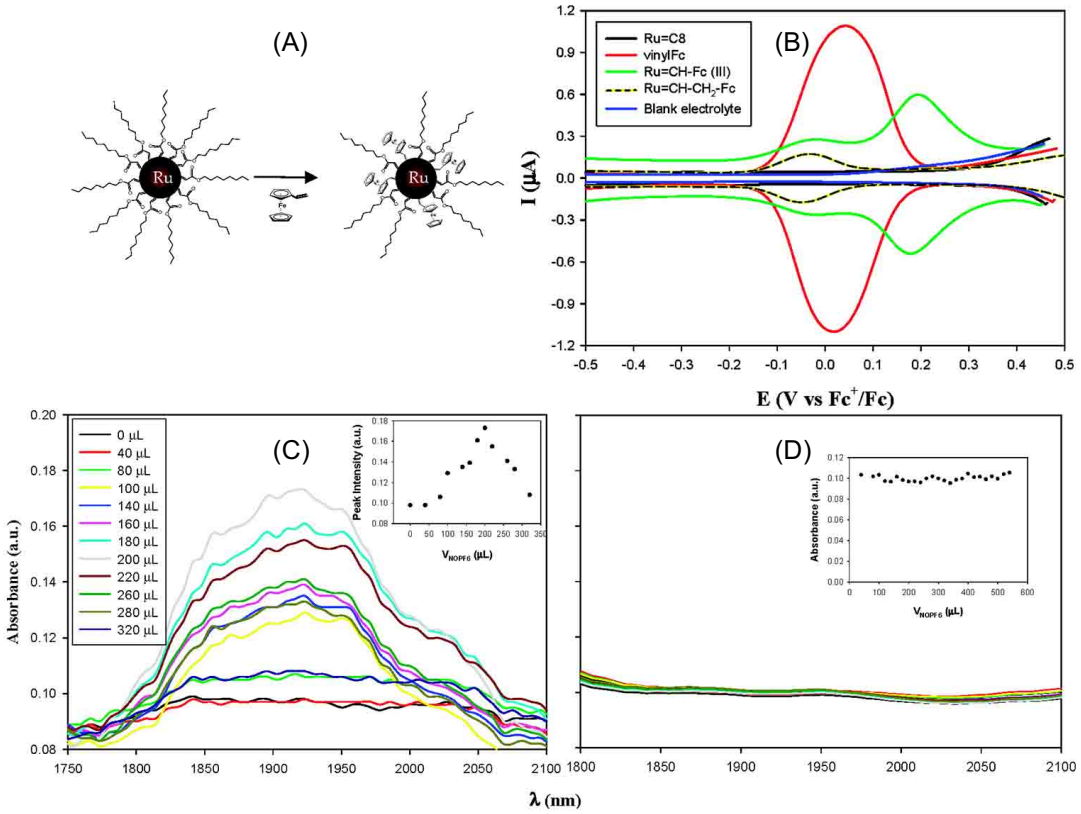

Figure 1.1. (A) Scheme of Ru=CH-Fc nanoparticles. (B) SWVs of vinylferrocene monomers, Ru=C8, Ru=CH-Fc, and Ru=CH-CH_2-Fc nanoparticles. NIR spectra of (C) Ru=CH-Fc and (D) Ru=CH-CH_2-Fc nanoparticles with addition of varied amounts of 1mM $NOPF_6$. Adapted with permission from reference.[2] Copyright © 2008 American Chemical Society.

Intraparticle charge transfer has been manifested with both photoluminescence emissions and intervalence charge transfer (IVCT) between metal centers linked to the nanoparticle metal cores. The intraparticle charge delocalization was first demonstrated within the electrochemistry measurements showing intervalence charge transfer (IVCT)

of ruthenium nanoparticles functionalized with ferrocenyl moieties through metal−carbene (M=C) π interfacial bonds (Ru=CH−Fc).[2] IVCT refers to an electron transfer process within two or more chemically identical redox-active metal centers bridged with conjugated chemical linkers, which is generally observed for organometallic complexes such as ferrocene oligomers and Creutz-Taube ion.[66, 67] Depending on the degree of charge delocalization, mixed valence compounds are categorized into three classes as suggested by Robin and Day: Class I compounds with no interactions between redox metal centers, Class II compounds exhibiting intermediate interactions between redox sites, and Class III with extensive charge delocalization between redox centers.[68] In the study, IVCT was achieved with ferrocenyl moieties attached on the ruthenium nanoparticles by conjugated interfacial bonds (M=C). The electrochemistry measurements (Figure 1.1B) showed that the Ru=CH−Fc nanoparticles exhibited two pairs of redox peaks with formal potentials ($E^{o\prime}$) at −0.019 and +0.185 V (vs Fc^{+}/Fc), resulting a potential spacing ($\Delta E^{o\prime}$) of 0.204 V, corresponding to a Class II complex. In sharp contrast, only one pair of redox peaks was observed for the Ru=CH−CH_2−Fc nanoparticles (ruthenium nanoparticles functionalized with allylferrocene). This strongly suggests the effective IVCT occurs between particle-bound functional ferrocene groups due the conjugated Ru=C interfacial interactions, while the insert of the saturated Csp^3 spacer effectively turned off the IVCT, which further demonstrates such IVCT within the nanoparticle system occurs by a through-bond mechanism. Near-infrared (NIR) spectroscopic measurements (Figure 1.1C, D) displayed consistent results with those obtained above.

With the addition of increasing amount of hexafluorophosphate ($NOPF_6$), the Ru=CH−Fc nanoparticles showed apparent absorption peak at around 1930 nm and the peak intensity exhibited volcano-shaped dependence on the amount of $NOPF_6$ added. Such spectroscopic results normally signify IVCT behavior between the ferrocene groups at mixed valence. In contrast, such absorption peak was not observed for the Ru=CH−CH_2−Fc nanoparticles.

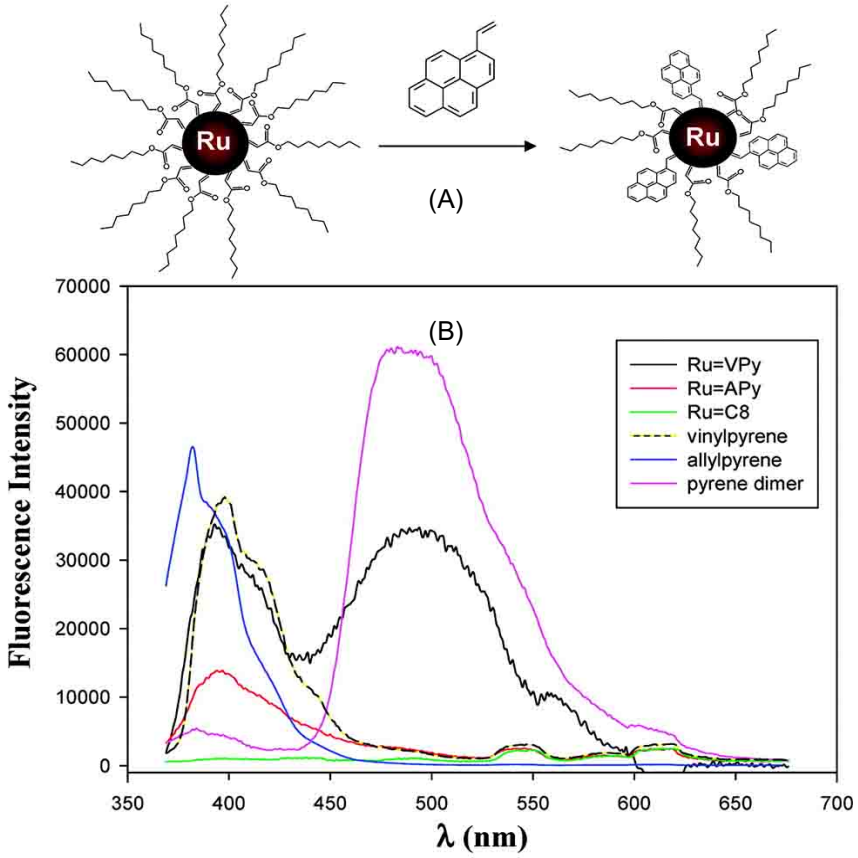

Figure 1.2. (A) Scheme of Ru=Vpy nanoparticles. (B) Fluorescence spectra of the Ru=C8, Ru=VPy, and Ru=APy nanoparticles, as well as 1-vinylpyrene, 1- allylpyrene, and (E)-1,2-di(pyren-1-yl)ethene (pyrene dimer). Adapted with permission from reference.[10] Copyright © 2009 American Chemical Society.

Such intraparticle charge delocalization has also been manifested with nanoparticle photoluminescence properties.[10, 48] For example, the Ru=VPy and Ru=APy nanoparticles were prepared by olefin metathesis reactions between Ru=C8 nanoparticles and 1-vinylpyrene and 1-allylpyrene, respectively. While the Ru=C8 nanoparticles showed no apparent fluorescence, the Ru=APy nanoparticles exhibited single emission peak at 392 nm (Figure 1.2B), corresponding to the monomeric pyrene photoluminescence emission. In sharp contrast, for the Ru=APy nanoparticles (Figure 1.2B), two major emission peaks were observed at 392 and 490 nm, which is analogous to that of conjugated pyrene dimers of (E)-1,2-di(pyren-1-yl)ethene. This suggests that extensive intraparticle charge delocalization occurs between particle-bound pyrene derivatives due to the conductive metal cores and the conjugated Ru=C π bonds, while the introduction of a saturated sp^3 hybridized carbon effectively switches it off. Similar behaviors were also obtained with Ru nanoparticles functionalized with other fluorophores like anthracene.[48]

New optical and electrochemical properties were also obtained with metal nanoparticles functionalized with acetylide fragments by the formation of M−C≡C bonds, demonstrating the intraparticle charge delocalization.[4] The FTIR measurements for the Ru−OC nanoparticles(Ru nanoparticles protected with 1-octynide (Ru−OC)[4]) illustrated that the C≡C bond vibration band red-shifted to 1936 cm^{-1} compared with 2119 cm^{-1} for 1-octyne monomers (Figure 1.3 B), which can be accounted for by the reduced bonding order due to the intraparticle charge delocalization. Moreover, the Ru−OC nanoparticles exhibited apparent

photoluminescence with well-defined excitation and emission maxima at 347 nm and 428 nm, respectively (Figure 1.3C), analogous to those for diacetylene derivatives (–C≡C–C≡C–), which again suggests the intraparticle charge delocalization because of conductive metal cores and the conjugated Ru–acetylide (Ru–C≡C) interfacial bonds. In addition, with the ruthenium nanoparticles functionalized by ferroceneyl moieties by via the formation of ruthenium–acetylide (Ru–C≡C) interfacial bonds,[4] the intraparticle charge delocalization was further confirmed in electrochemistry measurements by showing similar observations obtained for the ruthenium nanoparticles functionalized with ferrocenyl moieties through metal–carbene (M=C)

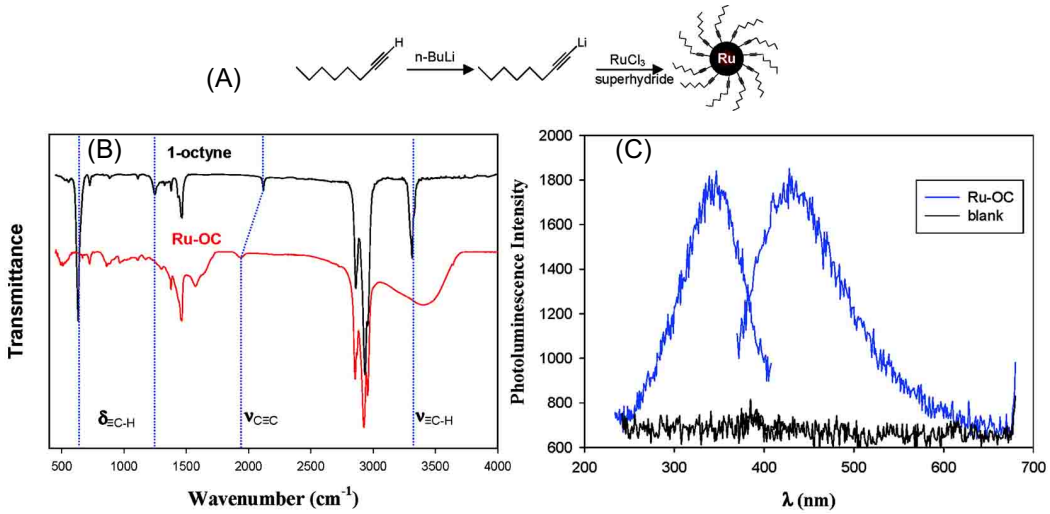

Figure 1.3. (A) Scheme of Ru-OC nanoparticles. (B) FTIR spectra of 1-octyne and Ru-OC nanoparticles. (C) Photoluminescence spectra of Ru-OC nanoparticles. Adapted with permission from reference.[4] Copyright © 2010 American Chemical Society.

π interfacial bonds (Ru=CH–Fc).[2] Similar optical performance was also observed as intact terminal alkyne derivatives are self-assembled onto the surfaces of noble nanoparticles.[46, 49, 53, 58]

1.4 Manipulation of intraparticle charge delocalization

As mentioned above, intraparticle charge delocalization takes place among the metal nanoparticle-bound functional moieties bridged with conjugated metal-carbon interfacial bonding and the conductive metal cores, leading to the emergence of the unique optical and electronic properties as manifested with spectroscopy and electrochemistry studies. Consequently, two major aspects should deserve significant attention. First, considering that the functional moieties binding on the nanoparticles behave collectively, it is possible that electron/energy transfer within part of the surface sites is propagated and/or amplified throughout the entire nanoparticles, resulting in much enhanced sensitivity of the nanoparticle to the local chemical environment. Second, the extent of the intraparticle charge delocalization among particle-bound functional moieties may also be impacted by the electronic property of the metal cores. Thus, intraparticle charge delocalization manipulation could be realized through specific designs that alter the electron/energy states with either the metal cores or the attached functional moieties on the nanoparticle surface.

Such manipulation is first demonstrated by showing the nanoparticle metal core charge states can be applied to effectively control the intraparticle conjugation and hence the intraparticle charge delocalization.[7] The ruthenium nanoparticles capped with 1-octynyl fragments (Ru–OC) were prepared and used as an example. As the nanoparticles behave as a molecular capacitor, the charge states of Ru nanoparticles cores can be readily manipulated with chemical reduction (by using $NaBH_4$) or oxidation (by using $Ce(SO_4)_2$) to generate $Ru–OC_{red}$ and $Ru–OC_{ox}$ samples. The

nanoparticle metal cores state changes were estimated in electrochemical measurements showing that each reduced nanoparticle ($Ru–OC_{Red}$) gains 0.67 electrons in average and oxidized nanoparticles ($Ru–OC_{Ox}$) exhibited an average loss of 0.63 electrons per nanoparticle. The following spectroscopic measurements demonstrated the drastic impacts of the metal core charge state on the intraparticle charge delocalization. The FTIR spectra (in Figure 1.4A) showed that the C≡C stretching vibration band appeared at 1965 cm^{-1} for the as-prepared Ru–OC nanoparticles, red-shifted compared with that at 2116 cm^{-1} for the 1-ocytyne monomers, which may be due to the intraparticle charge delocalization by the bonding coordination of the 1-octynyl groups to the Ru nanoparticle metal cores through the acetylene moieties (Ru–C≡C). Note that we have shown that particle-bound acetylene moieties behaved analogously to the acetylene dimer derivatives, –C≡C–C≡C–. In contrast, the C≡C stretching vibration band further red-shifted to 1953 cm^{-1} after reduction, while blue-shifted to 1977 cm^{-1} with oxidation. Such observation means the charging of extra electrons into the metal cores (by chemical reduction) further enhanced the charge delocalization, leading to the decreased bonding order of the C≡C moieties and more red-shifted C≡C vibration band, while the chemical oxidation caused the electron depletion of the metal nanoparticle cores, which reduced the intraparticle extended conjugation, resulting in the increased C≡C bonding order and hence less red-shifted vibration band energy (more independent particle-bound functional moieties). The nanoparticle charge state induced C≡C bonding order variation was also demonstrated with the XPS measurements. As shown in Figure 1.4B, the binding energy of the sp

carbon 1s electrons were obtained at 284.49 eV, 284. 36 eV, and 284.75 eV for the as-prepared Ru–OC, Ru–OC_{Red}, and Ru–OC_{Ox} nanoparticles, respectively, which is in agreement with the nanoparticle charge states. Consistent observation was also found in photoluminescence measurements. As shown in Figure 1.4C, although all three particle exhibited well-defined excitation/emission peaks at the same positions around 350/430 nm, the intensities were found enhanced (reduced) along with the reduction (oxidation) of the nanoparticle despite of the similar optical densities, meaning the enhancement (diminishment) of the intraparticle charge delocalization due to the chemical reduction (oxidation) of the nanoparticles.

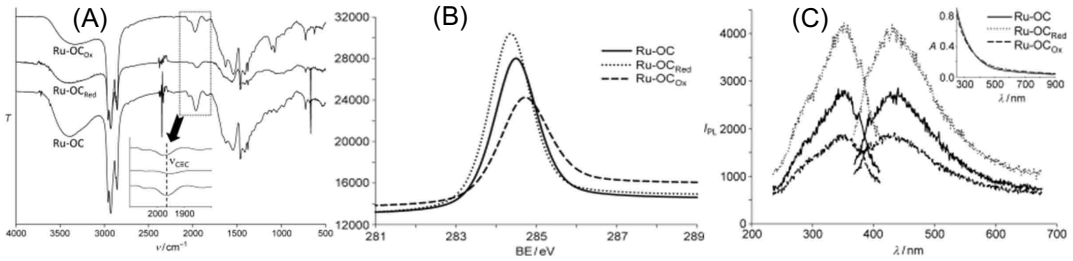

Figure 1.4. (A) FTIR spectra, (B) XPS spectra of sp-hybridized carbon atoms (C 1s electrons), and (C) excitation and emission spectra of Ru-OC nanoparticles before and after reduction and oxidation. Adapted with permission from reference.[7] Copyright © 2010 WILEY-VCH Verlag GmbH & Co. KGaA, Weinheim.

Intraparticle charge delocalization may also be manipulated by the local electron/energy transfer at part of nanoparticle surface. For instance, ruthenium nanoparticles were co-functionalized with vinylpyrene and a vinylbenzohistidine derivative through the Ru–carbene (Ru=C) π bond.[9] The intraparticle charge delocalization between particle-bound pyrene moieties may be deliberately

manipulated by the formation of the complex between the histidine group and selective metal ions through the π-type interactions, due to that the complexation polarizing the nanoparticle core electrons via the π molecular backbone within the histidine ligand bridging the imidazole ring and the nanoparticle core. In fact, this was manifested with clear photoluminescence characteristics variations. As illustrated in Figure 1.5, in the present of Hg^{2+}, Co^{2+}, and Pb^{2+} ((H)−(J)) the nanoparticles showed decreasing emission peak intensity at 490 nm and concurrent increasing emission peak intensity at 390 nm, while almost no apparent photoluminescence characteristics change was observed as the addition of Li^{+}, K^{+}, Rb^{+}, Mg^{2+}, Ca^{2+}, and Zn^{2+} ions ((B)-(G)). This is most likely accounted for by strong binding affinity of histidine to Hg^{2+}, Co^{2+}, and Pb^{2+}, and the incorporation of positive charged ionic species induced the polarization of the particle core electrons, resulting in the diminishment of the intraparticle charge delocalization between the particle-bound pyrene moieties. This means pyrene moieties attached on the nanoparticle metal core surface with the Ru=C bonds behaved more independently. As a matter of fact, similar behaviors were also observed with the Ru nanoparticles functionalized with vinylpyrene and vinylbenzo (crown ether), where apparently reduced photoluminescence intensity at 490 nm was obtained along with the crown ether moieties binding to selective alkaline metal ions.[51]

1.5 Potential applications based on intraparticle charge delocalization

The successful manipulation of the intraparticle charge delocalization confirms that the electron/energy transfer at a local site of the nanoparticles can be propagated and amplified to the whole nanoparticles, which were evidenced with apparent

discrepancy in spectroscopic and/or electrochemical properties of the resulted nanoparticles. This mechanism may be further explored as a unique platform for varied applications.

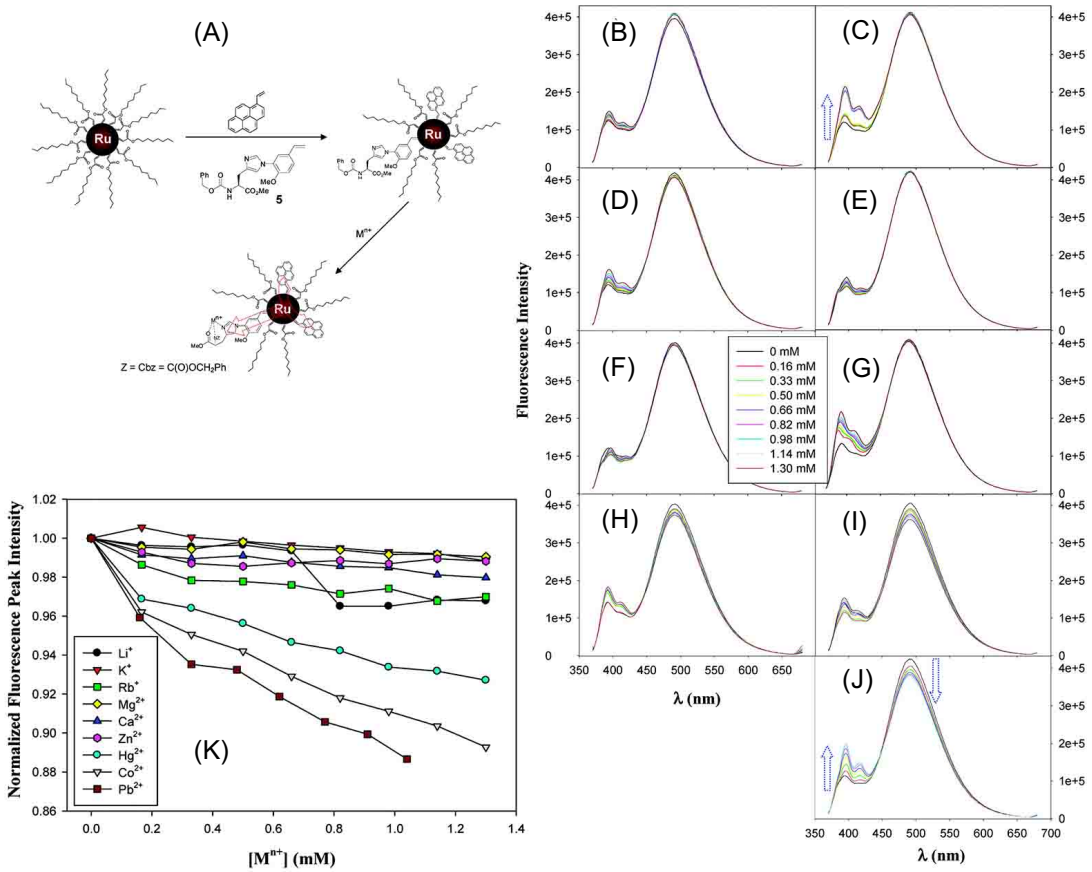

Figure 1.5. (A) Scheme of functionalization of carbene-stablized ruthenium (Ru=C8) nanoparticles with vinyl-terminated functional ligands. (B-J) Emission spectra of Ru=VPyHis nanoparticles with the addition of (B) Li^+, (C) K^+, (D) Rb^+, (E) Mg^{2+}, (F) Ca^{2+}, (G) Zn^{2+}, (H) Hg^{2+}, (I) Co^{2+}, (J) Pb^{2+}. (K) Variation of the Ru=VPyHis nanoparticle fluorescence intensity at 490 nm with the addition of varied metal ions. Adapted with permission from reference.[9] Copyright © 2012 American Chemical Society.

Manipulation of the intraparticle charge delocalization within the Ru=VPy nanoparticle were manifested with the photoluminescence variance, which could be taken as indicator for the chemical environment changes. For example, Ru=VPy

nanoparticles were explored as the chemosensor for detecting nitroaromatic derivatives (including 2,4,6- trinitrotoluene (TNT), 2,4-dinitrotoluene (2,4-DNT), 2,6-dinitro-toluene (2,6-DNT), nitrobenzene (NB), and 1-chloro-nitrobenzene (CNB)), where the Ru=VPy nanoparticles behaved analogously to pyrene conjugated polymers.[6] As shown in Figure 1.6A, TNT caused the most apparent intensity diminishment for the emission peak at 390 nm in comparison with other nitroaromatic compounds. The quenching constant obtained for TNT from the regression of the Stern−Volmer plots (Figure 1.6B) was found significantly larger than those for other compounds. More importantly, the constants obtained above were also much larger than those for previous reported luminescence chemosensors based on quantum dots or conjugated polymers. In contrast, although apparent photoluminescence intensity diminishment and similar behaviors were also observed for the Ru=APy nanoparticles, the decay was not as significant as that for the Ru=VPy nanoparticles (Figure 1.6C). The corresponding quenching constants from Stern−Volmer plots were also found much smaller as compared with those for the Ru=VPy nanoparticles. Such difference observed between Ru=VPy and Ru=APy nanoparticles were attributed to the different chemical linkers connecting the pyrene moieties with the Ru cores. The intraparticle charge delocalization resulting from the conjugated Ru=C interfacial bonding improved the electron/energy transfer from the pyrene moieties to the quencher molecules, similar to the amplification effects observed for the pyrene-based conjugated polymers. However, the extended intraparticle conjugation was effectively turned off for the Ru=APy nanoparticles with the sp^3 carbon inserted into the the interfacial linker, leading to the

decrease of the quenching efficiency. Nevertheless, both nanoparticles exhibited much higher sensitivity to nitroaromatic derivatives than pyrene monomers, which can be ascribed to the much enchanced collision frequency between the pyrene moieties and the quencher molecules because of the close proximity particle-bound pyrene groups.

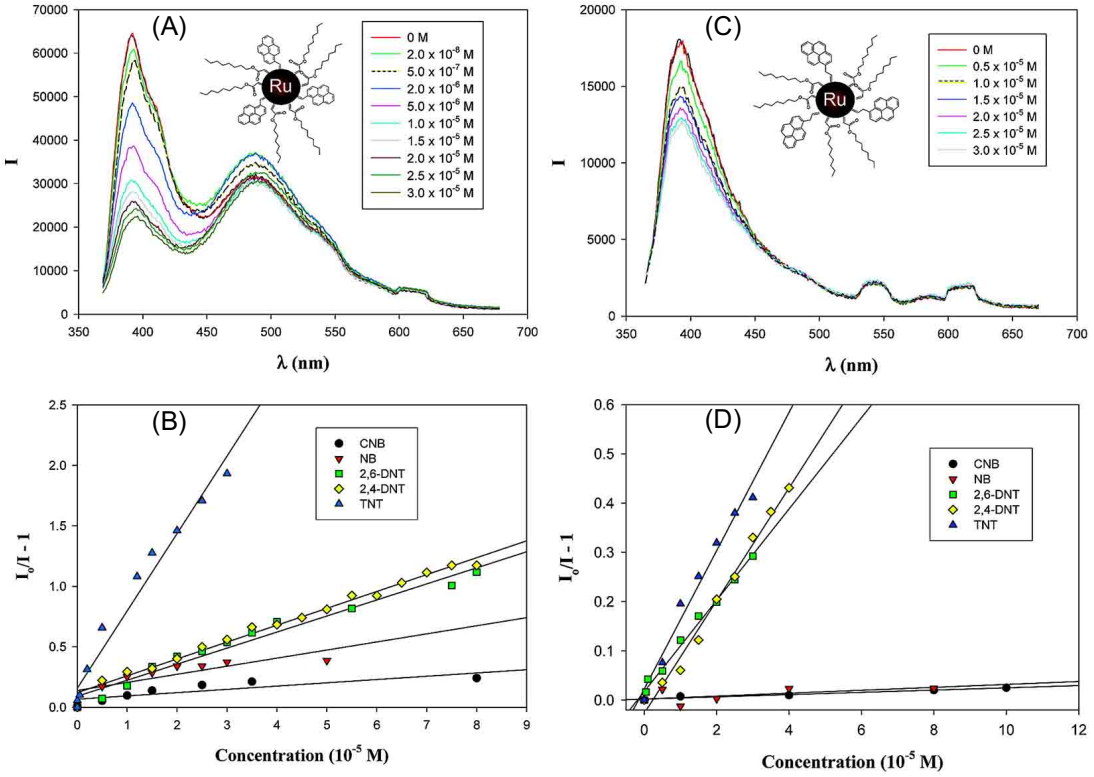

Figure 1.6. Fluorescence emission spectra of (A) Ru=VPy and (C) Ru=APy nanoparticles with the addition of varied amounts of TNT. Stern−Volmer plots of the Ru=VPy (B) and Ru=APy (D) nanoparticles in the presence of different nitroaromatic analytes. Adapted with permission from reference.[6] Copyright © 2010 American Chemical Society.

Multi-functionalized nanoparticles can also be exploited to fabricate nanoparticle-mediated molecular dyads.[3] Conventional molecular dyads represent a class of functional molecular complexes involving electrodonating/electrowithdrawing

groups associated with a chemical linker. With photoirradiation, the effective intramolecular electron/energy transfer may lead to unique optical and electronic properties. This may be further applied in multiple areas like molecular electronics, organic photovoltaics, and electroluminescence.[69, 70] It has been widely shown that the nature of the chemical linkers highly impacts the efficiency of the intramolecular electron/energy transfer and thus the optical/electronic properties of the molecular dyads. Given that the nanosized metal cores have been demonstrated to be able to behave as chemical linkers equal to conventional chemical bridges by the effective intraparticle charge delocalization, metal nanoparticles could be exploited for functional dyads (polyads), where nanoparticles cores behave as a unique structural scaffold and the the functional moieties bind onto the surface through metal–carbon covalent bonds. In this manner, the structure is significantly easy to build, and diverse and multiple functional moieties can be incorporated onto the particle surface, which readily forms a wide range of dyads (polyads) structures. More importantly, the electronic interactions between particle-bound functional moieties may be further manipulated by different interfacial bonding interactions and the metal cores electronic states. This concept was first demonstrated with specially deisgned and synthesized ruthenium nanoparticle.[3] In this study, Ru(EDPA), Ru(VAN), and Ru(EDPA/VAN) nanoparticles were prepared by functionalization of Ru "bare" colloids with 4-ethynyl-N,N-diphenylaniline, vinylanthracene, as well as 4-ethynyl-N,N-diphenylaniline and vinylanthracene, respectively, as shown in scheme in Figure 1.7A. Consequently,

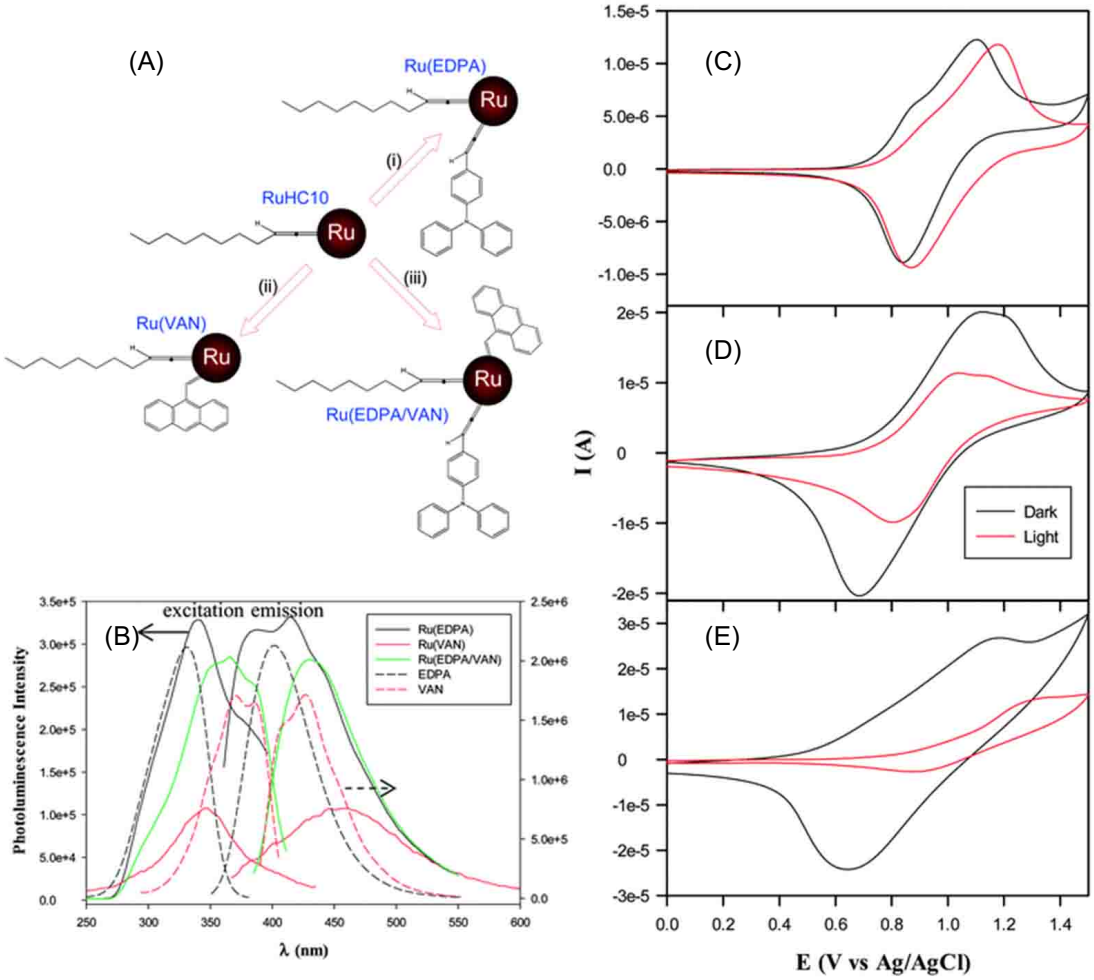

Figure 1.7. (A) Schemes of ruthenium nanoparticles functionalized with (i) EDPA, (ii) VAN or (iii) both. (B) Excitation and emission spectra of Ru(EDPA), Ru(VAN), and Ru(EDPA/VAN) nanoparticles, as well as monomeric EDPA and VAN. CVs acquired in the dark and under photoirradiation of (C) monomeric EDPA, (D) Ru(EDPA), and (E) Ru(EDPA/VAN) nanoparticles. Adapted with permission from reference.[3] Copyright © 2013 The Royal Society of Chemistry.

effective intraparticle charge transfer was anticipated upon photoirradiation from the VAN to the EDPA in Ru(EDPA/VAN) nanoparticles, revealed in photoluminescence measurements. As shown in Figure 1.7B, Ru(EDPA/VAN) displayed excitation peak at 365nm with lower energy than those for both Ru(EDPA) and Ru(VAN) and emission

peak at 431 nm in the intermediate range between those for Ru(EDPA) and Ru(VAN). Such observation means the emergence of new energy structures with efficient mixing electronic energy levels of particle-bound triphenylamine and anthracene moieties, resulting from the conjugated interfacial bonding interactions. Such photo-induced intraparticle charge transfer in Ru(EDPA/VAN) nanoparticles was further confirmed with electrochemical measurements. As depicted in Figure 1.7E, Ru(EDPA/VAN) displayed one pair of voltammetric peaks at +0.91 V in dark close to that of Ru(EDPA) nanoparticles, while the peaks almost completely disappeared under UV irradiation. This observation may be ascribed to the photoexcited electrons transfer from triphenylamine moieties to metal cores and further to the electron-accepting anthracene group, that is the UV irradiation induced the triphenylamine valence electrons depletion, and consequently the completely diminished corresponding voltammetric profiles. Such observation in electrochemical measurements were actually in agreement with that from photoluminescence, which may suggest that the nanoparticle metal cores served as conductive media facilitating the charge delocalization between particle-bound triphenylamine and anthracene moieties behaving analogously to molecular dyads with the conjugated chemical spacers.

1.6 Oxygen reduction reaction electrocatalysts based on noble metals

Fuel cells have been attracting overwhelming research interest from all over the world as portable and renewable energy sources.[71-74] However, the widely commercial applications of this technology is currently significantly limited by the high costs. This is mainly due to the relatively low efficiency of the cathode catalysts and a

large amount of Pt is required to promote the sluggish kinetics of oxygen reduction reaction (ORR) at the fuel cell cathode,[75-77] $O_2 + 4H^+ + 4e \rightarrow 2H_2O$. Thus ORR has long been a central research topic among the studies of electrode reactions.

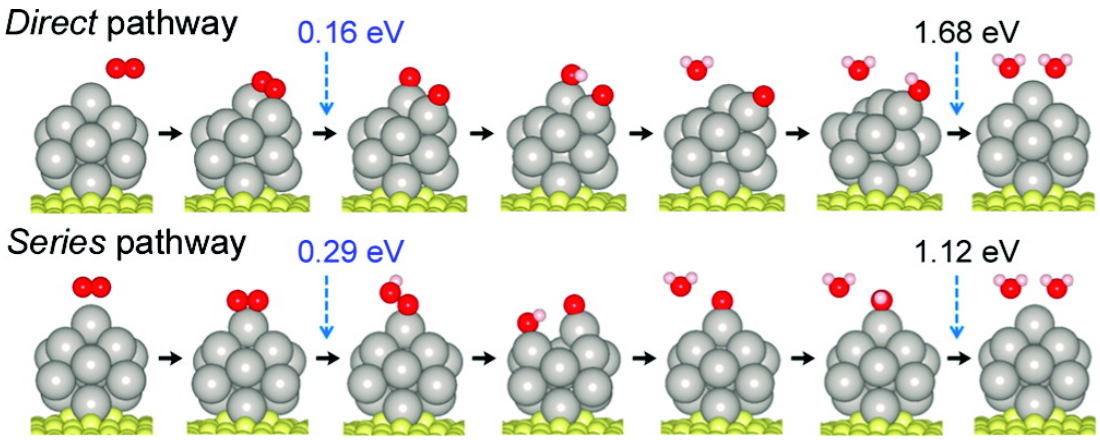

Figure 1.8. Direct and series pathways for oxygen reduction. Adapted with permission from reference.[8] Copyright © 2012 American Chemical Society.

So far, there are two leading models proposed for ORR, the direct and series pathways (Figure 1.8).[8] The difference between the two models lies in whether the hydrogen peroxide molecules are generated during the process or the sequence between the oxygen–oxygen bond breaking and the protonation of the adsorbed O_2 molecules. The former model states the bond breaking occurs before the protonation, meaning no hydrogen peroxide molecules are formed, while the latter one involves the bond breaking after the formation of hydrogen peroxide from protonation. Although the differences affect the investigation of electrocatalysis in a large degree, two significant similarities between the two models deserve further examination. First, it is always the oxygen atom that binds to the surface of the catalysts for the adsorbed oxygen or any form of the oxygen-contained intermediate (OI), regardless of the pathway. Second, it

is always the adsorption of the free oxygen molecule along with the first electron transfer involved for the initial step, while the final step required the removal of the formed water after the last electron transfer. The consequence of the first fact is that there is a linear relationship between the binding affinities of the catalysts surface to each OI during the process, meaning a strong affinity between the catalyst surface and one OI leads to the surface strongly binds to the others. While the second fact suggests that it is required of both facial oxygen adsorption and water desorption to complete an efficient reduction reaction. As a result, a moderate binding affinity of the catalysts to oxygen molecules and OIs is vital for the best ORR catalysts.[1, 78] For instance, silver and gold bind to oxygen molecules and OIs too weakly to initiate the very first adsorption of oxygen molecules, leading to a poor catalytic activity, and metals in the platinum group (Ru, Rh, Pd, Os, Ir, Pt) generally bind to oxygen and the oxygenated intermediates (OI) too strongly which is beneficial for initial oxygen adsorption but prevents facile removal of water,[1, 78] while platinum exhibits the best performance due to the moderate oxygen affinity in comparison with other metals. Nevertheless, both theoretical and experimental studies have shown that it is still about 0.1 to 0.2 eV higher of the binding energy between Pt and OIs than the optimum.[79-81]

This varying oxygen affinity along with different metals has been further predicted in different studies to relate to the d band center relative to the Fermi level.[1, 75, 78, 82-86] In fact, a volcano-shaped curve can be obtained when plotting the relative d band center level (against Fermi level) vs activity, as shown in Figure 1.9.[1] The metals with a high relative d band center against Fermi level exhibit strong

interactions with oxygen. In contrast, metals with weak oxygen affinity tend to have a low d band center. Obviously, Pt in the plot stands out as the most active ORR catalyst with much moderate oxygen affinity, while there is still room available for further improvement.

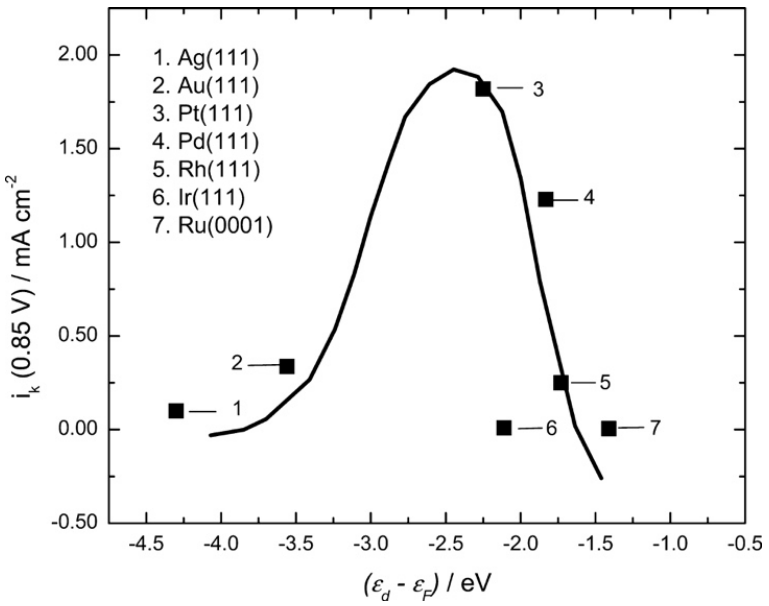

Figure 1.9. ORR specific activity of different metal (111) facets as a function of difference between d band center and Fermi level. Adapted with permission from reference[1]. Copyright © 2007 American Chemical Society.

In order to reach the theoretical volcano peak, numerous strategies have been designed and developed. These include catalysts compositions control to form core/shell or homogeneous alloy structures,[75, 78, 79, 87-90] size manipulation,[91-95] formation of catalysts structures with specific shape or highly active facet orientation,[96-99] functionalization by organic molecules,[24, 25, 100-102] as well as manipulation of interactions between catalysts and substrates.[103-113]

1.7 References

1. Lima, F.H.B., et al., *Catalytic activity-d-band center correlation for the O2 reduction reaction on platinum in alkaline solutions.* Journal of Physical Chemistry C, 2007. **111**(1): p. 404-410.
2. Chen, W., et al., *Nanoparticle-mediated intervalence transfer.* Journal of the American Chemical Society, 2008. **130**(36): p. 12156-12162.
3. Phebus, B.D., et al., *Intraparticle donor-acceptor dyads prepared using conjugated metal-ligand linkages.* Physical Chemistry Chemical Physics, 2013. **15**(40): p. 17647-17653.
4. Chen, W., et al., *Alkyne-Protected Ruthenium Nanoparticles.* J. Phys. Chem. C, 2010. **114**: p. 18146–18152.
5. Roduner, E., *Size matters: why nanomaterials are different.* Chemical Society Reviews, 2006. **35**(7): p. 583-592.
6. Chen, W., et al., *Pyrene-Functionalized Ruthenium Nanoparticles as Effective Chemosensors for Nitroaromatic Derivatives.* Analytical Chemistry, 2010. **82**(2): p. 461-465.
7. Kang, X.W., et al., *Alkyne-Stabilized Ruthenium Nanoparticles: Manipulation of Intraparticle Charge Delocalization by Nanoparticle Charge States.* Angewandte Chemie-International Edition, 2010. **49**(49): p. 9496-9499.
8. Lim, D.H. and J. Wilcox, *Mechanisms of the Oxygen Reduction Reaction on Defective Graphene-Supported Pt Nanoparticles from First-Principles.* Journal of Physical Chemistry C, 2012. **116**(5): p. 3653-3660.

9. Kang, X.W., et al., *Manipulation of Intraparticle Charge Delocalization by Selective Complexation of Transition-Metal Ions with Histidine Moieties.* Analytical Chemistry, 2012. **84**(4): p. 2025-2030.

10. Chen, W., et al., *Pyrene-Functionalized Ruthenium Nanoparticles: Novel Fluorescence Characteristics from Intraparticle Extended Conjugation.* Journal of Physical Chemistry C, 2009. **113**(39): p. 16988-16995.

11. Moreno-Manas, M. and R. Pleixats, *Formation of carbon-carbon bonds under catalysis by transition-metal nanoparticles.* Accounts of Chemical Research, 2003. **36**(8): p. 638-643.

12. Dutta, D.K., B.J. Borah, and P.P. Sarmah, *Recent Advances in Metal Nanoparticles Stabilization into Nanopores of Montmorillonite and Their Catalytic Applications for Fine Chemicals Synthesis.* Catalysis Reviews-Science and Engineering, 2015. **57**(3): p. 257-305.

13. Chen, Y., et al., *Immobilizing Highly Catalytically Active Noble Metal Nanoparticles on Reduced Graphene Oxide: A Non-Noble Metal Sacrificial Approach.* Journal of the American Chemical Society, 2015. **137**(1): p. 106-109.

14. Crooks, R.M., et al., *Dendrimer-encapsulated metal nanoparticles: Synthesis, characterization, and applications to catalysis.* Accounts of Chemical Research, 2001. **34**(3): p. 181-190.

15. Sau, T.K., et al., *Properties and Applications of Colloidal Nonspherical Noble Metal Nanoparticles.* Advanced Materials, 2010. **22**(16): p. 1805-1825.

16. Jain, P.K., et al., *Review of some interesting surface plasmon resonance-enhanced properties of noble metal nanoparticles and their applications to biosystems.* Plasmonics, 2007. **2**(3): p. 107-118.

17. Doria, G., et al., *Noble Metal Nanoparticles for Biosensing Applications.* Sensors, 2012. **12**(2): p. 1657-1687.

18. Conde, J., G. Doria, and P. Baptista, *Noble Metal Nanoparticles Applications in Cancer.* Journal of Drug Delivery, 2012. **2012**: p. 12.

19. Jain, P.K., et al., *Calculated absorption and scattering properties of gold nanoparticles of different size, shape, and composition: Applications in biological imaging and biomedicine.* Journal of Physical Chemistry B, 2006. **110**(14): p. 7238-7248.

20. Murphy, C.J., et al., *Anisotropic metal nanoparticles: Synthesis, assembly, and optical applications.* Journal of Physical Chemistry B, 2005. **109**(29): p. 13857-13870.

21. Daniel, M.C. and D. Astruc, *Gold nanoparticles: Assembly, supramolecular chemistry, quantum-size-related properties, and applications toward biology, catalysis, and nanotechnology.* Chemical Reviews, 2004. **104**(1): p. 293-346.

22. Long, N.V., et al., *Synthesis and Characterization of Fe-Based Metal and Oxide Based Nanoparticles: Discoveries and Research Highlights of Potential Applications in Biology and Medicine.* Recent Patents on Nanotechnology, 2014. **8**(1): p. 52-61.

23. Hu, P.G., et al., *Electrocatalytic activity of alkyne-functionalized AgAu alloy nanoparticles for oxygen reduction in alkaline media.* Nanoscale, 2015. **7**(21): p. 9627-9636.

24. Zhou, Z.Y., et al., *Enhancement of the electrocatalytic activity of Pt nanoparticles in oxygen reduction by chlorophenyl functionalization.* Chemical Communications, 2012. **48**(28): p. 3391-3393.

25. Zhou, Z.Y., et al., *Ligand-Mediated Electrocatalytic Activity of Pt Nanoparticles for Oxygen Reduction Reactions.* Journal of Physical Chemistry C, 2012. **116**(19): p. 10592-10598.

26. Zhou, Z.Y., et al., *Butylphenyl-functionalized Pt nanoparticles as CO-resistant electrocatalysts for formic acid oxidation.* Physical Chemistry Chemical Physics, 2012. **14**(4): p. 1412-7.

27. Deming, C.P., et al., *Alkyne-Protected AuPd Alloy Nanoparticles for Electrocatalytic Reduction of Oxygen.* Chemelectrochem, 2015. **2**(11): p. 1719-1727.

28. Mayer, K.M. and J.H. Hafner, *Localized Surface Plasmon Resonance Sensors.* Chemical Reviews, 2011. **111**(6): p. 3828-3857.

29. Fong, K.E. and L.Y.L. Yung, *Localized surface plasmon resonance: a unique property of plasmonic nanoparticles for nucleic acid detection.* Nanoscale, 2013. **5**(24): p. 12043-12071.

30. Campelo, J.M., et al., *Sustainable Preparation of Supported Metal Nanoparticles and Their Applications in Catalysis.* Chemsuschem, 2009. **2**(1): p. 18-45.

31. Astruc, D., *Transition-metal Nanoparticles in Catalysis: From Historical Background to the State-of-the Art*, in *Nanoparticles and Catalysis*. 2008, Wiley-VCH Verlag GmbH & Co. KGaA. p. 1-48.

32. Neouze, M.A. and U. Schubert, *Surface modification and functionalization of metal and metal oxide nanoparticles by organic ligands.* Monatshefte Fur Chemie, 2008. **139**(3): p. 183-195.

33. Brust, M., et al., *Synthesis of Thiol-Derivatized Gold Nanoparticles in a 2-Phase Liquid-Liquid System.* Journal of the Chemical Society-Chemical Communications, 1994(7): p. 801-802.

34. Chen, S.W. and R.W. Murray, *Arenethiolate monolayer-protected gold clusters.* Langmuir, 1999. **15**(3): p. 682-689.

35. Crabtree, R.H., *Organometallic Chemistry of the Transition Metals, 6th Edition.* Organometallic Chemistry of the Transition Metals, 6th Edition, 2014: p. 1-504.

36. Siegbahn, P.E.M., *Trends of Metal-Carbon Bond Strengths in Transition-Metal Complexes.* Journal of Physical Chemistry, 1995. **99**(34): p. 12723-12729.

37. Simoes, J.A.M. and J.L. Beauchamp, *Transition-Metal Hydrogen and Metal-Carbon Bond Strengths - the Keys to Catalysis.* Chemical Reviews, 1990. **90**(4): p. 629-688.

38. Shahid, G. and N. Sheppard, *Ir-Spectra and the Structures of the Chemisorbed Species Resulting from the Adsorption of the Linear Butenes on a Pt/Sio2 Catalyst .1. Temperature-Dependence of the Spectra.* Journal of the Chemical Society-Faraday Transactions, 1994. **90**(3): p. 507-511.

39. Shahid, G. and N. Sheppard, *Ir-Spectra and the Structures of the Chemisorbed Species Resulting from the Adsorption of the Linear Butenes on a Pt/Sio2 Catalyst .2. Spectra of the Hydrogenated Surface Species as a Function of Temperature.* Journal of the Chemical Society-Faraday Transactions, 1994. **90**(3): p. 513-516.

40. Sheppard, N., *Vibrational Spectroscopic Studies of the Structure of Species Derived from the Chemisorption of Hydrocarbons on Metal Single-Crystal Surfaces.* Annual Review of Physical Chemistry, 1988. **39**: p. 589-644.

41. Trevor, D.J., et al., *Evidence of Extensive Dehydrogenation and Size Dependent Chemisorption in the Molecular-Surface Chemistry of Platinum Cluster with Hydrocarbons.* Abstracts of Papers of the American Chemical Society, 1985. **189**(Apr-): p. 184-Coll.

42. Lide, D.R., *CRC handbook of chemistry and physics: a ready-reference book of chemical and physical data*. 2004, Boca Raton, FL: CRC Press.

43. Zhou, Z.Y., et al., *Butylphenyl-functionalized palladium nanoparticles as effective catalysts for the electrooxidation of formic acid.* Chemical Communications, 2011. **47**(21): p. 6075-6077.

44. Ghosh, D. and S.W. Chen, *Palladium nanoparticles passivated by metal-carbon covalent linkages.* Journal of Materials Chemistry, 2008. **18**(7): p. 755-762.

45. Chen, W., et al., *Carbene-functionalized ruthenium nanoparticles.* Chemistry of Materials, 2006. **18**(22): p. 5253-5259.

46. Kang, X., et al., *Alkyne-functionalized ruthenium nanoparticles: ruthenium-vinylidene bonds at the metal-ligand interface.* J Am Chem Soc, 2012. **134**(3): p. 1412-1415.

47. Ghosh, D. and S.W. Chen, *Solid-state electronic conductivity of ruthenium nanoparticles passivated by metal-carbon covalent bonds.* Chemical Physics Letters, 2008. **465**(1-3): p. 115-119.

48. Chen, W., S. Pradhan, and S.W. Chen, *Photoluminescence and conductivity studies of anthracene-functionalized ruthenium nanoparticles.* Nanoscale, 2011. **3**(5): p. 2294-2300.

49. Kang, X.W. and S.W. Chen, *Electronic conductivity of alkyne-capped ruthenium nanoparticles.* Nanoscale, 2012. **4**(14): p. 4183-4189.

50. Hu, P.G., et al., *Self-Assembly and Chemical Reactivity of Alkenes on Platinum Nanoparticles.* Langmuir, 2015. **31**(1): p. 522-528.

51. Kang, X.W., et al., *Intraparticle Charge Delocalization of Carbene-Functionalized Ruthenium Nanoparticles Manipulated by Selective Ion Binding.* Langmuir, 2011. **27**(20): p. 12636-12641.

52. Hu, P.G., et al., *Platinum Nanoparticles Functionalized with Ethynylphenylboronic Acid Derivatives: Selective Manipulation of Nanoparticle Photoluminescence by Fluoride Ions.* Langmuir, 2014. **30**(18): p. 5224-5229.

53. Liu, K., Y. Song, and S.W. Chen, *Electrocatalytic activities of alkyne-functionalized copper nanoparticles in oxygen reduction in alkaline media.* Journal of Power Sources, 2014. **268**: p. 469-475.

54. Mirkhalaf, F., J. Paprotny, and D.J. Schiffrin, *Synthesis of metal nanoparticles stabilized by metal-carbon bonds.* Journal of the American Chemical Society, 2006. **128**(23): p. 7400-7401.

55. Kawai, K., et al., *Synthesis and antibacterial properties of water-dispersible silver nanoparticles stabilized by metal-carbon sigma-bonds.* Applied Surface Science, 2012. **262**: p. 76-80.

56. Maity, P., et al., *Binding Motif of Terminal Alkynes on Gold Clusters.* Journal of the American Chemical Society, 2013. **135**(25): p. 9450-9457.

57. Zhang, S., K.L. Chandra, and C.B. Gorman, *Self-assembled monolayers of terminal alkynes on gold.* Journal of the American Chemical Society, 2007. **129**(16): p. 4876-+.

58. He, G.Q., et al., *Alkyne-functionalized palladium nanoparticles: Synthesis, characterization, and electrocatalytic activity in ethylene glycol oxidation.* Electrochimica Acta, 2013. **94**: p. 98-103.

59. Patterson, M.L. and M.J. Weaver, *Surface-Enhanced Raman-Spectroscopy as a Probe of Adsorbate Surface Bonding - Simple Alkenes and Alkynes Adsorbed at Gold Electrodes.* Journal of Physical Chemistry, 1985. **89**(23): p. 5046-5051.

60. Ford, M.J., R.C. Hoft, and A. McDonagh, *Theoretical study of ethynylbenzene adsorption on Au(111) and implications for a new class of self-assembled monolayer.* Journal of Physical Chemistry B, 2005. **109**(43): p. 20387-20392.

61. Li, Q., et al., *Electronic Control over Attachment and Self-Assembly of Alkyne Groups on Gold.* Acs Nano, 2012. **6**(10): p. 9267-9275.

62. Feilchenfeld, H. and M.J. Weaver, *Binding of Alkynes to Silver, Gold, and Underpotential-Deposited Silver Electrodes as Deduced by Surface-Enhanced Raman-Spectroscopy.* Journal of Physical Chemistry, 1989. **93**(10): p. 4276-4282.

63. Boronat, M., et al., *Making C-C Bonds with Gold: Identification of Selective Gold Sites for Homo- and Cross-Coupling Reactions between Iodobenzene and Alkynes.* Journal of Physical Chemistry C, 2012. **116**(47): p. 24855-24867.

64. Joo, S.-W. and K. Kim, *Adsorption of phenylacetylene on gold nanoparticle surfaces investigated by surface-enhanced Raman scattering.* Journal of Raman Spectroscopy, 2004. **35**(7): p. 549-554.

65. Chen, W., et al., *Intervalence transfer of ferrocene moieties adsorbed on electrode surfaces by a conjugated linkage.* Chemical Physics Letters, 2009. **471**(4-6): p. 283-285.

66. Powers, M.J. and T.J. Meyer, *Intervalence Transfer in Mixed-Valence Biferrocene Ions.* Journal of the American Chemical Society, 1978. **100**(14): p. 4393-4398.

67. Creutz, C. and H. Taube, *Binuclear Complexes of Ruthenium Ammines.* Journal of the American Chemical Society, 1973. **95**(4): p. 1086-1094.

68. Robin, M.B. and P. Day, *Mixed Valence Chemistry-A Survey and Classification*, in *Advances in Inorganic Chemistry and Radiochemistry*, H.J. Emeléus and A.G. Sharpe, Editors. 1968, Academic Press. p. 247-422.

69. Raymo, F.M. and M. Tomasulo, *Electron and energy transfer modulation with photochromic switches.* Chemical Society Reviews, 2005. **34**(4): p. 327-336.

70. Lin, Y.Z., Y.F. Li, and X.W. Zhan, *Small molecule semiconductors for high-efficiency organic photovoltaics.* Chemical Society Reviews, 2012. **41**(11): p. 4245-4272.

71. Cano-Castillo, U., *Hydrogen and Fuel Cells: Potential Elements in the Energy Transition Scenario.* Revista Mexicana De Fisica, 2013. **59**(2): p. 85-92.

72. Hamrock, S.J., A.M. Herring, and T.A. Zawodzinski, *Fuel cell chemistry and operation.* Journal of Power Sources, 2007. **172**(1): p. 1-1.

73. Patel, A., et al., *Investigating the effects of proton exchange membrane fuel cell conditions on carbon supported platinum electrocatalyst composition and performance.* Journal of Vacuum Science & Technology A, 2012. **30**(4): p. 04D107.

74. Borup, R., et al., *Scientific aspects of polymer electrolyte fuel cell durability and degradation.* Chemical Reviews, 2007. **107**(10): p. 3904-3951.

75. Stephens, I.E.L., et al., *Understanding the electrocatalysis of oxygen reduction on platinum and its alloys.* Energy & Environmental Science, 2012. **5**(5): p. 6744.

76. Norskov, J.K., et al., *Origin of the Overpotential for Oxygen Reduction at a Fuel-Cell Cathode.* Journal of Physical Chemistry B, 2004. **108**: p. 17886-17892.

77. Ramaswamy, N. and S. Mukerjee, *Fundamental Mechanistic Understanding of Electrocatalysis of Oxygen Reduction on Pt and Non-Pt Surfaces: Acid versus Alkaline Media.* Advances in Physical Chemistry, 2012. **2012**: p. 1-17.

78. Kitchin, J.R., et al., *Modification of the surface electronic and chemical properties of Pt(111) by subsurface 3d transition metals.* Journal of Chemical Physics, 2004. **120**(21): p. 10240-10246.

79. Stephens, I.E.L., et al., *Tuning the Activity of Pt(111) for Oxygen Electroreduction by Subsurface Alloying.* Journal of the American Chemical Society, 2011. **133**(14): p. 5485-5491.

80. Greeley, J., et al., *Alloys of platinum and early transition metals as oxygen reduction electrocatalysts.* Nature Chemistry, 2009. **1**(7): p. 552-556.

81. Greeley, J. and J.K. Norskov, *Combinatorial Density Functional Theory-Based Screening of Surface Alloys for the Oxygen Reduction Reaction.* Journal of Physical Chemistry C, 2009. **113**(12): p. 4932-4939.

82. Hammer, B. and J.K. Norskov, *Electronic factors determining the reactivity of metal surfaces.* Surface Science, 1995. **343**(3): p. 211-220.

83. Hennig, D., M.V. GandugliaPirovano, and M. Scheffler, *Adlayer core-level shifts of admetal monolayers on transition-metal substrates and their relation to the surface chemical reactivity.* Physical Review B, 1996. **53**(15): p. 10344-10347.

84. Bzowski, A., et al., *Electronic-Structure of Au and Ag Overlayers on Ru(001) - the Behavior of the Noble-Metal D-Bands.* Physical Review B, 1995. **51**(15): p. 9979-9984.

85. Weinert, M. and R.E. Watson, *Core-Level Shifts in Bulk Alloys and Surface Adlayers.* Physical Review B, 1995. **51**(23): p. 17168-17180.

86. Toyoda, E., et al., *The d-Band Structure of Pt Nanoclusters Correlated with the Catalytic Activity for an Oxygen Reduction Reaction.* Journal of Physical Chemistry C, 2011. **115**(43): p. 21236-21240.

87. Carpenter, M.K., et al., *Solvothermal Synthesis of Platinum Alloy Nanoparticles for Oxygen Reduction Electrocatalysis.* Journal of the American Chemical Society, 2012. **134**(20): p. 8535-8542.

88. Seo, A., et al., *Performance and stability of Pt-based ternary alloy catalysts for PEMFC.* Electrochimica Acta, 2006. **52**(4): p. 1603-1611.

89. Stamenkovic, V.R., et al., *Improved oxygen reduction activity on Pt3Ni(111) via increased surface site availability.* Science, 2007. **315**(5811): p. 493-497.

90. Luo, J., et al., *Activity-composition correlation of AuPt alloy nanoparticle catalysts in electrocatalytic reduction of oxygen.* Electrochemistry Communications, 2006. **8**(4): p. 581-587.

91. Paalanen, P., B.M. Weckhuysen, and M. Sankar, *Progress in controlling the size, composition and nanostructure of supported gold-palladium nanoparticles for catalytic applications.* Catalysis Science & Technology, 2013. **3**(11): p. 2869-2880.

92. Liu, Y., et al., *Importance of Particle Size and Distribution in Achieving High-Activity, High-Stability Oxygen Reduction Catalysts.* Acs Catalysis, 2015. **5**(3): p. 1560-1567.

93. Zhou, W.J., et al., *Pd particle size effects on oxygen electrochemical reduction.* International Journal of Hydrogen Energy, 2014. **39**(12): p. 6433-6442.

94. Shao, M.H., A. Peles, and K. Shoemaker, *Electrocatalysis on Platinum Nanoparticles: Particle Size Effect on Oxygen Reduction Reaction Activity.* Nano Letters, 2011. **11**(9): p. 3714-3719.

95. Kim, J.W., et al., *Size-controlled synthesis of Pt nanoparticles and their electrochemical activities toward oxygen reduction.* International Journal of Hydrogen Energy, 2011. **36**(1): p. 706-712.

96. Wang, J.X., et al., *Oxygen Reduction on Well-Defined Core-Shell Nanocatalysts: Particle Size, Facet, and Pt Shell Thickness Effects.* Journal of the American Chemical Society, 2009. **131**(47): p. 17298-17302.

97. Lee, C.L., et al., *Silver triangular nanoplates as electrocatalyst for oxygen reduction reaction.* Electrochemistry Communications, 2010. **12**(11): p. 1609-1613.

98. Wu, J.B., et al., *Truncated Octahedral Pt3Ni Oxygen Reduction Reaction Electrocatalysts.* Journal of the American Chemical Society, 2010. **132**(14): p. 4984-+.

99. Shao, M.H., et al., *Electrocatalysis on Shape-Controlled Palladium Nanocrystals: Oxygen Reduction Reaction and Formic Acid Oxidation.* Journal of Physical Chemistry C, 2013. **117**(8): p. 4172-4180.

100. He, G.Q., et al., *Electrocatalytic Activity of Organically Functionalized Silver Nanoparticles in Oxygen Reduction.* Science of Advanced Materials, 2013. **5**(11): p. 1727-1736.

101. Liu, K., et al., *Platinum nanoparticles functionalized with acetylene derivatives: Electronic conductivity and electrocatalytic activity in oxygen reduction.* Journal of Electroanalytical Chemistry, 2013. **688**: p. 143-150.

102. Pietron, J.J., et al., *Electrochemical Observation of Ligand Effects on Oxygen Reduction at Ligand-Stabilized Pt Nanoparticle Electrocatalysts.* Electrochemical and Solid-State Letters, 2008. **11**(8): p. B161.

103. Kongkanand, A., et al., *Single-wall carbon nanotubes supported platinum nanoparticles with improved electrocatalytic activity for oxygen reduction reaction.* Langmuir, 2006. **22**(5): p. 2392-2396.

104. Li, W.Z., et al., *Preparation and characterization of multiwalled carbon nanotube-supported platinum for cathode catalysts of direct methanol fuel cells.* Journal of Physical Chemistry B, 2003. **107**(26): p. 6292-6299.

105. Joo, S.H., et al., *Preparation of high loading Pt nanoparticles on ordered mesoporous carbon with a controlled Pt size and its effects on oxygen reduction and methanol oxidation reactions.* Electrochimica Acta, 2009. **54**(24): p. 5746-5753.

106. Ding, J., et al., *Platinum and platinum-ruthenium nanoparticles supported on ordered mesoporous carbon and their electrocatalytic performance for fuel cell reactions.* Electrochimica Acta, 2005. **50**(15): p. 3131-3141.

107. Wen, Z.H., J. Liu, and J.H. Li, *Core/shell Pt/C nanoparticles embedded in mesoporous carbon as a methanol-tolerant cathode catalyst in direct methanol fuel cells.* Advanced Materials, 2008. **20**(4): p. 743-747

.

108. Hsin, Y.L., K.C. Hwang, and C.T. Yeh, *Poly(vinylpyrrolidone)-modified graphite carbon nanofibers as promising supports for PtRu catalysts in direct methanol fuel cells.* Journal of the American Chemical Society, 2007. **129**(32): p. 9999-10010.

109. Jia, J.C., et al., *SnO2-embedded worm-like carbon nanofibers supported Pt nanoparticles for oxygen reduction reaction.* Electrochimica Acta, 2014. **141**: p. 13-19.

110. He, G., et al., *Oxygen Reduction Catalyzed by Platinum Nanoparticles Supported on Graphene Quantum Dots.* Acs Catalysis, 2013. **3**(5): p. 831-838.

111. Song, Y. and S. Chen, *Graphene quantum-dot-supported platinum nanoparticles: defect-mediated electrocatalytic activity in oxygen reduction.* ACS Appl Mater Interfaces, 2014. **6**(16): p. 14050-60.

112. Liang, Y.Y., et al., *Co3O4 nanocrystals on graphene as a synergistic catalyst for oxygen reduction reaction.* Nature Materials, 2011. **10**(10): p. 780-786.

113. Wu, Z.S., et al., *3D Nitrogen-Doped Graphene Aerogel-Supported Fe3O4 Nanoparticles as Efficient Eletrocatalysts for the Oxygen Reduction Reaction.* Journal of the American Chemical Society, 2012. **134**(22): p. 9082-9085.

Chapter 2

Identification of the Formation of Metal-Vinylidene Interfacial Bonds of Alkyne-Capped Platinum Nanoparticles by Isotopic Labelling

Reproduced with permission from (Peiguang Hu, Limei Chen, Christopher P. Deming, Lewis W. Bonny, Hsiau-Wei Lee, Shaowei Chen, "Identification of the Formation of Metal-Vinylidene Interfacial Bonds of Alkyne-Capped Platinum Nanoparticles by Isotopic Labelling"), in revision.

2.1 Abstract

Stable platinum nanoparticles were prepared by the self-assembly of 1-dodecyne and dodec-1-deuteroyne onto bare platimum colloid surfaces. The nanoparticles exhibited consistent core size and optical properties. FTIR and NMR measurements confirmed the formation of Pt–vinylidene (Pt=C=CH–) interfacial linkages rather than Pt–acetylide (Pt–C≡C–) and platinum–hydride (Pt–H) bonds.

2.2 Introduction

Recently it has been observed that metal-ligand interfacial bonding interactions may be exploited as a new, effective variable in the manipulation of the chemical and physical properties of metal nanoparticles.[1-3] Of these, acetylene derivatives represent a unique capping ligand, as they may be readily self-assembled onto transition metal surfaces, forming conjugated metal-carbon bonds. This leads to apparent intraparticle charge delocalization between the particle-bound functional moieties and hence new optical and electronic properties. For instance,[4, 5] ruthenium nanoparticles have been functionalized with n-octynyl fragments (deprotonated n-octyne) through the formation of ruthenium–acetylide (Ru–C≡) bonds. The resulting nanoparticles exhibit an apparent red-shift of the C≡C vibrational energy and photoluminescence emission that is analogous to those of diacetylene derivatives (–C≡C–C≡C–); and with ethynylferrocenyl fragments incorporated into the nanoparticle capping layer, intervalence charge transfer occurs between the ferrocenyl metal centers at mixed valence, a behavior analogous to ferrocene oligomers, which suggests nanoparticle-mediated electronic communication thanks to the conjugated

metal-ligand interfacial linkages.[4, 5] More recently, it has been found that metal nanoparticles can also be stabilized by the direct self-assembly of n-alkynes onto "bare" metal colloids,[6-8] due to the formation of metal–vinylidene (M=C=CH–) interfacial bonding linkages that are in a dynamic equilibrium with metal–acetylide (M–C≡) and metal hydride (M–H) bonds by a tautomeric rearrangement process (Scheme 1). Such a hypothesis is supported by the specific reactivity of the nanoparticles with imine derivatives. Note that in alkyne-transition metal complexes, the metal–vinylidene (M=C=CH–) structure is thermodynamically favorable.[9, 10] Thus, one immediate question arises. Is metal–vinylidene (M=C=CH–) bond also the dominant interfacial bonding linkages on alkyne-capped metal nanoparticles? This remains an outstanding question and is the primary motivation of the present study.

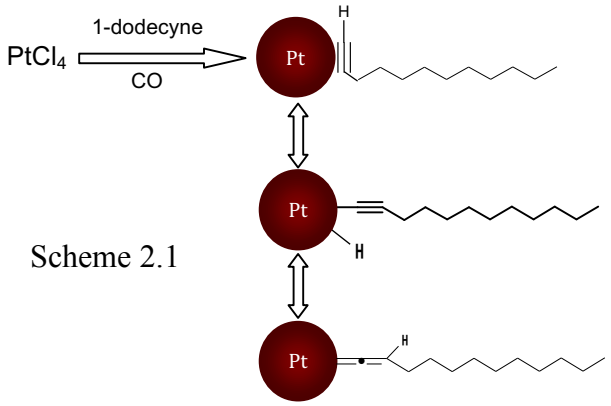

Scheme 2.1

Herein, we compare the spectroscopic characteristics of platinum nanoparticles functionalized with n-dodecyne (HC12) and dodec-1-deuteroyne (DC12). FTIR and ^{1}H and ^{2}H NMR spectroscopic measurements showed clear

signatures of platinum−vinylidene (Pt)=C=CH−) linkages whereas none for platinum-hydride and platinum-acetylide.

2.3 Experimental Section

Chemicals. 1-Dodecyne (HC12, 98%, ACROS), deuterium oxide (D_2O, 99.9%, Cambridge Isotope Laboratory Inc.), hexane-d_{14} (99 atom% D, Sigma-Aldrich), potassium carbonate (K_2CO_3, 99.3%, Fisher Chemical), magnesium sulfate ($MgSO_4$, anhydrous, ≥ 97%, Sigma Aldrich), chloroform-d, ($CDCl_3$, 99.6%, ACROS), platinum (IV) chloride ($PtCl_4$, 99%, ACROS), and carbon monoxide (CO, 99.5%) were all used as received. All solvents were obtained from typical commercial sources and used without further treatment. Water was supplied by a Barnstead Nanopure water system (18.3 MΩ·cm).

Synthesis of Dodec-1-deuteroyne (DC12). DC12 was synthesized by following a previously reported procedure.[11] Briefly, a flame dried 20 mL vial was charged with 0.5 mmol (83 mg) of HC12 and 0.75 mmol (103 mg) of K_2CO_3 in 2 mL of acetonitrile. The mixture was stirred under a N_2 atmosphere for 30 min, followed by the addition of 0.5 mL of D_2O and then heated up to 50 °C and stirred for 24 h. After the solution was cooled down to room temperature, the organic phase was collected and dried by adding excessive $MgSO_4$. The organic solution was then centrifuged to remove solid salts, and the solvent was evaporated by blowing N_2 to obtain the final product of DC12. ^{1}H NMR measurements showed that about 90% of the original 1-dodecyne was deuterated (Figure 2.5).

Synthesis of Platinum Nanoparticles. HC12-functionalized platinum nanoparticles (PtHC12) were prepared by adopting the carbon monoxide reduction method described in previous studies.[12, 13] In brief, 0.1 mmol of $PtCl_4$ was first dissolved in 1 mL of H_2O in a 20 mL glass vial. 40 μL of HC12 was added to the solution, and the mixture was bubbled with CO for 30 min under magnetic stirring. The vial was then sealed and subjected to stirring for overnight. It was found that the bottom aqueous phase became colorless while the thin organic phase turned dark brown. The organic phase was collected and rinsed with copious acetonitrile to remove excessive HC12, affording the PtHC12 nanoparticles. DC12-functionalized platinum (PtDC12) nanoparticles were prepared in a similar fashion except that D_2O and DC12 were used instead. Both nanoparticles were readily soluble in common organic solvents such as CH_2Cl_2, $CHCl_3$, THF, toluene, alkanes, etc.

Characterizations. Transmission electron microscopic (TEM) measurements were conducted with a Philips CM300/FEG transmission electron microscope operated at 300 kV. UV-vis spectra were obtained with a Perkin-Elmer Lambda 35 UV-vis spectrometer by using a quartz cuvette (1 cm × 1cm) as a sample container, and photoluminescence measurements were performed on a FluoroMax-3 fluorospectrometer with the same samples used for UV-vis absorption measurements. FTIR spectroscopic studies were carried out on a Perkin-Elmer FTIR spectrometer (Spectrum One, spectral resolution 1 cm^{-1}), where the samples were prepared by dropcasting on a ZnSe disk. ^1H NMR spectroscopic measurements were carried out with a Varian Unity Inova 500 MHz NMR spectrometer with the samples dissolved in

$CDCl_3$, while ^2H NMR spectroscopic studies were performed with a Bruker Avance III HD 800 MHz NMR spectrometer with samples dissolved in *n*-hexane-d_{14}.

2.4 Results and Discussion

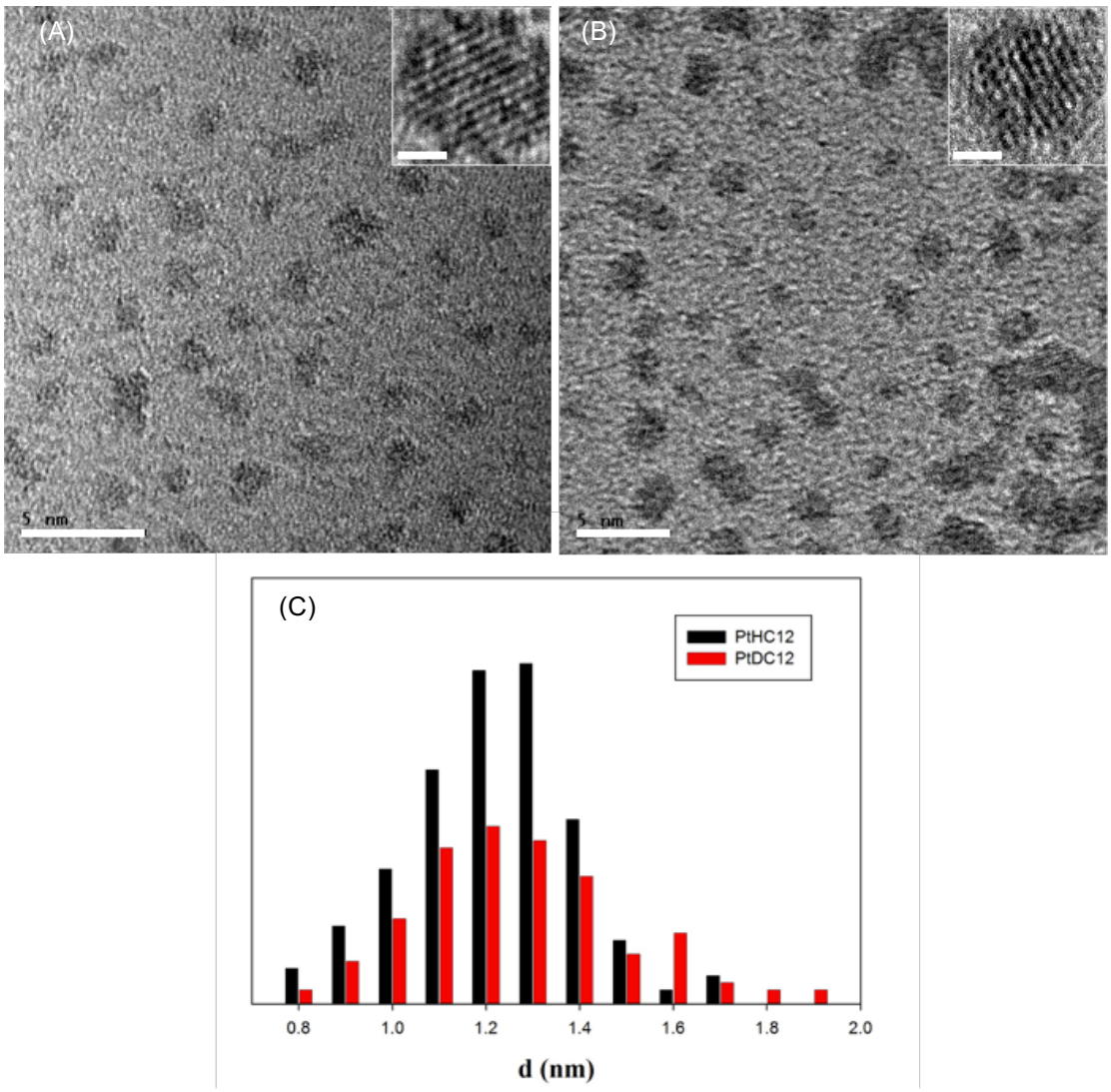

Figure 2.1. Representative TEM micrographs of (A) PtHC12 and (B) PtDC12 nanoparticles. Insets are the corresponding high-resolution images which show the nanoparticle lattice fringes that are consistent with Pt(111). (C) Core size histograms where the average core size is estimated to be 1.3 ± 0.2 nm for both samples.

As manifested in TEM measurements (Figure 2.1), both PtHC12 and PtDC12 nanoparticles were dispersed rather well without apparent agglomeration, suggesting sufficient protection of the nanoparticles by the self-assembly of the alkyne ligands on platinum colloid surface, as observed previously.[14] Statistical analysis based on more than 150 nanoparticles showed that both samples were of 1.3 ± 0.2 nm in diameter, with the majority of the nanoparticles in the range of 1.0 to 1.5 nm. Moreover, clearly defined lattice fringes can be seen in high-resolution TEM studies where the interplanar

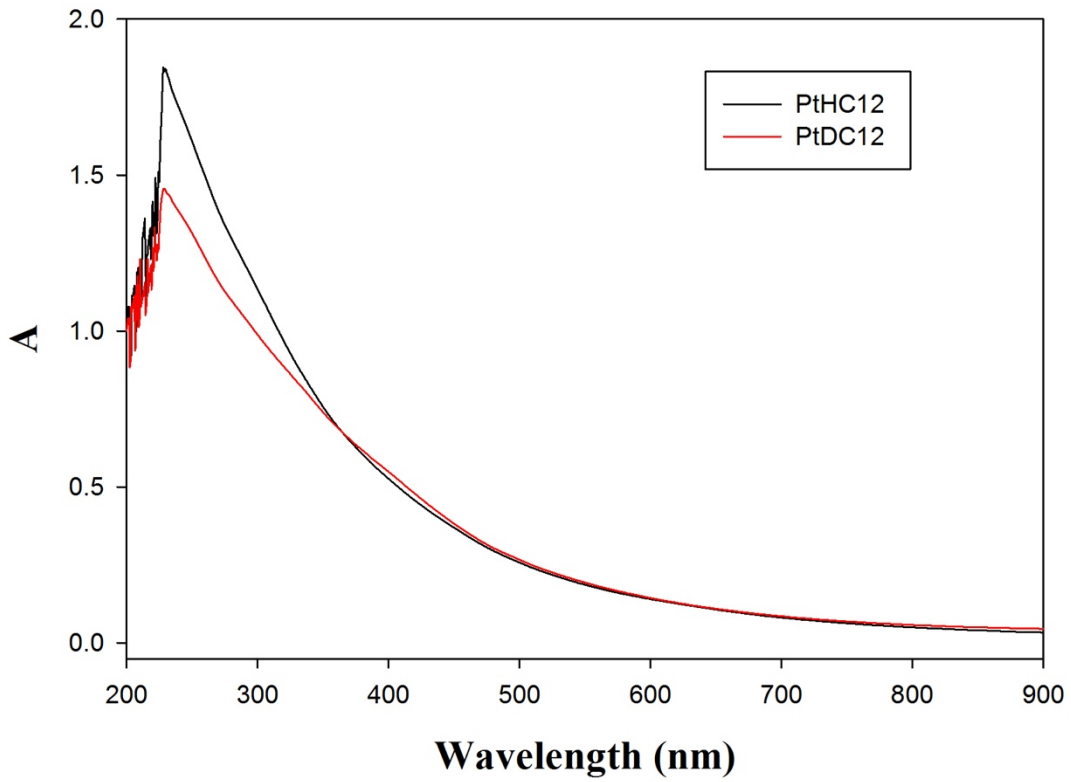

Figure 2.2. UV-vis absorption spectra of PtHC12 (black) and PtDC12 (red) nanoparticles in CH_2Cl_2.

distance of 0.232 nm is consistent with that of the Pt(111) crystalline planes (PDF Card 4-802). The optical properties of both nanoparticles were also consistent with prior results.[14] For instance, whereas only featureless UV-vis absorption profiles were observed (Figure 2.2), both nanoparticles displayed apparent photoluminescence emissions (Figure 2.3), with an excitation maximum and the corresponding emission maximum at 350 and 440 nm for PtHC12, 360 and 450 nm for PtDC12, that were analogous to those of diacetylene derivatives (−C≡C−C≡C−). This was ascribed to intraparticle charge delocalization between

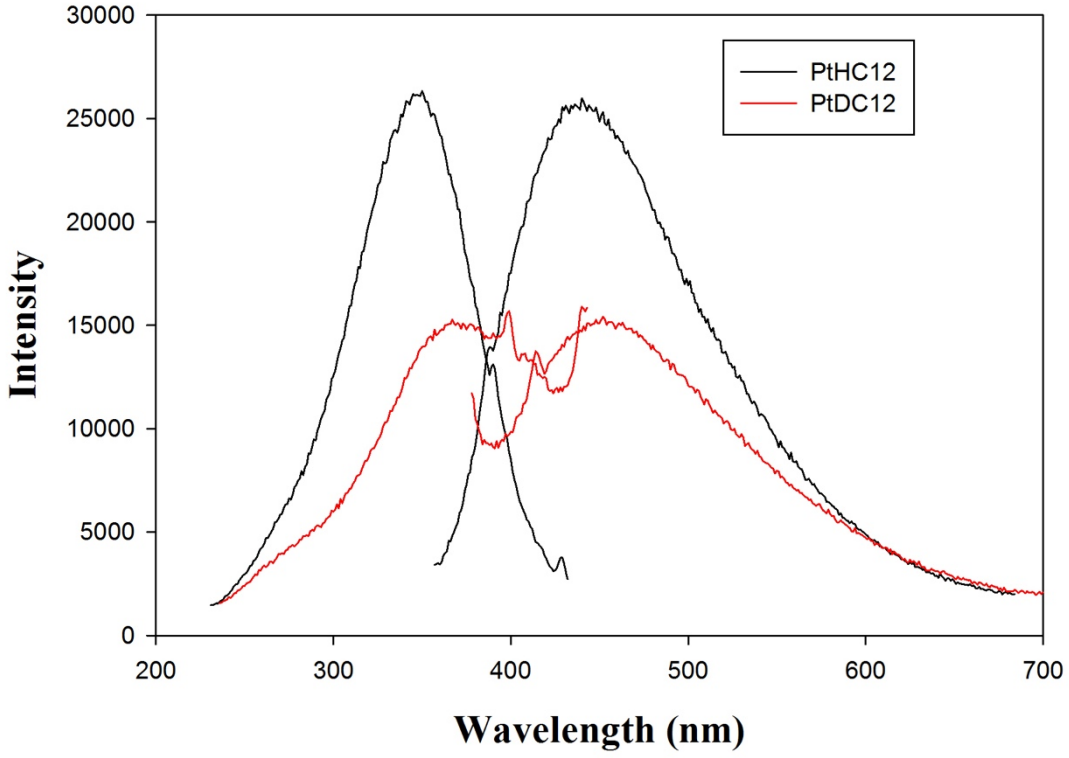

Figure 2.3. Photoluminescne spectra of PtHC12 (black) and PtDC12 (red) nanoparticles in CH_2Cl_2.

the particle-bound acetylene moieties, as observed before for noble metal nanoparticles functionalized with acetylene derivatives.[4, 5, 15]

As mentioned above, in prior studies, the self-assembly of n-alkynes on metal nanoparticles was thought to involve the formation of a dynamic equilibrium between metal-vinylidene (M=C=CH–) and metal-actylide (M–C≡) + metal–hydride (M–H) bonds (Scheme 1). These were first examined by FTIR measurements. From Figure 2.4, several characteristic bands can be identified

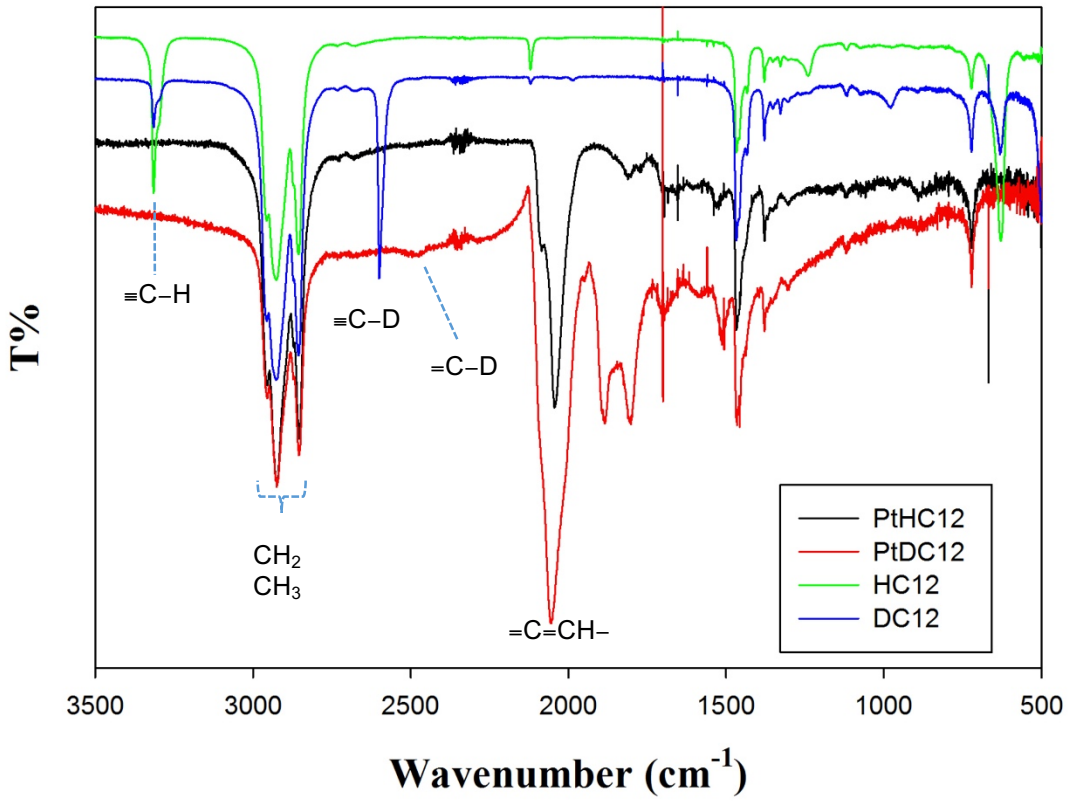

Figure 2.4. FTIR spectra of PtHC12 (black) and PtDC12 (red) nanoparticles, along with monomeric HC12 (green) and DC12 (blue) ligands.

for the HC12 monomers (green curve), 3315 cm^{-1} for the terminal ≡C–H vibration, 2120 cm^{-1} for the C≡C vibrations, and multiple vibration bands at 2956, 2927, and 2853 cm^{-1} that arose from the $-CH_2-$ and $-CH_3$ vibrations of the hydrocarbon chains. DC12 monomers (blue curve) displayed similar characteristics, except that the terminal ≡C–D vibration appeared at 2600 cm^{-1} (the fact that the 3315 cm^{-1} band remained visible was because not all alkynyl

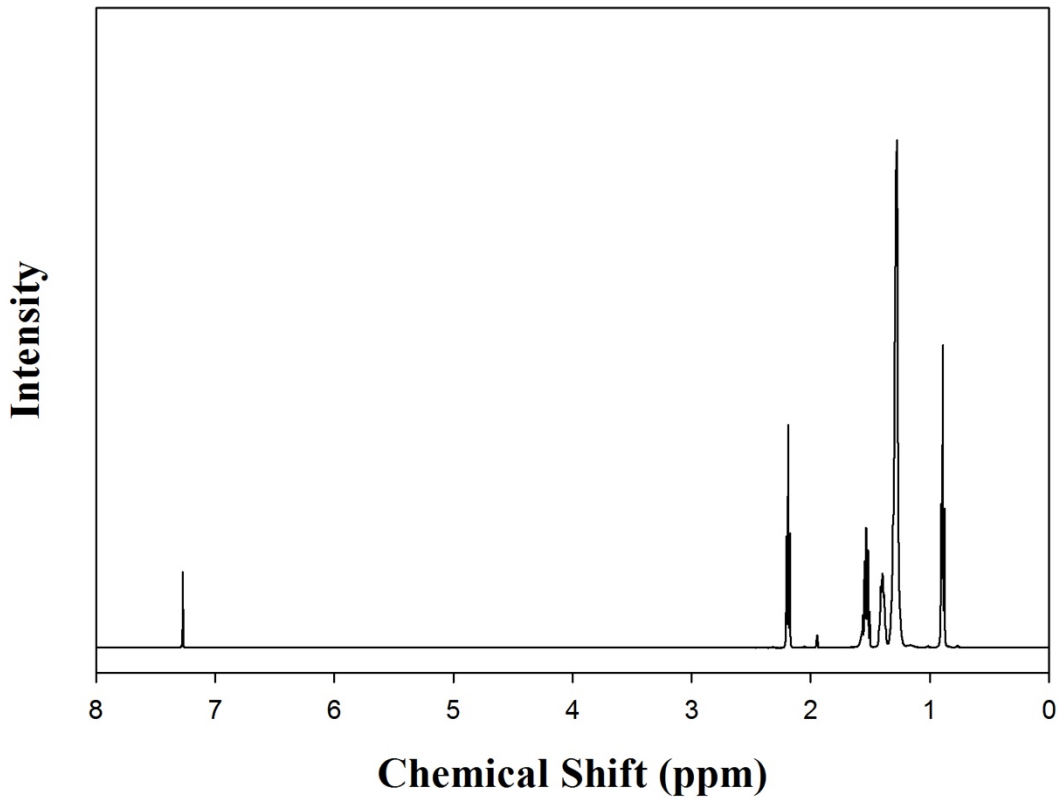

Figure 2.5. ^{1}H NMR spectrum of DC12 in $CDCl_3$. Based on the integrated peak areas of the terminal ≡C–**H** (1.95 ppm) and C**H**$_3$ (0.89 ppm) protons, it is estimated that 95% of protons are replaced with ≡C–**D**.

protons were replaced by the deuterium atoms,[11] as shown in Figure 2.5. When the ligands were self-assembled onto Pt nanoparticle surfaces, for both PtHC12 and PtDC12 nanoparticles the $-CH_2-$ and $-CH_3$ vibrations remained virtually unchanged, and the ≡C−H and ≡C−D vibrational bands vanished completely. Furthermore, PtHC12 exhibited a vibrational band at 2047 cm^{-1}, a red-shift of 73 cm^{-1} from that of monomeric C≡C stretch. Previously this was accounted for by the formation of conjugated Pt−C≡ interfacial bonds that led to intraparticle charge delocalization and hence a diminishing bonding order of the C≡C moiety, with additional contributions from Pt−H bonds on the nanoparticle surface (Scheme 1).[14] For PtDC12, this band appeared at an almost identical position of 2051 cm^{-1}; yet no vibrational band was observed around 1450 cm^{-1} that is anticipated for the Pt−D bonds.[16, 17] Instead, a new band emerged at around 2475 cm^{-1} for PtDC12, which is in good agreement with vinyl carbon deuterium (=C−D) stretch.[18, 19] Taken together, these results strongly suggest the formation of the metal−vinylidene interfacial structure, rather than the metal−acetylide + metal−hydride linkages, at the metal-ligand interface (Scheme 1).

Consistent results were obtained in NMR measurements, as shown in Figure 2.6. From the ^{1}H NMR spectra, one can see that both PtHC12 (black) and PtDC12 (red) nanoparticles exhibited two prominent broad bands at 0.89 and 1.26 ppm, which can be assigned to the terminal methyl (C**H**$_3$) and (partial)

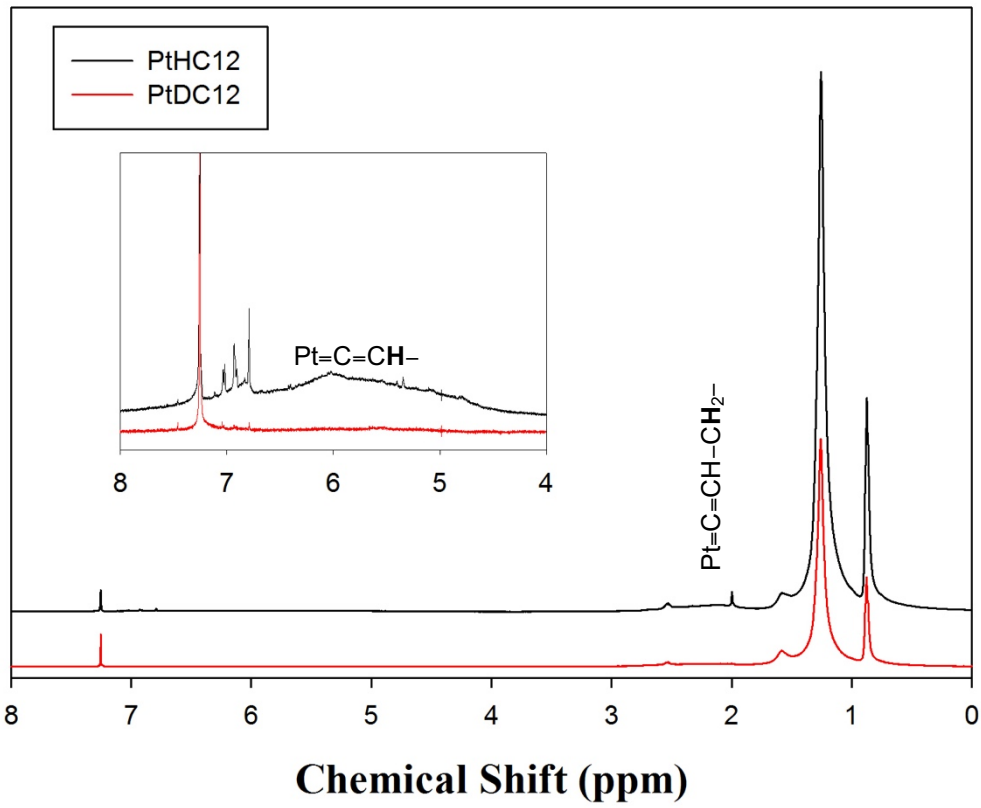

Figure 2.6. ^{1}H NMR spectra of PtHC12 (black) and PtDC12 (red) nanoparticles in $CDCl_3$. Inset is the zoom-in of the region between 4 and 8 ppm.

methylene (C**H**$_2$) protons of the HC12 (black) and DC12 (red) ligands, respectively. Notably, the absence of sharp features at these two peaks indicates the successful attachment of the ligands onto the nanoparticle surface, and both Pt nanoparticles were spectroscopically clean and free of excess ligands[20] (the peaks at 1.56, 2.01, and 7.26 ppm are due to protons from residual solvents of water, acetonitrile, and chloroform, respectively). In addition, two broad bands can be identified at 2.10 and 6.01 ppm for both nanoparticles. Of these, the peak

at 2.10 ppm can be ascribed to the protons of the α-carbon of Pt–vinylidene (Pt=C=CH–C**H**$_2$–), whereas the peak at 6.01 ppm is consistent with the vinylidene protons (Pt=C=C**H**–). Importantly, for the PtHC12 nanoparticles, the ratio of the integrated peak areas between the vinylidene and α-methylene protons was calculated to be 0.95:2, close to the theoretical value of 1:2 (if all the interfacial structures adopt the Pt=C=C configuration), again, consistent with the formation of Pt–vinylidene (Pt=C=C) rather than Pt–acetylide (Pt–C≡C)

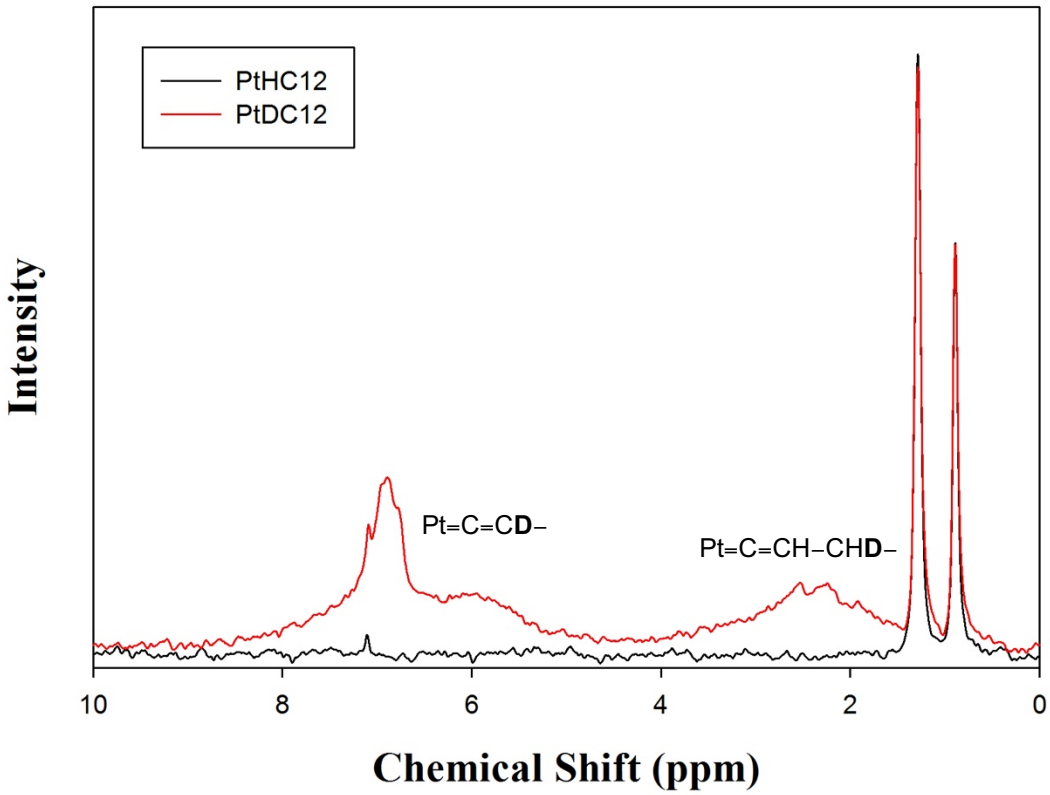

Figure 2.7. ^{2}H NMR spectra of PtHC12 (black) and PtDC12 (red) nanoparticles in n-hexane-d_{14}.

interfacial structure on the Pt nanoparticle surface, in agreement with the FTIR results (Figure 2.4). Such a ratio was significantly lower for the PtDC12 nanoparticles at only 0.1:2, due to the replacement of the vinylidene proton with deuterium (Figure 2.5).

Further structural information was obtained in ^{2}H NMR measurements. As shown in Figure 2.7, the PtHC12 nanoparticle showed two sharp peaks at 0.89 and 1.28 ppm, which arose from the methyl and methylene deuteriums of n-hexane, respectively. In sharp contrast, in addition to these solvent peaks, PtDC12 nanoparticles exhibited two broad bands within the range of 5 to 8 ppm, and 1.5 to 3.5 ppm: the former is consistent with the vinylidene deuterium (Pt=C=C**D**−), while the latter might be ascribed to methylene deuterium (Pt=C=CH−CH**D**−) produced by hydrogen/deuterium migration due to the sigmatropic reaction.[21] These results further confirmed the formation of Pt−vinylidene (Pt=C=CH−) interfacial structure, in good agreement with the results from FTIR.

2.5 Conclusions

In summary, using isotopically labelled alkyne ligands, FTIR and NMR spectroscopic measurements confirmed that when alkynes self-assembled on metal nanoparticle surfaces, the interfacial bonding structures primarily entailed metal−vinylidene linkages.

2.6 References

1. Chen, S.W., Z.H. Zhao, and H. Liu, *Charge Transport at the Metal-Organic Interface.* Annual Review of Physical Chemistry, Vol 64, 2013. **64**: p. 221-245.
2. Chen, W., et al., *Carbene-functionalized ruthenium nanoparticles.* Chemistry of Materials, 2006. **18**(22): p. 5253-5259.
3. Crudden, C.M., et al., *Ultra stable self-assembled monolayers of N-heterocyclic carbenes on gold.* Nature Chemistry, 2014. **6**(5): p. 409-414.
4. Chen, W., et al., *Alkyne-Protected Ruthenium Nanoparticles.* J. Phys. Chem. C, 2010. **114**: p. 18146–18152.
5. Kang, X.W., et al., *Alkyne-Stabilized Ruthenium Nanoparticles: Manipulation of Intraparticle Charge Delocalization by Nanoparticle Charge States.* Angewandte Chemie-International Edition, 2010. **49**(49): p. 9496-9499.
6. Kang, X., et al., *Alkyne-functionalized ruthenium nanoparticles: ruthenium-vinylidene bonds at the metal-ligand interface.* J Am Chem Soc, 2012. **134**(3): p. 1412-1415.
7. Maity, P., et al., *Binding Motif of Terminal Alkynes on Gold Clusters.* Journal of the American Chemical Society, 2013. **135**(25): p. 9450-9457.
8. Maity, P., et al., *Organogold Clusters Protected by Phenylacetylene.* Journal of the American Chemical Society, 2011. **133**(50): p. 20123-20125.
9. Bianchini, C., et al., *Metal Hydride Alkynyl -] Metal Vinylidene Rearrangements Occurring in Both Solid-State and Solution - Role of the 1-Alkyne Substituent in Determining the Relative Stability of Pi-Alkyne, Hydride*

Alkynyl, and Vinylidene Forms at Cobalt. Organometallics, 1991. **10**(10): p. 3697-3707.

10. Silvestre, J. and R. Hoffmann, *Hydrogen Migration in Transition-Metal Alkyne and Related Complexes.* Helvetica Chimica Acta, 1985. **68**(6): p. 1461-1506.
11. Bew, S.P., et al., *Mild Reaction Conditions for the Terminal Deuteration of Alkynes.* Organic Letters, 2012. **14**(2): p. 456-459.
12. Yu, Y., et al., *Identification of a Highly Luminescent Au-22(SG)(18) Nanocluster.* Journal of the American Chemical Society, 2014. **136**(4): p. 1246-1249.
13. Hu, P.G., et al., *Nanoparticle-Mediated Intervalence Charge Transfer: Core-Size Effects.* Angewandte Chemie-International Edition, 2016. **55**(4): p. 1455-1459.
14. Liu, K., et al., *Platinum nanoparticles functionalized with acetylene derivatives: Electronic conductivity and electrocatalytic activity in oxygen reduction.* Journal of Electroanalytical Chemistry, 2013. **688**: p. 143-150.
15. Hu, P.G., et al., *Platinum Nanoparticles Functionalized with Ethynylphenylboronic Acid Derivatives: Selective Manipulation of Nanoparticle Photoluminescence by Fluoride Ions.* Langmuir, 2014. **30**(18): p. 5224-5229.
16. Pliskin, W.A. and R.P. Eischens, *Infrared Spectra of Hydrogen and Deuterium Chemisorbed on Platinum.* Zeitschrift für Physikalische Chemie, 1960. **24**(1_2): p. 11.

17. Toya, T., *Theory of Hydrogen Adsorption on Platinum.* Journal of the Research Institute for Catalysis Hokkaido University, 1962. **10**(3).

18. Nikow, M., M.J. Wilhelm, and H.L. Dai, *Vibrational Modes of the Vinyl and Deuterated Vinyl Radicals.* Journal of Physical Chemistry A, 2009. **113**(31): p. 8857-8870.

19. Wu, Y.J., et al., *Infrared absorption spectra of vinyl radicals isolated in solid Ne.* Journal of Chemical Physics, 2008. **128**(20).

20. Hostetler, M.J., et al., *Alkanethiolate gold cluster molecules with core diameters from 1.5 to 5.2 nm: Core and monolayer properties as a function of core size.* Langmuir, 1998. **14**(1): p. 17-30.

21. Connelly, N.G., et al., *Electron-Transfer-Induced Interconversion of Alkyne and Vinylidene Chromium Complexes - a Quantitative Study.* Journal of the American Chemical Society, 1995. **117**(49): p. 12202-12208.

Chapter 3

Platinum Nanoparticles Functionalized with Ethynylphenylboronic Acid Derivatives: Selective Manipulation of Nanoparticle Photoluminescence by Fluoride Ions

3.1 Abstract

Platinum nanoparticles functionalized with 4-ethynylphenylboronic acid pinacol ester (Pt–EPBAPE) were successfully synthesized by a simple chemical reduction procedure. Because of the formation of conjugated metal–ligand interfacial linkages, the resulting nanoparticles exhibited apparent photoluminescence arising from the nanoparticle-bound acetylene moieties that behaved analogously to diacetylene derivatives. Interestingly, the nanoparticle photoluminescence was markedly quenched upon the addition of fluoride ions (F^-). In contrast, significantly less or virtually no change was observed with a variety of other anions such as Cl^-, Br^-, I^-, NO_3^-, HSO_4^-, $H_2PO_4^-$, ClO_4^-, BF_4^-, and PF_6^-. The high selectivity toward fluoride ion is most probably because of the strong specific affinity of the boronic acid moiety to fluoride. The formation of B–F bonds led to the conversion of Bsp^2 to Bsp^3, as manifested in ^{11}B NMR measurements, which impacted the intraparticle charge delocalization between the particle-bound acetylene moieties and hence the nanoparticle photoluminescence.

3.2 Introduction

Organically capped transition-metal nanoparticles represent a unique class of functional materials that may be used as novel building blocks in diverse applications such as nanoelectronics, catalysis, and chemical and biological sensing.[1-5] This is largely motivated by the ready decoration of the nanoparticle surface with multiple/diverse functional moieties. In addition, the electronic interactions between the particle-bound functional moieties may be deliberately manipulated by the

metal–ligand interfacial bonding interactions, leading to the emergence of unprecedented optical and electronic properties. In particular, it has been demonstrated that with conjugated metal–ligand interfacial bonds, extensive intraparticle charge delocalization occurs between the nanoparticle-bound functional moieties, which thus behave analogously to the dimeric counterparts.[6-10] For instance, for metal nanoparticles stabilized by the self-assembly of acetylene derivatives, the nanoparticles exhibit well-defined photoluminescence that is consistent with that of diacetylene derivatives.[9, 11] More importantly, thanks to the extended conjugation within the nanoparticles, specific interactions of the nanoparticles with target analytes may lead to signal propagation/amplification and hence enhanced detection sensitivity, as manifested in the photoluminescence detection of nitroaromatics and lead ions ($Pb2^{+}$) by pyrene-functionalized ruthenium nanoparticles.[12, 13] This is the primary motivation of the present study which is focused on the sensitive and selective manipulation of nanoparticle photoluminescence by deliberate functionalization of platinum nanoparticles with boronic acid derivatives that react selectively with fluoride ions (F^{-}).

The specific interactions between fluoride and boronic acid have been very well-known and used rather extensively for the development of chemical and biological sensors.[14-19] The general mechanism involves the formation of strong bonding between fluoride and boron that then leads to an apparent change of the fluorescence emission characteristics. Such a sensing architecture may be exploited for the sensitive and selective manipulation of nanoparticle optoelectronic properties with deliberate

surface chemical functionalization. Within this context, in the present study, we prepared platinum nanoparticles functionalized with 4-ethynylphenylboronic acid pinacol ester which exhibited apparent photoluminescence that was consistent with those of diacetylene derivatives, thanks to the formation of conjugated Pt−C≡/Pt=C=C bonds at the metal–ligand interface.[9, 11] The boronic acid moieties served as the specific binding sites for fluoride ions, which exerted sensitive impacts on the nanoparticle photoluminescence. Importantly, the resulting nanoparticles exhibited excellent selectivity and sensitivity toward fluoride, in comparison with a series of other anions.

3.3 Experimental Section

Chemicals. Platinum chloride ($PtCl_2$, 98%, Alfa Aesar), 4-ethynylphenylboronic acid pinacol ester (EPBAPE, 95%, Sigma-Aldrich), tetra-n-octylammonium bromide (TOABr, 98%, Cole Parmer), tetrabutylammonium fluoride (TBAF, 98%, ACROS), tetrabutylammonium chloride (TBACl, ⩾97%, ACROS), tetrabutylammonium bromide (TBABr, ⩾98%, ACROS), tetrabutylammonium iodide (TBAI, ⩾98%, ACROS), tetrabutylammonium nitrate ($TBANO_3$, 97%, ACROS), tetrabutylammonium hydrogen sulfate ($TBAHSO_4$, 97%, Aldrich), tetrabutylammonium dihydrogen phosphate ($TBAH_2PO_4$, 99%, Aldrich), tetrabutylammonium perchlorate ($TBAClO_4$, TCI America), tetrabutylammonium tetrafluoroborate ($TBABF_4$, ACROS), and tetrabutylammonium hexafluorophosphate ($TBAPF_6$, 98%, Fluka) were used as received. All solvents were obtained from typical

commercial sources and used without further treatment. Water was supplied by a Barnstead Nanopure water system (18.3 MΩ·cm).

Synthesis of Platinum Nanoparticles. In a typical synthesis, 0.1 mmol of $PtCl_2$ were dissolved in a 1 mL concentrated HCl solution at 100 °C for 30 min. The solution was then cooled down to room temperature, into which was added 3 mL of a toluene solution of TOABr (0.1 M) under stirring for 1 h. The H_2O phase was removed and the orange toluene phase was washed with H_2O five times. The obtained toluene solution was reduced to 1 mL by blowing N_2, and 5 mL of THF as well as 0.3 mmol of EPBAPE was added into the toluene solution. Ten milligrams of $NaBH_4$ dissolved in 1 mL of ice-cold H_2O was added into the solution dropwise under magnetic stirring. The appearance of a dark brown color signified the formation of platinum nanoparticles. The solution was stirred for 2 h before the solvents were removed by rotary evaporation. The obtained solids were rinsed with acetonitrile five times, affording purified platinum nanoparticles functionalized by the self-assembly of EPBAPE onto platinum surfaces, as depicted in Scheme 1A. The particles were denoted as Pt–EPBAPE and were found to be readily soluble in organic media such as dichloromethane and dimethylformamide (DMF).

Characterizations. The morphology and sizes of the Pt–EPBAPE nanoparticles were characterized by transmission electron microscopic (TEM) studies (Philips CM300 at 300 kV). More than 200 nanoparticles were measured to obtain a size histogram. ^{11}B NMR spectroscopic measurements were carried out by using concentrated solutions of the nanoparticles in DMF-d_6 with a Varian Unity 500 MHz

NMR spectrometer. Chemical shifts were referenced to $BF_3 \cdot OEt_2$ in $CDCl_3$. FTIR measurements were carried out with a Perkin–Elmer FTIR spectrometer (Spectrum One, spectral resolution 4 cm^{-1}), where the samples were prepared by casting the particle solutions onto a ZnSe disk. Photoluminescence (PL) measurements were carried out with a PTI fluorospectrometer. Typically, 3 mL of a Pt–EPBAPE nanoparticle solution in DMF at a concentration of 0.01 mg/mL was added into a quartz cuvette. A series of calculated amounts of tetrabutylammonium salts (with different anions) were added into the cuvette by a Hamilton microliter syringe and the PL spectra were collected after thorough mixing of the nanoparticle solution.

Scheme 3.1

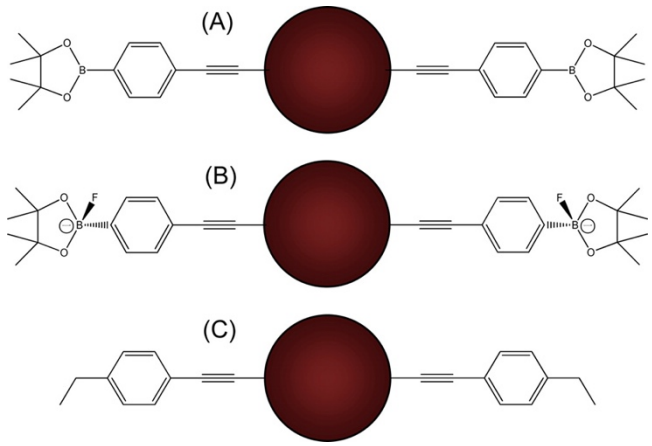

3.4 Results and Discussion

Figure 3.1 depicts a representative TEM micrograph of the Pt–EPBAPE nanoparticles. It can be seen that the nanoparticles were very well dispersed without apparent agglomeration, suggesting sufficient protection of the nanoparticles by the

EPBAPE ligands, as a result of the self-assembly of the acetylene moieties onto platinum nanoparticle surfaces forming Pt–C≡/Pt=C=C bonds (Scheme 3.1A).[20]

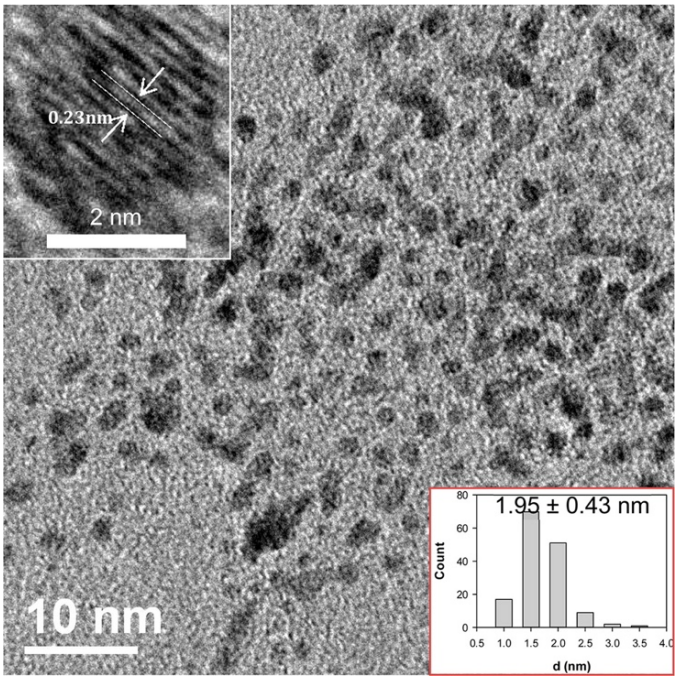

Figure 3.1. Representative TEM micrograph of Pt–EPBAPE nanoparticles. Scale bar 10 nm. Top inset shows a high-resolution image where the lattice fringes with a spacing of 0.23 nm can be identified. Bottom inset shows the corresponding core size histogram.

High-resolution imaging showed very well-defined lattice fringes with a spacing of 0.23 nm that are consistent with the (111) crystal planes of fcc Pt, as manifested in the top figure inset. Additionally, the core size histogram based on a statistical analysis of more than 200 nanoparticles shows that the majority of the nanoparticles are in the narrow range of 1.5 to 2.0 nm in diameter with an average of 1.95 ± 0.43 nm, as depicted in the lower inset.

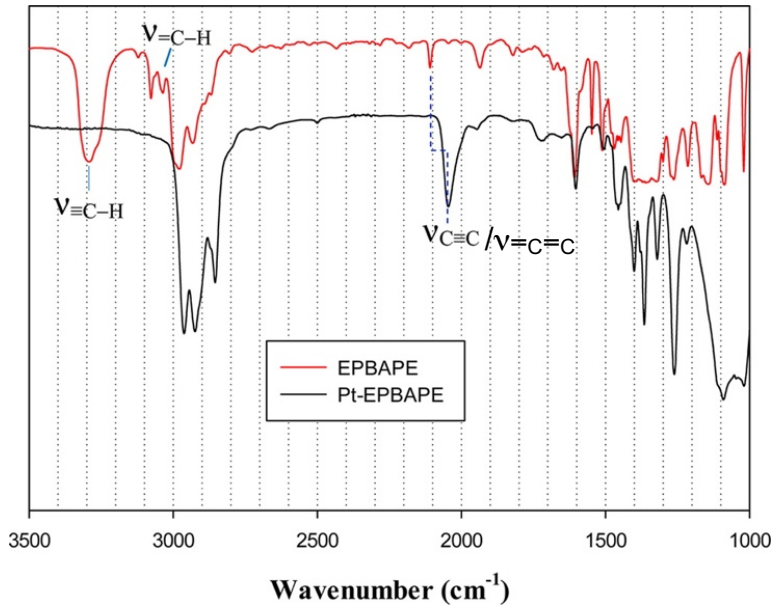

Figure 3.2. FTIR spectra of EPBAPE monomers (red curve) and PtEPBAPE nanoparticles (black curve).

The successful incorporation of the EPBAPE ligands onto the platinum nanoparticle surface was further manifested in FTIR measurements. Figure 3.2 depicts the FTIR spectra of the Pt−EPBAPE nanoparticles (black curve) and the monomeric EPBAPE ligands (red curve). It can be seen that, for the EPBAPE monomers, the terminal ≡C−H vibrational stretch can be clearly identified at 3291 cm^{-1} and the C≡C stretch at 2108 cm^{-1}. Yet for the Pt−EPBAPE nanoparticles, the band at 3291 cm^{-1} vanished, suggesting ready cleavage of the ≡C−H bonds upon the self-assembly of the ligands onto the Pt nanoparticle surface (this also indicates that the nanoparticles were free of excessive monomeric ligands). Meanwhile, the C≡C stretch was found to red-shift to 2046 cm^{-1}, which may be mainly ascribed to the formation of Pt=C=C interfacial bonds. Furthermore, whereas the aromatic =C−H vibrations were rather

apparent between 3000 and 3100 cm^{-1} with the monomeric ligands, no vibrational features were observed above 3000 cm^{-1} with the Pt–EPBAPE nanoparticles. This may also be accounted for by the intraparticle charge delocalization due to the conjugated Pt=C=C bonds where the =C–H vibrations red-shifted and became overlapped with the methyl vibrations (2800–3000 cm^{-1})-notably, the peak at 2850 cm^{-1} became substantially intensified. Similar behaviors have also been observed previously with nanoparticles functionalized with other acetylene derivatives.[20]

Because of extensive intraparticle charge delocalization, the resulting Pt–EPBAPE nanoparticles exhibited apparent PL characteristics, akin to diacetylene derivatives.[20] As depicted by the black curves in Figure 3.3, despite a low concentration of only 0.01 mg/mL in DMF, the Pt–EPBAPE nanoparticles display an intense well-defined excitation peak at 335 nm and an emission one at 406 nm. Interestingly, from panel (A), one can see that, upon the addition of TBAF, the Pt–EPBAPE nanoparticles exhibited an apparent diminishment of the photoluminescence. For instance, at a TBAF concentration of 0.67 mM, the PL intensity of the Pt–EPBAPE nanoparticles decreased by more than 40%. Similar but much less drastic diminishments were observed in the presence of $TBAH_2PO_4$ and TBAI, as depicted in panels (B) and (C), respectively. In contrast, virtually no change of the nanoparticle PL was seen with the addition of TBABr (panel D) and other tetrabutylammonium salts that included TBACl, $TBANO_3$, $TBAHSO_4$, $TBAClO_4$, $THABF_4$, and $TBAPF_6$ (E–J). These observations suggest high sensitivity and selectivity of the nanoparticle PL to fluoride ions.

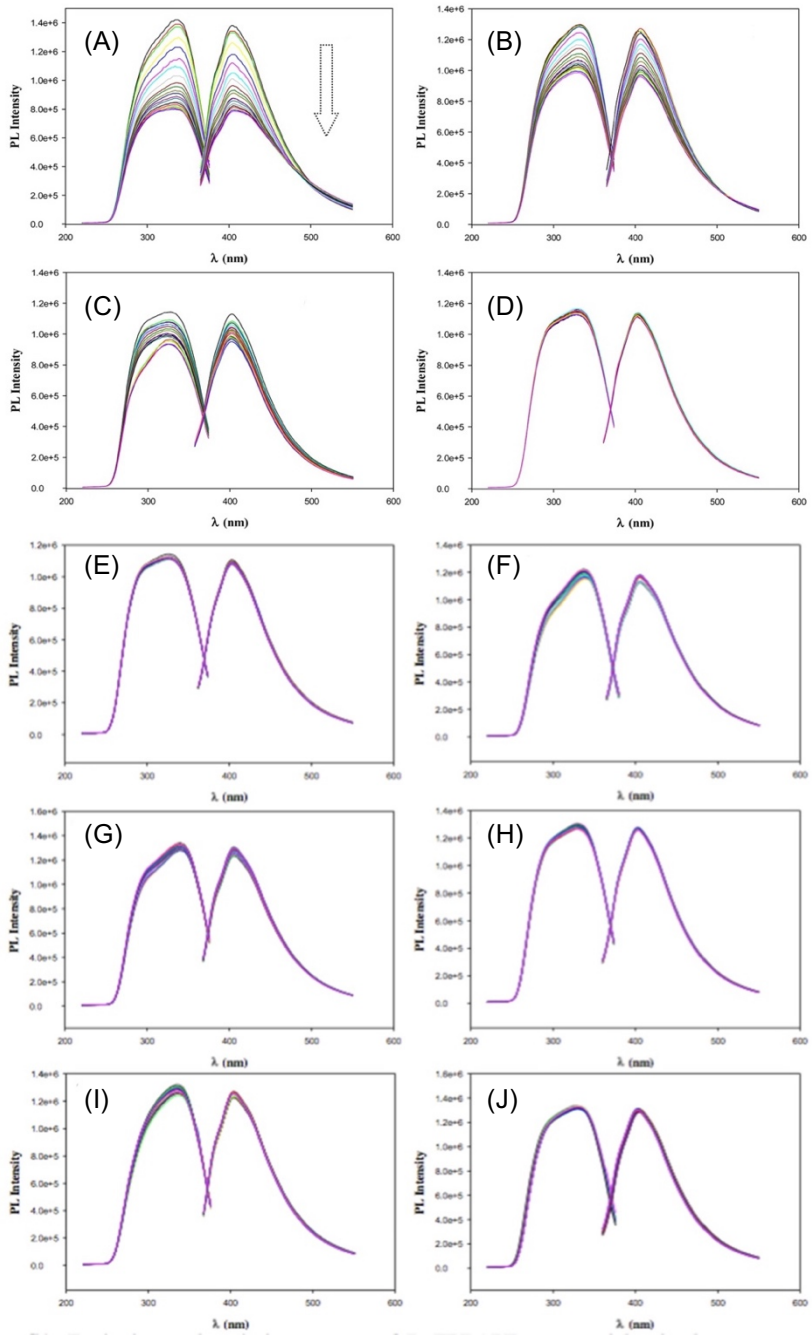

Figure 3.3. Excitation and emission spectra of Pt–EPBAPE nanoparticles in the presence of tetrabutylammonium salts at various concentrations up to 0.67 mM (concentration increment 33 μM): (A) TBAF, (B) $TBAH_2PO_4$, (C) TBAI, (D) TBABr, (E) TBACl, (F) $TBANO_3$, (G) $TBAHSO_4$, (H) $TBAClO_4$, (I) $THABF_4$, and (J) $TBAPF_6$. Initial concentration of the nanoparticles was 0.01 mg/mL in DMF.

Notably, with the addition of a large excess of TBAF, the emission intensity at

406 nm exhibited further diminishment and concurrently a new emission peak started to emerge at a longer wavelength position of 460 nm and the intensity increased accordingly, leading to the appearance of an isoemission point around 435 nm in the

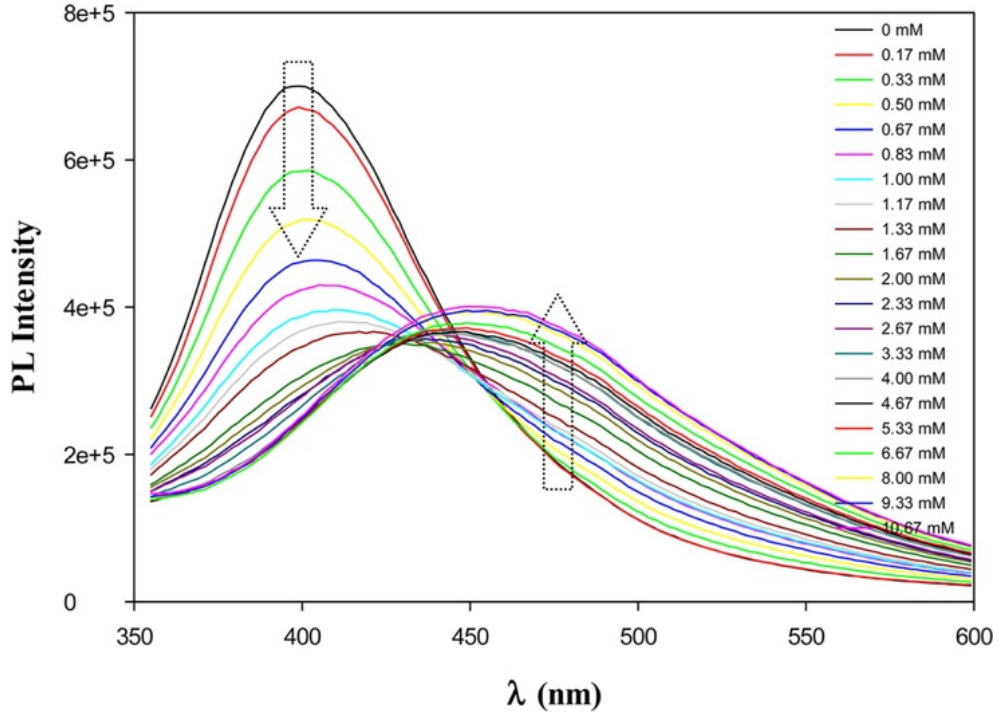

Figure 3.4. Photoluminescence emission spectra of Pt–EPBAPE nanoparticles (6 μg/mL in DMF) with the addition of TBAF up to 10.67 mM. Excitation wavelength was set at 335 nm.

emission profiles (Figure 3.4). In a previous study of ratiometric fluorescence sensing of fluoride ions by an asymmetric bidentate receptor containing a boronic acid and imidazolium group,[19] an isoemission point was clearly identified at 406 nm in acetonitrile with the addition of various amounts of fluoride ions. This may be ascribed to the unique interactions between fluoride ions and the sp^2 B in the boronic acid moieties of Pt–EPBAPE.[18, 19, 21-25] As shown in Scheme 3.1A, the B atom of the

EPBAPE ligand possesses an sp^2 trigonal planar geometry with an empty p orbital perpendicular to the plane of the phenyl ring, allowing the boron atom to be conjugated with the phenyl carbons and hence involved in the intraparticle charge delocalization between the particle-bound acetylene moieties. Note that the boron atoms of such a feature are good electron receptors (nucleophiles) and the binding of fluoride ions into

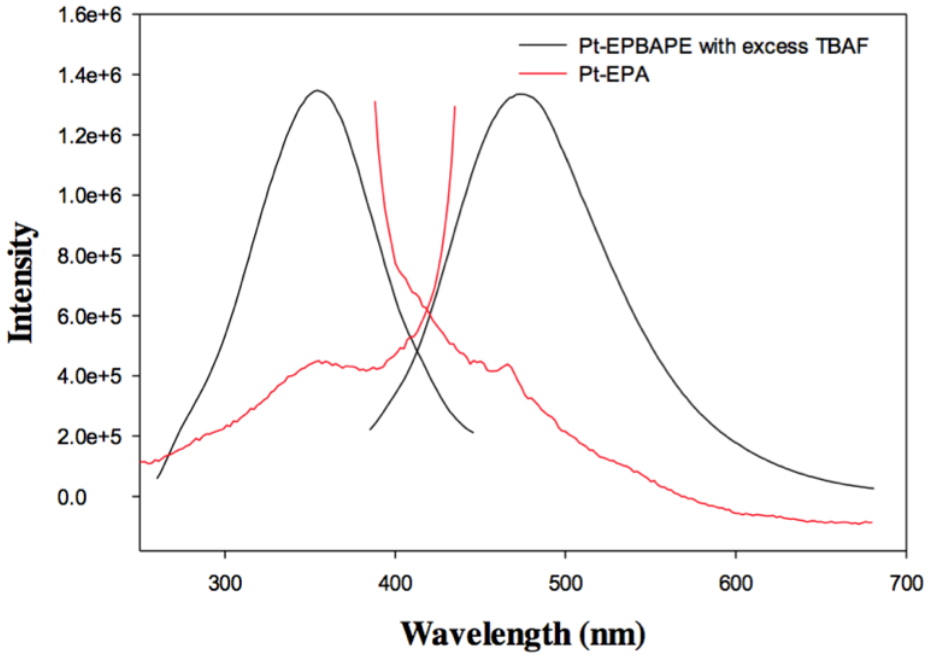

Figure 3.5. Excitation and emission spectra of Pt–EPBAPE nanoparticles with the addition of a large excess of TBAP, along with those of Pt–EPA nanoparticles in DMF. The excitation and emission peaks can both be identified at 355 nm and 467 nm, respectively.

the vacant site most likely induces a change of the molecular geometry and hybridization of the boron atoms to sp^3, as shown in Scheme 1B. The sp^3 boron is no longer able to participate in the conjugation between the particle-bound phenylacetylene groups, leading to an increase of the energy of the HOMO level and hence a red shift of the emission peak position.[23, 26] In fact, one may notice that,

after reactions with an excess of TBAF, the PL characteristics (exaction and emission peak energies) of the Pt–EPBAPE nanoparticles started to resemble those of platinum nanoparticles functionalized with 4-ethylphenylacetylene (Pt–EPA, Scheme 3.1C), as depicted in Figure 3.5.

With the addition of $TBAH_2PO_4$ and TBAI, whereas the quenching of the nanoparticle PL was apparent, the origin was most likely different. These two anions are known to adsorb rather strongly on platinum surfaces.[27, 28] Thus, it is most likely that the diminishment of the nanoparticle PL intensity was due to partial desorption of EPBAPE ligands from the nanoparticle surface. In fact, precipitation of nanoparticles

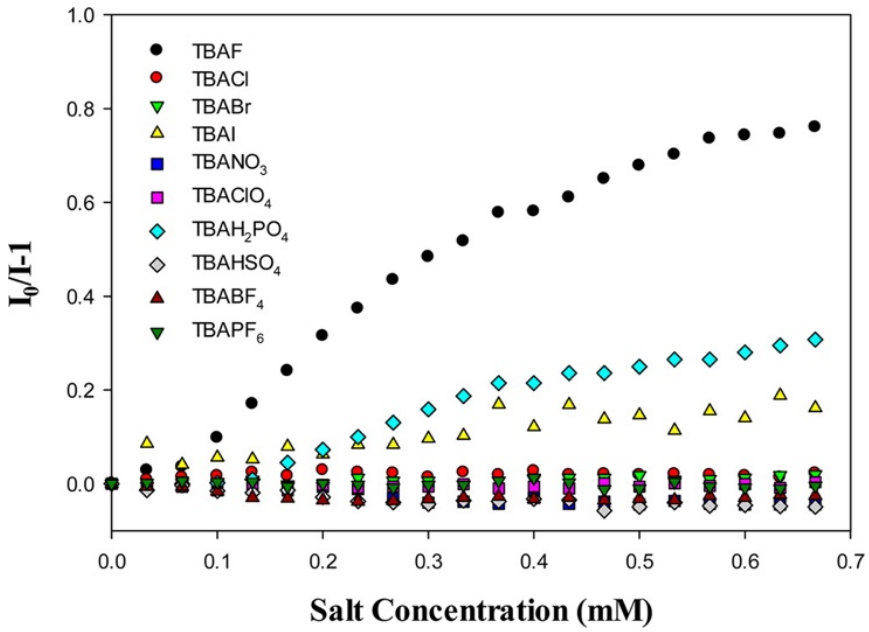

Figure 3.6. Stern–Volmer plots of the photoluminescence emission intensity of Pt–EPBAPE nanoparticles with the addition of various amounts of tetrabutylammonium salts.

was observed with the addition of a large excess of these anions into the nanoparticle solution.

The high sensitivity and selectivity of the PL quenching of the Pt–EPBAPE nanoparticles by F^- can be further manifested by the Stern–Volmer analysis,[29]

$$I_0/I - 1 = K[A] \qquad (3.1)$$

where I_0 and I are the nanoparticle PL intensities in the absence and presence of quencher A, respectively, [A] is the concentration of quencher A, and K is the Stern-Volmer quenching constant. Figure 3.6 depicts the Stern–Volmer plots in the presence of various tetrabutylammonium salts at concentrations up to 0.67 mM. There are at least two aspects that warrant attention. First, the Pt–EPBAPE nanoparticle exhibited almost linear diminishment of the photoluminescence intensity in the low anion concentration regime, and the quenching constant varies significantly with the specific quencher, as manifested by the slopes of the Stern–Volmer plots, which are summarized in Table 3.1. One can see that the quenching constant for F^- is estimated to be 1.71×10^3 M^{-1}, more than 3 times that of $H_2PO_4^-$ (0.53×10^3 M^{-1}), 6 times that of I^- (0.28×10^3 M^{-1}), and about 2 orders of magnitude greater than those of Br^- (0.029×10^3 M^{-1}), Cl^- (0.010×10^3 M^{-1}), and ClO_4^- (0.008×10^3 M^{-1}). For the rest of the series (NO_3^-, HSO_4^-, BF_4^-, and PF_6^-), the nanoparticle PL was virtually unchanged, and thus the quenching constant was essentially zero. Second, the lowest anion concentration that leads to an observable change of the nanoparticle PL intensity also varies markedly, which is estimated to be 0.051 mM for F^-, 0.12 mM for $H_2PO_4^-$, and 0.20 mM for I^- (the rest was not measured as the nanoparticle PL was virtually

unchanged). Taken together, these observations highlight the specific binding of F^- among the series of anions to the boronic acid moieties (Scheme 3.1B).

The specific binding of fluoride ions and the boronic acid moieties was further confirmed by ^{11}B NMR measurements. Figure 3.7 shows the ^{11}B NMR spectra of the Pt–EPBAPE nanoparticles in the (A) absence and (B and C) presence of various amounts of TBAF in DMF-d_6. From curve (A) of the Pt–EPBAPE nanoparticles alone,

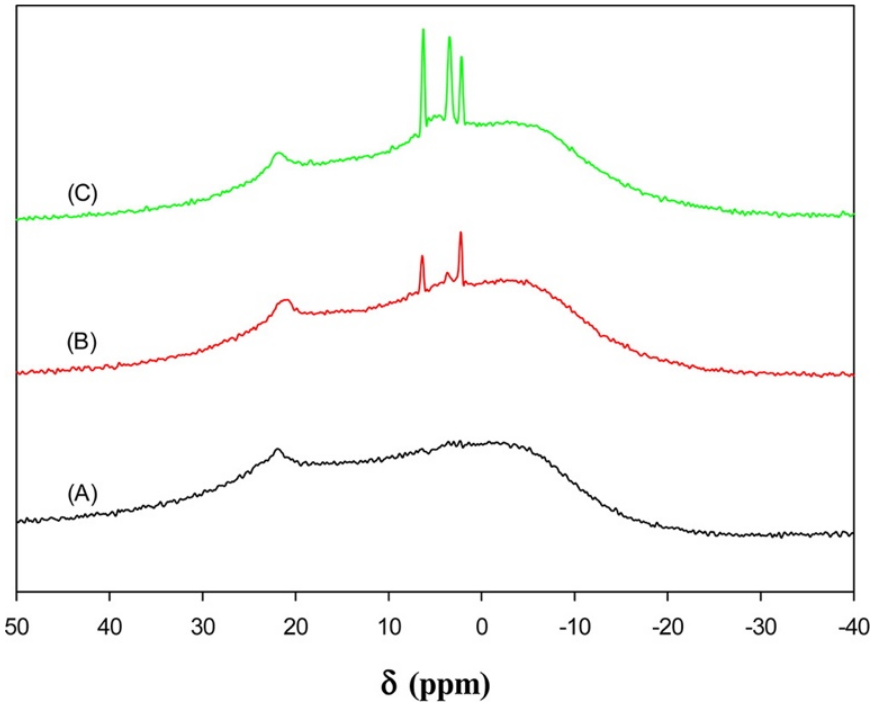

Figure 3.7. ^{11}B NMR spectra of Pt–EPBAPE nanoparticles at a concentration of 37.5 mg/mL in DMF-d_6 in the (A) absence and presence of various amounts of TBAF: (B) 42.4 mM and (C) 277.3 mM.

a relatively broad peak centered at ca. 20.9 ppm can be identified, which may be ascribed to the sp^2 B in the boronic acid moieties (the broad feature from 40 to −20 ppm is due to boron residuals in the NMR glass tubing).[18, 30-33] Upon the addition of TBAF into the nanoparticle solution, the intensity of this peak diminished, and

concurrently several new spectral features started to appear within the range of 6.3–2.2 ppm, which might be ascribed to B sp^3, and the intensity became increasingly intensified with the amount of TBAF added from 42.4 mM in curve (B) to 277.3 mM in curve (C). These behaviors are consistent with the binding of nucleophilic F^- to the empty p orbitals of the boron center of the boronic acid such that the boron centers now became sp^3 hybridized (Scheme 3.1B).[18, 31, 33]

3.5 Conclusions

In this study, platinum nanoparticles functionalized with ethynylphenylboronic acid panicol ester were synthesized by taking advantage of the self-assembly of acetylene moieties onto platinum surfaces forming Pt–C≡/Pt=C=C bonds. The resulting nanoparticles exhibited apparent photoluminescence as a result of the conjugated metal–ligand interfacial bonds whereby the particle-bound acetylene moieties behaved analogously to diacetylene derivatives. Interestingly, the addition of fluoride ions led to apparent diminishment of the nanoparticle photoluminescence. This was accounted for by the specific affinity of fluoride ions to the boronic acid moieties forming stable B–F bonds that impacted the intraparticle charge delocalization. In contrast, significantly less or virtually no change of the nanoparticle photoluminescence was observed with a series of other anions that included Cl^-, Br^-, I^-, NO_3^-, HSO_4^-, $H2PO_4^-$, ClO_4^-, BF_4^-, and PF_6^-, signifying the high selectivity of the nanoparticles toward fluoride ions. The results further highlight the significance of deliberate functionalization of nanoparticle surface in the manipulation of nanoparticle optical and electronic properties.

3.6 References

1. Jeong, Y., et al., *Fabrication of Stable Nanoparticle-Based Colloidal Microcapsules.* Current Organic Chemistry, 2013. **17**(1): p. 49-57.
2. Thaxton, C.S., N.L. Rosi, and C.A. Mirkin, *Optically and chemically encoded nanoparticle materials for DNA and protein detection.* Mrs Bulletin, 2005. **30**(5): p. 376-380.
3. Sardar, R., et al., *Gold Nanoparticles: Past, Present, and Future.* Langmuir, 2009. **25**(24): p. 13840-13851.
4. Perez-Juste, J., et al., *Gold nanorods: Synthesis, characterization and applications.* Coordination Chemistry Reviews, 2005. **249**(17-18): p. 1870-1901.
5. Segev-Bar, M. and H. Haick, *Flexible Sensors Based on Nanoparticles.* Acs Nano, 2013. **7**(10): p. 8366-8378.
6. Chen, W., et al., *Nanoparticle-mediated intervalence transfer.* Journal of the American Chemical Society, 2008. **130**(36): p. 12156-12162.
7. Chen, W., et al., *Pyrene-Functionalized Ruthenium Nanoparticles: Novel Fluorescence Characteristics from Intraparticle Extended Conjugation.* Journal of Physical Chemistry C, 2009. **113**(39): p. 16988-16995.
8. Deming, C.P., et al., *Alkyne-Protected AuPd Alloy Nanoparticles for Electrocatalytic Reduction of Oxygen.* Chemelectrochem, 2015. **2**(11): p. 1719-1727.

9. Kang, X., et al., *Alkyne-functionalized ruthenium nanoparticles: ruthenium-vinylidene bonds at the metal-ligand interface.* J Am Chem Soc, 2012. **134**(3): p. 1412-1415.

10. Deming, C.P., et al., *Nitrene-functionalized ruthenium nanoparticles: Selective manipulation of nanoparticle electronic conductivity by vinyl derivatives.* Sensors and Actuators B-Chemical, 2014. **194**: p. 319-324.

11. Kang, X.W. and S.W. Chen, *Electronic conductivity of alkyne-capped ruthenium nanoparticles.* Nanoscale, 2012. **4**(14): p. 4183-4189.

12. Chen, W., et al., *Pyrene-Functionalized Ruthenium Nanoparticles as Effective Chemosensors for Nitroaromatic Derivatives.* Analytical Chemistry, 2010. **82**(2): p. 461-465.

13. Kang, X.W., et al., *Intraparticle Charge Delocalization of Carbene-Functionalized Ruthenium Nanoparticles Manipulated by Selective Ion Binding.* Langmuir, 2011. **27**(20): p. 12636-12641.

14. Nishimura, T., et al., *A simple visual sensor with the potential for determining the concentration of fluoride in water at environmentally significant levels.* Chemical Communications, 2013. **49**(5): p. 478-480.

15. Huang, S., et al., *The Progress of Selective Fluorescent Chemosensors by Boronic Acid.* Current Medicinal Chemistry, 2012. **19**(16): p. 2621-2637.

16. Mader, H.S. and O.S. Wolfbeis, *Boronic acid based probes for microdetermination of saccharides and glycosylated biomolecules.* Microchimica Acta, 2008. **162**(1-2): p. 1-34.

17. Wang, W., X.M. Gao, and B.H. Wang, *Boronic acid-based sensors.* Current Organic Chemistry, 2002. **6**(14): p. 1285-1317.

18. Galbraith, E. and T.D. James, *Boron based anion receptors as sensors.* Chem Soc Rev, 2010. **39**(10): p. 3831-42.

19. Xu, Z., et al., *Ratiometric Fluorescence Sensing of Fluoride Ions by an Asymmetric Bidentate Receptor Containing a Boronic Acid and Imidazolium Group.* European Journal of Organic Chemistry, 2009(18): p. 3058-3065.

20. Liu, K., et al., *Platinum nanoparticles functionalized with acetylene derivatives: Electronic conductivity and electrocatalytic activity in oxygen reduction.* Journal of Electroanalytical Chemistry, 2013. **688**: p. 143-150.

21. Dusemund, C., K.R.A.S. Sandanayake, and S. Shinkai, *Selective fluoride recognition with ferroceneboronic acid.* Journal of the Chemical Society, Chemical Communications, 1995(3): p. 333.

22. Cooper, C.R., *Selective fluorescence detection of fluoride using boronic acids.* Chemical Communications, 1998(13): p. 1365-1366.

23. Nicolas, M., et al., *Boronic ester-substituted triphenylamines as new Lewis base-sensitive redox receptors.* Journal of Electroanalytical Chemistry, 2000. **482**(2): p. 211-216.

24. Melaimi, M. and F.P. Gabbai, *A heteronuclear bidentate Lewis acid as a phosphorescent fluoride sensor.* Journal of the American Chemical Society, 2005. **127**(27): p. 9680-9681.

25. Liu, X.Y., D.R. Bai, and S. Wang, *Charge-Transfer Emission in Nonplanar Three-Coordinate Organoboron Compounds for Fluorescent Sensing of Fluoride.* Angewandte Chemie, 2006. **118**(33): p. 5601-5604.

26. Oehlke, A., et al., *Nitro-substituted stilbeneboronate pinacol esters and their fluoro-adducts. Fluoride ion induced polarity enhancement of arylboronate esters.* Journal of Organic Chemistry, 2007. **72**(12): p. 4328-4339.

27. Gisbert, R., G. Garcia, and M.T.M. Koper, *Adsorption of phosphate species on poly-oriented Pt and Pt(111) electrodes over a wide range of pH.* Electrochimica Acta, 2010. **55**(27): p. 7961-7968.

28. Shu, Z.X. and S. Bruckenstein, *Iodine Adsorption Studies at Platinum.* Journal of Electroanalytical Chemistry, 1991. **317**(1-2): p. 263-277.

29. Lakowicz, J.R., *Principles of Fluorescence Spectroscopy.* Principles of Fluorescence Spectroscopy.

30. Phillips, W.D., H.C. Miller, and E.L. Muetterties, *B11 Magnetic Resonance Study of Boron Compounds.* Journal of the American Chemical Society, 1959. **81**(17): p. 4496-4500.

31. Mooney, E.F. and P.H. Winson, *Self-Association of Dibenzyl Phenylboronate.* Chemical Communications, 1967(7): p. 341-&.

32. Kubo, Y., et al., *Detection of anions using a fluorescent alizarin-phenylboronic acid ensemble.* Chemical Communications, 2005(22): p. 2846-2848.

33. Reetz, M.T., C.M. Niemeyer, and K. Harms, *Crown Ethers with a Lewis Acidic Center - a New Class of Heterotopic Host Molecules.* Angewandte Chemie-International Edition in English, 1991. **30**(11): p. 1472-1474.

Chapter 4

Nanoparticle-Mediated Intervalence Charge Transfer: Core-Size Effects

4.1 Abstract

Two types of platinum nanoparticles (NPs) functionalized with ethynylferrocene were prepared. The subnanometer-sized NPs ($Pt_{10}eFc$) showed semiconductor-like characteristics with a bandgap of about 1.0 eV, and the other was metal-like with a core size of about 2 nm ($Pt_{314}eFc$) and no significant bandgap. IR spectroscopic measurements showed a clear red-shift of the C≡C/=C=C and ferrocenyl ring =C−H vibrational energies with increasing particle core size owing to enhanced intraparticle charge delocalization between the particle-bound ferrocenyl moieties. Electrochemical measurements showed two pairs of voltammetric peaks owing to intervalence charge transfer between the ferrocenyl groups on the nanoparticle surface, which was apparently weaker with $Pt_{10}eFc$ than with $Pt_{314}eFc$. Significantly, the former might be markedly enhanced with UV photoirradiation owing to enhanced nanoparticle electronic conductivity, whereas no apparent effects were observed with the latter.

4.2 Introduction

In recent years, it has been found that electronic communication may occur between nanoparticle-bound functional moieties when they are bonded to the nanoparticle surface by conjugated metal−ligand interfacial linkages.[1-11] This leads to the emergence of new optical and electronic properties that are analogous to those of their dimeric derivatives. For instance, when ferrocenyl moieties are bound to ruthenium nanoparticle surfaces by ruthenium–carbene (Ru=C) π bonds, electrochemical measurements exhibit two pairs of voltammetric peaks,[3] consistent with the well-known intervalence charge transfer (IVCT) of biferrocene derivatives

bridged with conjugated chemical linkers.[12-14] Such nanoparticle-mediated intraparticle charge delocalization has also been observed with other functional moieties, and facilitated by the conducting metal cores. For instance, electron injection into the metal cores by chemical reduction is found to readily enhance intraparticle charge delocalization, whereas opposite effects are observed by chemical oxidation.[11] In these earlier studies, the nanoparticle metal cores are typically over 2 nm in diameter, and hence exhibit electronic conductivity analogous to that of the corresponding bulk metal.[15]

However, when the core size of the metal nanoparticles diminishes to the subnanometer regime, comparable to the Fermi wavelength of an electron, the nanoparticles become molecule-like, with the emergence of a nonzero HOMO–LUMO bandgap, akin to semiconductor materials.[15] Such metal nanoclusters, consisting of several to a few tens of atoms, show extraordinary high specific surface area, significantly modified optical properties, and discrete energy levels.[16-18] Thus, an immediate question arises. When functional moieties are bonded to subnanometer-sized particle surfaces, will effective electronic communication still occur between them? This is the primary motivation of the present work.

Herein, we compare the IVCT behaviors of two ferrocene-functionalized Pt nanoparticles, one with a core size about 2 nm (metal-like) and the other in the subnanometer regime (semiconductor-like). The ferrocenyl moieties were incorporated onto the nanoparticle surface by ligand-exchange reactions of triphenylphosphine (PPh_3)-stabilized platinum nanoparticles with ethynylferrocene (eFc) by taking

advantage of the strong affinity of acetylene (C≡C) group to transition-metal surfaces forming metal–acetylide/metal–vinylidene (M–C≡C/M=C=C) interfacial bonds.[10, 11, 19]

4.3 Experimental Section

Chemicals. Platinum(II) chloride ($PtCl_2$, 73% Pt, ACROS), hydrochloric acid (HCl, 12.1 M, Fisher Scientific), tetra-n-octylammonium bromide (TOABr, 98%, Cole Parmer), triphenylphosphine (PPh_3, 99%+, ACROS), ethynylferrocene (eFc, 97%, ACROS), sodium acetate (NaOAc, MC&B), and sodium carbonate (Na_2CO_3, 99%, Fisher Scientific) were all used as received without any further purification. Solvents were purchased at the highest purity available from typical commercial sources and also used as received. Tetra-n-butylammonium perchlorate (TBAP, 98%, TCI America) was used after recrystallization 4 times in ethanol. Water was supplied by a Barnstead Nanopure water system (18.3 MΩ·cm).

Synthesis of ethynylferrocene-functionalized platinum (PteFc) nanoparticles. Platinum nanoparticles of two different sizes were prepared. The synthetic procedure for subnanometer-sized Pt clusters was adopted from previous reports.[20-22] In a typical reaction, $PtCl_2$ (0.1 mmol) was dissolved in HCl (1 mL, 12.1 M) at 100 °C. The solution was then added to a toluene solution of TOABr (0.3 mmol in 30 mL) and stirred vigorously for 1 h. The organic phase was collected and magnetically stirred overnight after the addition of 0.3 mmol PPh_3, generating a white precipitate. The white precipitate was then collected by centrifugation and dispersed in an ethanol–water (30 mL:5 mL) mixture, into which CO was bubbled for 3 h. The

solution was then under stirring for 12 h leading to the production of an orange precipitate. This signified the formation of subnanometer-sized Pt clusters. The orange precipitate was collected by centrifugation, rinsed three times with ethanol to remove water, and then washed five times with CH_2Cl_2 and isooctane (1:70) to remove excessive TOABr and PPh_3, affording purified PPh_3-stablized Pt ($PtPPh_3$) subnanoclusters. The subnanoclusters were then mixed with eFc (0.3 mmol) in CH_2Cl_2 (1 mL) and stirred for 2 d, before the solution was dried by bubbling N_2 and washed with isooctane five times to remove monomeric ligands, leading to the preparation of ferrocene-functionalized Pt subnanoclusters.

To prepare larger Pt nanoparticles capped with eFc, a different procedure was used. First, PPh_3-protected platinum nanoparticles were synthesized by the self-assembly of PPh_3 onto the surface of "bare" Pt colloids that were synthesized by thermolytic reduction of $PtCl_2$ in 1,2-propanediol.[3-6] Experimentally, $PtCl_2$ (0.1 mmol) was dissolved in HCl (3 mL, 12.1 M). The solution was then condensed to 1 mL, neutralized with sodium carbonate, and centrifuged to remove unsolved salts. The supernatant and NaOAc (1 mmol, 82 mg) were added to 1,2-propanediol (100 mL). The mixed solution was heated at 165 °C under vigorous stirring for 1 h. Toluene (50 mL) with PPh_3 (0.3 mmol; threefold molar excess of $PtCl_2$) was added after the solution was cooled down to room temperature, and the mixed solution was stirred magnetically for overnight. The toluene phase was then collected, dried by rotary evaporation, and rinsed extensively with excessive acetonitrile to obtain PPh_3-capped Pt nanoparticles. Exchange reactions with eFc were carried out in a similar fashion by adding a

calculated amount of eFc into the $PtPPh_3$ nanoparticle solution in CH_2Cl_2 under magnetic stirring for 2 d, affording larger PteFc nanoparticles.

Characterization. The morphology and sizes of the PteFc nanoparticles were characterized by transmission electron microscopic (TEM) studies (Philips CM300 at 300 kV). UV-Vis spectra were collected with a UNICAM ATI UV4 spectrometer. FTIR measurements were carried out with a PerkinElmer FTIR spectrometer (Spectrum One, spectral resolution 4 cm^{-1}); the samples were prepared by casting the particle solutions onto a NaCl disk. ^1H NMR spectroscopic measurements were carried out by using concentrated nanoparticle solutions in CD_2Cl_2 with a Varian Unity 500 MHz NMR spectrometer. MALDI-TOF mass spectra were acquired by using an Ettan MALDI-TOF Pro (Amersham Biosciences) spectrometer equipped with a standard UV nitrogen laser (337 nm). The ions formed by the irradiation of laser were detected by a linear/reflectron time-of-flight mass spectrometer. The accelerating voltage was held at 20 kV and positive-ion mode was used. The platinum cluster solutions in CH_2Cl_2 was mixed with the DCTB matrix (10 mg mL^{-1} in CH_2Cl_2) and was then applied to the sample plate and air-dried. The laser beam was focused on a stainless steel plate where the samples were spotted.

Electrochemistry. Voltammetric measurements were carried out either in the dark or under UV photoirradiation (254 nm) with a CHI 440 electrochemical workstation. A polycrystalline gold disk electrode (sealed in glass tubing) was used as the working electrode. A Ag/AgCl wire and a Pt coil were used as the reference and counter electrodes, respectively. Note that experimentally the reference electrode was

calibrated against the formal potential of the ferrocenium/ferrocene couple (Fc^+/Fc). The gold electrode was first polished with alumina slurries of 0.5 μm and then cleaned by sonication in 0.1 m HNO_3, H_2SO_4, and Nanopure water successively. Prior to data collection, the electrolyte solution was deaerated by bubbling ultrahigh-purity N_2 for at least 20 min and blanketed with a nitrogen atmosphere during the entire experimental procedure.

4.4 Results and Discussions

The structure of the subnanometer-sized PteFc clusters was first examined with MALDI-TOF mass spectrometric measurements. From the mass spectrum in Figure 4.1, a broad peak is observed centered around 2000 Da, suggesting that on average the nanoclusters consist of a Pt_{10} core, and the spikes at 1371, 1498, 1887, and 2092 Da

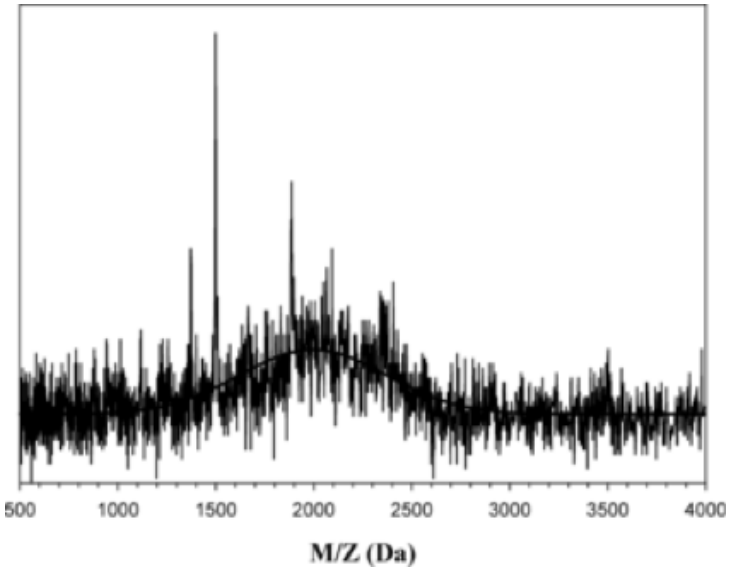

Figure 4.1. MALDI-TOF mass spectrum of Pt10eFc nanoclusters. Noisy curve: experimental data; smooth curve: Gaussian fit.

indicates that along with Pt_{10} clusters, Pt_7 is another major population in the sample. This corresponds to a core size of less than 1 nm for the Pt clusters.[23] Note that whereas conventional TEM is not a reliable method for evaluating nanoparticles in the subnanometer size range,[24] the Pt nanoparticles prepared by thermolysis of $PtCl_2$ i n 1,2-propanediol are much larger and can be readily characterized by TEM measurements. A representative TEM image of the nanoparticles is given in Figure 4.2. It can be clearly seen that the nanoparticles were dispersed very well without apparent aggregation, indicating effective protection of the nanoparticles by the capping ligands. Furthermore, the Pt nanoparticle core size was estimated to be 2.08 ± 0.37 nm, as manifested by the core size histogram (Figure 4.2 inset), based on a statistical analysis

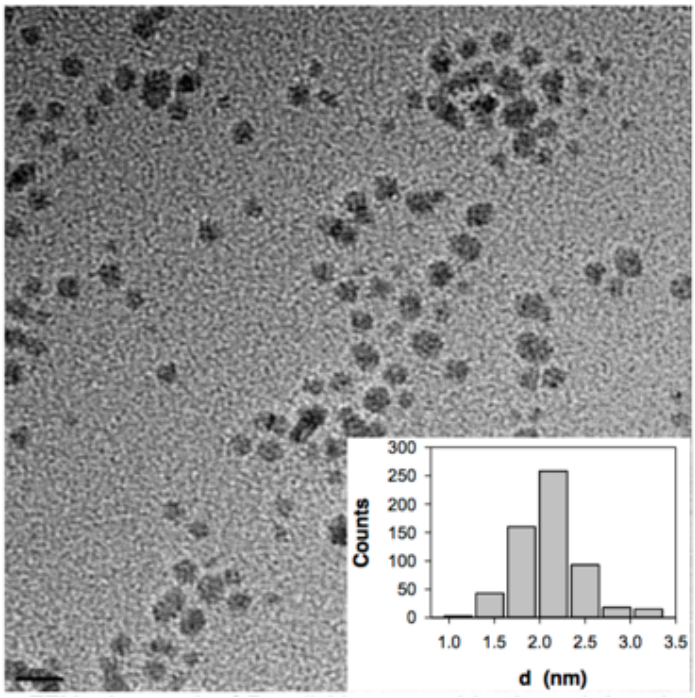

Figure 4.2. Representative TEM micrograph of Pt colloids prepared by thermolytic reduction of H_2PtCl_4 in 1,2-propanediol at 165 ^oC. Scale bar 5 nm. Inset shows the the core size histogram where the average diameter is estimated to be 2.08 ± 0.37 nm.

of more than 100 nanoparticles. Assuming a truncated octahedral structure, the metal core of the nanoparticles was estimated to consist of about 314 Pt atoms.[25] Therefore, these two nanoparticles were referred to as $Pt_{10}eFc$ and $Pt_{314}eFc$, respectively.

It is well-known that when the size of metal nanoparticles diminishes to the subnanometer regime, a non-zero HOMO–LUMO bandgap starts to emerge, as manifested in optical and electrochemical measurements.[15, 26] Figure 4.3 depicts the UV-vis absorption spectra of the $Pt_{10}eFc$ and $Pt_{314}eFc$ nanoparticles. It can be seen that both nanoparticles exhibited a broad absorption band centered at around 3.36 eV (368 nm), arising from the d–d transitions of the ferrocenyl moieties;[27, 28] and for the

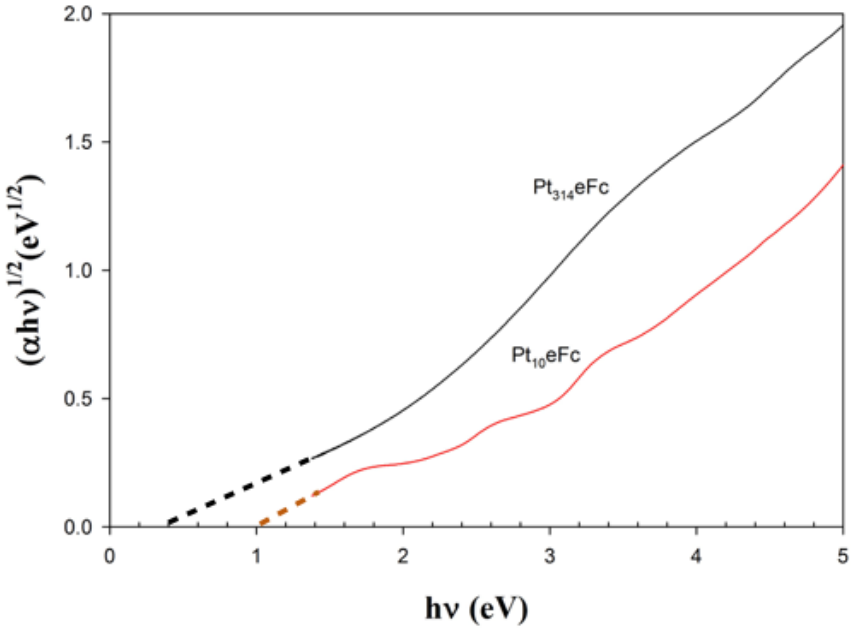

Figure 4.3. UV-vis absorption spectra of the $Pt_{10}eFc$ and $Pt_{314}eFc$ nanoparticles in CH_2Cl_2. α is the optional absorbance and $h\nu$ is the photon energy. Dashed lines are linear extrapolation to the *x*-axis.

Pt_{10}eFc sample, two additional absorption peaks can be identified around 2.62 eV (473 nm) and 1.75 eV (708 nm), which may be ascribed to interband transitions of the subnanometer-sized Pt_{10} clusters.[29-31] In fact, by extrapolating the absorption profiles to the x-axis (dashed curves), the bandgap of the Pt_{10}eFc nanoparticles can be estimated to be 1.0 eV whereas the larger Pt_{314}eFc nanoparticles shows an intercept of only 0.4 eV.

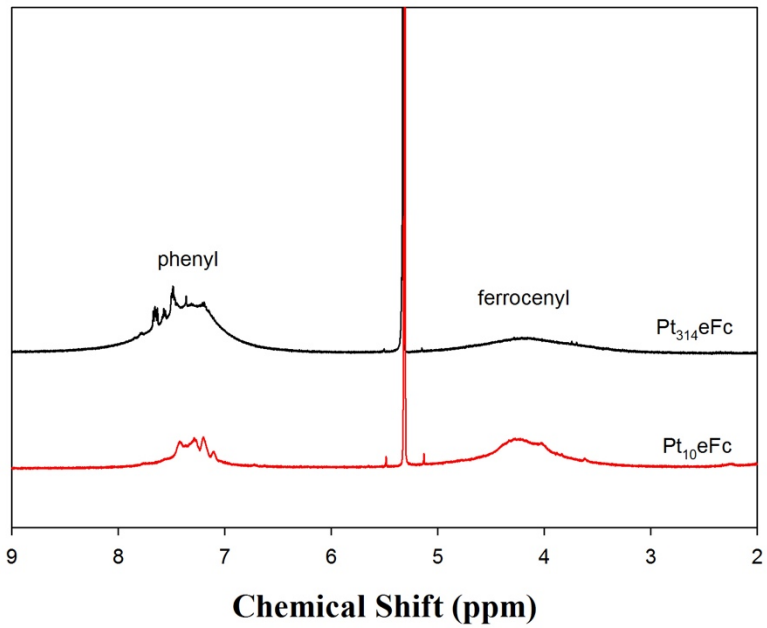

Figure 4.4. ^{1}H NMR spectra of the Pt_{10}eFc and Pt_{314}eFc nanoparticles in CD_2Cl_2.

The incorporation of ferrocenyl moieties onto the nanoparticle surface was confirmed and quantified by ^{1}H NMR measurements. Figure 4.4 shows the ^{1}H NMR spectra of the Pt_{10}eFc and the Pt_{314}eFc nanoparticles. It can be seen that both spectra exhibit two broad peaks centered around 7.45 and 4.25 ppm. The former may be

assigned to the phenyl protons of PPh_3, and the latter to the ferrocenyl protons of eFc, suggesting incomplete replacement of the original PPh_3 ligands by eFc. Furthermore, no alkynyl (≡C−H) protons at 2.71 ppm can be seen in both samples, indicating that both nanoparticles are spectroscopically clean and free of excess free eFc ligands. Furthermore, based on the integrated peak areas of the phenyl and ferrocenyl ring protons, the molar ratio of the eFc and PPh_3 ligands on the nanoparticle surface was estimated to be 4.44:1 for Pt_{10}eFc and 1.14:1 for Pt_{314}eFc.

The successful incorporation of the ferrocenyl ligands onto the nanoparticle surface was also manifested in FTIR measurements. From Figure 4.5, it can be seen that whereas PPh_3 monomers displayed multiple overtones/combination peaks within the range of 1600 to 2000 cm^{-1}, the features diminished markedly with the two nanoparticle samples (along with the phenyl ring =C−H vibration at 3066 cm^{-1}), suggesting a decrease of the PPh_3 concentration. Furthermore, for the eFc monomers, the terminal ≡C−H vibration can be clearly identified at 3292 cm^{-1}, the C≡C stretch at 2109 cm^{-1}, and the ferrocenyl ring =C−H stretch at 3113 cm^{-1}. Yet when the ligands were bound onto Pt nanoparticle surface by ligand-exchange reactions, the sharp peak at 3291 cm^{-1} vanished for both the Pt_{10}eFc and Pt_{314}eFc nanoparticles, indicating ready cleavage of the ≡C−H bond and the formation of Pt−acetylide/Pt−vinylidene (M−C≡C/M=C=C) interfacial bonds at the metal−ligand interface (this also shows that both nanoparticle samples were indeed free of monomeric eFc). [10] Furthermore, the ferrocenyl ring =C−H stretch and the C≡C stretch both exhibited a marked red-shift to 3095 and 2060 cm^{-1} for Pt_{10}eFc, and 3092 and 2024 cm^{-1} for Pt_{314}eFc, respectively.

This may be ascribed to the formation of Pt−acetylide/Pt−vinylidene (Pt−C≡C/Pt=C=C) interfacial bonds and the intraparticle charge delocalization between the particle-bound ferrocene moieties as a result of the conjugated metal-ligand interfacial bonds, as observed previously.[10, 32, 33] Furthermore, the fact that the =C−H and C≡C stretches were at lower energy with the larger $Pt_{314}eFc$ nanoparticles than with the smaller $Pt_{10}eFc$ suggests better conjugation between the ferrocenyl moieties in $Pt_{314}eFc$ than in

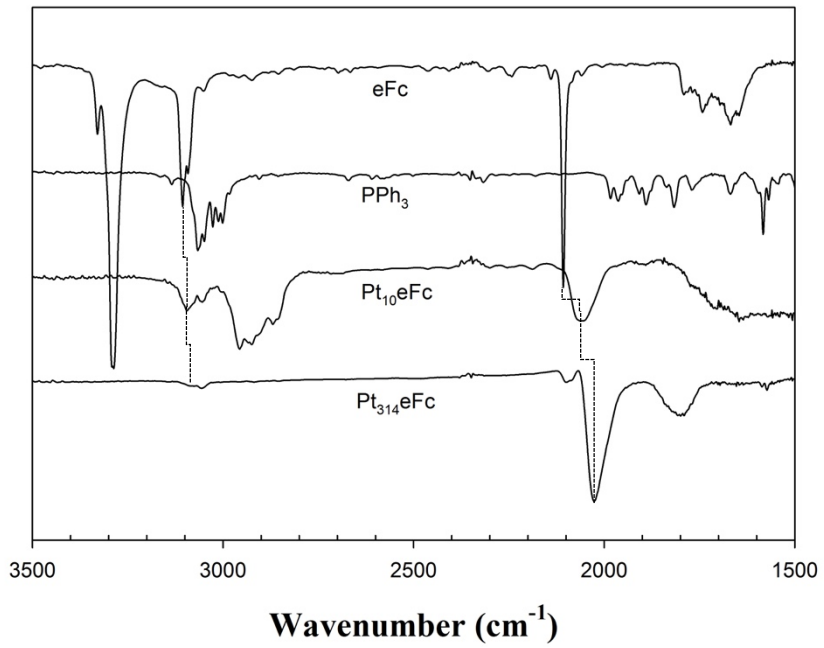

Figure 4.5. FTIR spectra of the $Pt_{10}eFc$, $Pt_{314}eFc$ nanoparticles, and monomeric eFc, PPh_3 ligands.

$Pt_{10}eFc$, most probably because of the nonzero bandgap of the subnanometer-sized metal cores that diminished the electronic conductivity of the nanoclusters, as

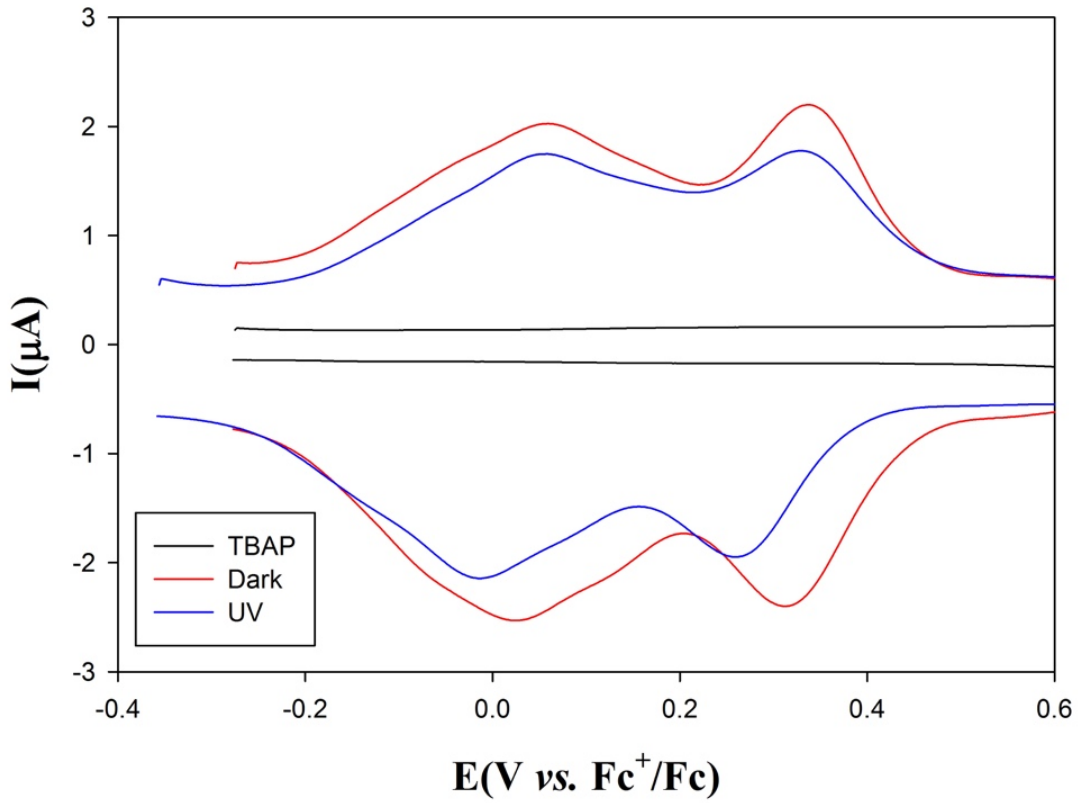

Figure 4.6. SWVs of $Pt_{314}eFc$ nanoparticles at a gold electrode in 0.1 M TBAP in CH_2Cl_2 in the dark and under UV irradiation. Electrode surface areas: 0.87 mm^2. Nanoparticle concentrations: 5 mg mL^{-1}. Increment of potential 2 mV, amplitude 25 mV, frequency 15 Hz.

compared to the large nanoparticles that are anticipated to behave analogously to bulk metal.[15]

Interestingly, the apparent difference of the electronic structure of the nanoparticle metal cores led to marked discrepancy of the nanoparticle electrochemical behaviors. Figure 4.6 and 4.7 depicts the square-wave voltammograms (SWVs) of $Pt_{314}eFc$ (Figure 4.6) and $Pt_{10}eFc$ (Figure 4.7) nanoparticles in the dark and under UV photoirradiation (254 nm, 4.89 eV) with 0.1 M TBAP in CH_2Cl_2. From Figure 4.6, two

pairs of voltammetric peaks (red curves) can be clearly seen in the dark at the formal potentials ($E^{o\prime}$) of +0.042 V and +0.32 V (vs. Fc^+/Fc), in contrast to the featureless profiles observed with TBAP alone (black curves). These may be ascribed to the nanoparticle-mediated intervalence charge transfer of the particle-bound ferrocenyl moieties as a result of the conjugated metal-ligand interfacial bonds, and the peak spacing ($\Delta E^{o\prime}$) of 0.28 V indicates that the nanoparticles behaved analogously to a class II complex as defined by Robin and Day.[3, 34] Consistent results are observed when the solution was exposed to UV irradiation (blue curves), where the two pairs of voltammetric peaks now appeared at +0.021 and +0.30 V with an identical $\Delta E^{o\prime}$ of 0.28 V. This may be accounted for by the lack of dependence of the nanoparticle electronic conductivity on photoirradiation because the metal cores are sufficiently big such that the nanoparticles behaved like the bulk metal.[15]

For the much smaller $Pt_{10}eFc$ particles, markedly different voltammetric responses were seen, as manifested in Figure 4.7. First, whereas there are also two pairs of voltammetric peaks within the potential range −0.4 to +0.6 V when the voltammograms were acquired in the dark (red curves), the peaks can only be resolved by deconvolution at $E^{o\prime}$ = +0.042 and +0.22 V (vs Fc^+/Fc). The peak potential spacing of $\Delta E^{o\prime}$ = 0.18 V suggests that the $Pt_{10}eFc$ nanoparticles fell into the intermediate between a class I and II complex.[3, 34] The fact that $\Delta E^{o\prime}$ is much smaller than that of $Pt_{314}eFc$ signifies reduced intraparticle charge delocalization between the particle-

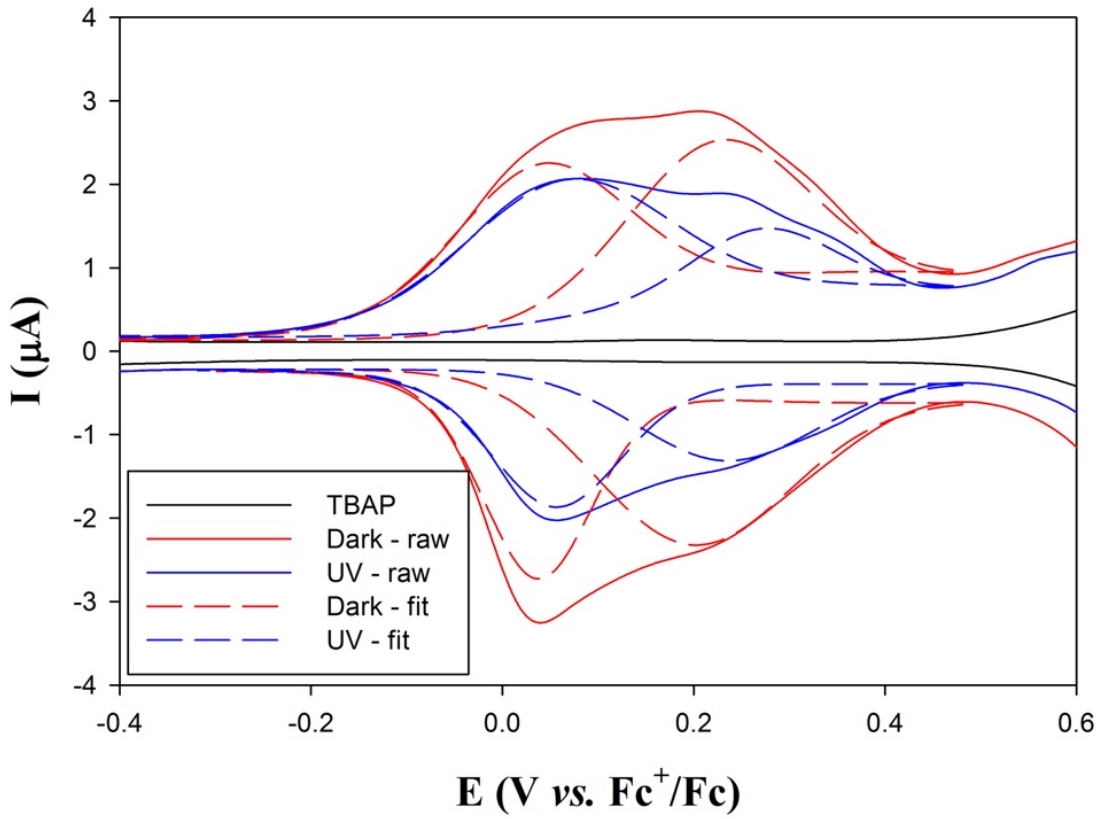

Figure 4.7. SWVs of $Pt_{10}eFc$ nanoparticles at a gold electrode in 0.1 M TBAP in CH_2Cl_2 in the dark and under UV irradiation. Electrode surface areas: 2.41 mm^2. Nanoparticle concentrations: Pt10eFc 2 $mg\,mL^{-1}$. Increment of potential 2 mV, amplitude 25 mV, frequency 15 Hz. Solid curves are experimental data and dashed curves are deconvolution fits.

bound ferrocenyl moieties, which is likely due to the ultrasmall particle core size and semiconductor-like electronic conductivity, akin to the results where the structure of the chemical bridge was found to significantly impact the IVCT of biferrocene derivatives.[14, 35] Interestingly, upon the exposure to UV photoirradiation, the two pairs of voltammetric peaks now appeared at +0.060 and +0.26 V (blue curves), and $\Delta E^{o\prime}$ increased by 20 mV to 0.20 V. This may be accounted for by the photo-enhanced

nanoparticle electronic conductivity,[36] leading to improved intraparticle charge delocalization between the surface ferrocenyl moieties, in contrast to the results of the larger Pt_{314}eFc nanoparticles.

4.5 Conclusions

In summary, the results presented above indicate when the nanoparticle core size diminishes to the subnanometer regime such that an apparent bandgap emerges, IVCT between nanoparticle-bound functional moieties diminishes markedly, in contrast to large nanoparticles where the cores behave like the bulk metal, as manifested in spectroscopic and electrochemical measurements. Yet, because of the semiconductor-like electronic characteristics of the subnanometer-sized clusters, photoirradiation can be used as an effective method to enhance the nanoparticle electronic conductivity and hence intraparticle charge delocalization, whereas no such effects are observed with the large counterparts. This further highlights the unique significance of metal core structures in the manipulation of nanoparticle charge-transfer dynamics.

4.6 References

1. Chen, W., et al., *Intervalence transfer of ferrocene moieties adsorbed on electrode surfaces by a conjugated linkage.* Chemical Physics Letters, 2009. **471**(4-6): p. 283-285.
2. Chen, L.M., et al., *Interfacial reactivity of ruthenium nanoparticles protected by ferrocenecarboxylates.* Physical Chemistry Chemical Physics, 2014. **16**(35): p. 18736-18742.

3. Chen, W., et al., *Nanoparticle-mediated intervalence transfer.* Journal of the American Chemical Society, 2008. **130**(36): p. 12156-12162.

4. Chen, W., et al., *Carbene-functionalized ruthenium nanoparticles.* Chemistry of Materials, 2006. **18**(22): p. 5253-5259.

5. Chen, W., et al., *Pyrene-Functionalized Ruthenium Nanoparticles: Novel Fluorescence Characteristics from Intraparticle Extended Conjugation.* Journal of Physical Chemistry C, 2009. **113**(39): p. 16988-16995.

6. Chen, W., et al., *Pyrene-Functionalized Ruthenium Nanoparticles as Effective Chemosensors for Nitroaromatic Derivatives.* Analytical Chemistry, 2010. **82**(2): p. 461-465.

7. Kang, X.W., et al., *Intraparticle Charge Delocalization of Carbene-Functionalized Ruthenium Nanoparticles Manipulated by Selective Ion Binding.* Langmuir, 2011. **27**(20): p. 12636-12641.

8. Chen, W., S. Pradhan, and S.W. Chen, *Photoluminescence and conductivity studies of anthracene-functionalized ruthenium nanoparticles.* Nanoscale, 2011. **3**(5): p. 2294-2300.

9. Kang, X.W., et al., *Manipulation of Intraparticle Charge Delocalization by Selective Complexation of Transition-Metal Ions with Histidine Moieties.* Analytical Chemistry, 2012. **84**(4): p. 2025-2030.

10. Liu, K., et al., *Platinum nanoparticles functionalized with acetylene derivatives: Electronic conductivity and electrocatalytic activity in oxygen reduction.* Journal of Electroanalytical Chemistry, 2013. **688**: p. 143-150.

11. Kang, X.W., et al., *Alkyne-Stabilized Ruthenium Nanoparticles: Manipulation of Intraparticle Charge Delocalization by Nanoparticle Charge States.* Angewandte Chemie-International Edition, 2010. **49**(49): p. 9496-9499.

12. Ferguson, G., et al., *The redox behaviour of ferrocene molecules .12. The redox behaviour of some bis-ferrocenyl compounds: Crystal and molecular structures of diferrocenylmethane and diferrocenylmethanol.* Journal of Organometallic Chemistry, 1996. **517**(1-2): p. 183-190.

13. Mochida, T., et al., *Biferrocenium salts with magnetite-like mixed-valence iron: coexistence of Fe3+ and Fe2.5+ in the crystal.* Chemical Communications, 2014. **50**(19): p. 2481-2483.

14. Morrison, W.H.K., S.; Hendrickson, D. N., *Polarographic and magnetic susceptibility study of various biferrocene compounds.* Inorganic Chemistry, 1973. **12**: p. 1998-2004.

15. Chen, S.W., et al., *Gold nanoelectrodes of varied size: Transition to molecule-like charging.* Science, 1998. **280**(5372): p. 2098-2101.

16. Link, S., et al., *Visible to infrared luminescence from a 28-atom gold cluster.* Journal of Physical Chemistry B, 2002. **106**(13): p. 3410-3415.

17. El-Sayed, M.A., *Some interesting properties of metals confined in time and nanometer space of different shapes.* Accounts of Chemical Research, 2001. **34**(4): p. 257-264.

18. Empedocles, S. and M. Bawendi, *Spectroscopy of single CdSe nanocrystallites.* Accounts of Chemical Research, 1999. **32**(5): p. 389-396.

19. Chen, W., et al., *Alkyne-Protected Ruthenium Nanoparticles.* Journal of Physical Chemistry C, 2010. **114**(42): p. 18146-18152.

20. Conte, M., et al., *Spin Trapping of Au-H Intermediate in the Alcohol Oxidation by Supported and Unsupported Gold Catalysts.* Journal of the American Chemical Society, 2009. **131**(20): p. 7189-7196.

21. Sharma, R., et al., *NMR Characterization of Ligand Binding and Exchange Dynamics in Triphenylphosphine-Capped Gold Nanoparticles.* Journal of Physical Chemistry C, 2009. **113**(37): p. 16387-16393.

22. Yu, Y., et al., *Identification of a Highly Luminescent Au-22(SG)(18) Nanocluster.* Journal of the American Chemical Society, 2014. **136**(4): p. 1246-1249.

23. Bartlett, P.A., B. Bauer, and S.J. Singer, *Synthesis of Water-Soluble Undecagold Cluster Compounds of Potential Importance in Electron-Microscopic and Other Studies of Biological-Systems.* Journal of the American Chemical Society, 1978. **100**(16): p. 5085-5089.

24. Chen, W. and S.W. Chen, *Oxygen Electroreduction Catalyzed by Gold Nanoclusters: Strong Core Size Effects.* Angewandte Chemie-International Edition, 2009. **48**(24): p. 4386-4389.

25. Hostetler, M.J., et al., *Alkanethiolate gold cluster molecules with core diameters from 1.5 to 5.2 nm: Core and monolayer properties as a function of core size.* Langmuir, 1998. **14**(1): p. 17-30.

26. Yang, Y.Y. and S.W. Chen, *Surface manipulation of the electronic energy of subnanometer-sized gold clusters: An electrochemical and spectroscopic investigation.* Nano Letters, 2003. **3**(1): p. 75-79.

27. Sohn, Y.S., Hendrick.Dn, and H.B. Gray, *Electronic Structure of Metallocenes.* Journal of the American Chemical Society, 1971. **93**(15): p. 3603.

28. Sohn, Y.S., et al., *Single-crystal electronic spectrum of ferrocene at 4.2 degrees K.* Chemical Physics Letters, 1970. **6**(5): p. 499-501.

29. Yuan, X., et al., *Synthesis of Highly Fluorescent Metal (Ag, Au, Pt, and Cu) Nanoclusters by Electrostatically Induced Reversible Phase Transfer.* Acs Nano, 2011. **5**(11): p. 8800-8808.

30. Laaksonen, T., et al., *Quantised charging of monolayer-protected nanoparticles.* Chemical Society Reviews, 2008. **37**(9): p. 1836-1846.

31. Akola, J., et al., *On the structure of thiolate-protected Au-25.* Journal of the American Chemical Society, 2008. **130**(12): p. 3756-+.

32. Kang, X.W. and S.W. Chen, *Electronic conductivity of alkyne-capped ruthenium nanoparticles.* Nanoscale, 2012. **4**(14): p. 4183-4189.

33. Kang, X., et al., *Alkyne-functionalized ruthenium nanoparticles: ruthenium-vinylidene bonds at the metal-ligand interface.* J Am Chem Soc, 2012. **134**(3): p. 1412-1415.

34. Robin, M.B. and P. Day, *Mixed Valence Chemistry-A Survey and Classification*, in *Advances in Inorganic Chemistry and Radiochemistry*, H.J. Emeléus and A.G. Sharpe, Editors. 1968, Academic Press. p. 247-422.

35. Ding, F.Z., et al., *Computational Study of Bridge-Assisted Intervalence Electron Transfer.* Journal of Physical Chemistry A, 2010. **114**(19): p. 6039-6046.

36. Pradhan, S., et al., *Photo-gated charge transfer of organized assemblies of CdSe quantum dots.* Langmuir, 2006. **22**(2): p. 787-793.

Chapter 5

Self-Assembly and Chemical Reactivity of Alkenes on Platinum Nanoparticles

5.1 Abstract

Stable platinum nanoparticles were synthesized by the self-assembly of alkene derivatives onto the platinum surface, possibly forming platinum−vinylidene (Pt=C=CH−)/platinum−acetylide (Pt−C≡C) interfacial bonds as a result of dehydrogenation and transformation of the olefin moieties catalyzed by platinum. Transmission electron microscopic measurements showed that the nanoparticles were well-dispersed without apparent agglomeration, indicating effective passivation of the nanoparticles by the ligands, and the average core was estimated to be 1.34 ± 0.39 nm. FTIR measurements showed the emergence of a new vibrational band at 2023 cm^{-1}, which was ascribed to the formation of =C=C/C≡C from the dehydrogenation of alkene ligands on platinum surfaces. Consistent behaviors were observed in photoluminescence measurements, where the emission profiles were similar to those of alkyne-functionalized Pt nanoparticles that arose from intraparticle charge delocalization between the particle-bound acetylene moieties. Selective reactivity with imine derivatives further confirmed the formation of Pt=C=CH−/Pt−C≡C interfacial linkages, as manifested in NMR and electrochemical measurements. Further structural insights were obtained by X-ray absorption near-edge spectroscopy and extended X-ray absorption fine structure analysis, where the coordinate numbers and bond lengths of the Pt−Pt and Pt−C linkages suggested that the metal−ligand interfacial bonds were in the intermediate between those of Pt−C≡ and Pt−Csp^2.

5.2 Introduction

Organically capped transition-metal nanoparticles represent a unique class of functional nanomaterials whose material properties have been found to be readily manipulated by the chemical natures of both the metal cores and organic ligands. More recently, metal–ligand interfacial bonding interactions have also been recognized as a powerful and valuable tool in the regulation of the chemical and physical properties of metal nanoparticles, as highlighted by a series of studies in which nanoparticles are functionalized by (conjugated) metal–carbon (or nitrogen) covalent bonds, in contrast with those passivated by mercapto derivatives.[1-22] Several experimental strategies have been developed, for instance, by taking advantage of the self-assembly of diazo derivatives on freshly prepared metal surfaces forming metal–carbene π bonds (M=C), the formation of metal–acetylide (M–C≡)/metal–vinylidene (M=C=CH–) bonds with acetylene derivatives, as well as the formation of metal–nitrene (M=N) π bonds with nitrene derivatives produced by the thermolytic reduction of azides.[1-4, 6, 7, 9-12, 14-16, 18, 19] These interfacial bonds are presumed to involve pπ–dπ bonding interactions between the unsaturated ligands and the metal centers,[23] akin to those observed in conventional organometallic complexes.[24, 25] In these nanoparticles with conjugated bonds at the metal–ligand interface, extensive intraparticle charge delocalization occurs between particle-bound functional moieties, leading to the emergence of electronic and optical properties that are analogous to those of their dimeric forms. Such unprecedented material properties have been exploited for the sensitive and selective detection of various compounds and ions through deliberate engineering of the nanoparticle surface.[14, 16, 26, 27]

With these earlier successes, one immediate question arises: is it possible to functionalize nanoparticles with alkene derivatives? Note that alkene molecules are known to adsorb on transition−metal surfaces, undergoing interfacial structural transformation (isomerization) through dehydrogenation.[23, 28] For example, the interaction of ethylene (CH_2=CH_2) with Pt has been extensively studied as a model system in the investigation of the alkene hydrogenation−dehydrogenation process.[28-30] At low temperatures (< 50 K), ethylene adsorbs onto platinum with the C=C bond parallel to the Pt surface, maintaining largely sp^2 character. However, at higher temperatures, several new and more stable species are generated by structural transformations.[31] For instance, at temperatures above 90 K, rehybridization of the π bond may be induced by electron transfer from Pt into the π* orbital, followed by the formation of a di-σ bound species on the Pt surface.[30] At higher temperatures, new surface species such as vinyl, vinylidene (~140 K), and ethylidyne (~300 K) may be generated as a result of the dehydrogenation reactions.[30, 32] Note that these aforementioned species can coexist on the platinum surface; however, the coverage of each varies with temperature.

Propylene (CH_3CH=CH_2) is another small alkene molecule that has attracted extensive interest. For instance, in the study of the interfacial interactions of propylene with platinum using reflection−absorption infrared spectroscopic (RAIRS) techniques, it has been proposed that at least four species might be derived from adsorbed propylene depending on surface coverage and temperature.[33] At temperatures below 230 K, undissociated propylene molecules adsorb on the platinum surface like ethylene,

yet at temperatures up to 275 K, it is shown that propylidyne (CH3CH2C≡), an alkylidyne moiety, is formed resulting from the dehydrogenation and rearrangement of the di-σ species, and the details of such conversion are believed to involve a stable and identifiable intermediate (2-propyl, CH3CH(Pt)CH3) or propylidene (Pt=CHCH2CH3).[33] At room temperature, there is evidence showing that propylene exhibits a structure similar to that of ethylene.[34]

For longer alkenes, it has also been proposed that they may decompose through the corresponding alkylidyne intermediates as they adsorb onto the surface of transition-metal surfaces.[34] This is the primary motivation of the present study. Herein we describe the synthesis and characterization of alkene-functionalized platinum nanoparticles. "Bare" Pt colloids were synthesized by thermolytic reduction of Pt(II) in 1,2-propanediol at controlled temperatures. Alkene derivatives were then added to the solution for nanoparticle surface functionalization. The resulting nanoparticles were found to be readily soluble in apolar organic solvents and exhibited apparent photoluminescence emission, suggesting the formation of conjugated metal–ligand interfacial bonds most probably through dehydrogenation reactions of the alkene ligands, a behavior analogous to those of nanoparticles functionalized by acetylene derivatives.[2, 3, 7, 26] The structures of the resulting nanoparticle were characterized by a range of experimental tools including transmission electron microscopy, infrared, photoluminescence, NMR spectroscopy, and electrochemistry. Further structural insights were obtained in X-ray absorption measurements, wherein X-ray absorption near edge spectroscopy (XANES) and extended X-ray absorption fine

structure (EXAFS) analyses were carried out to probe the interfacial bonding interactions by using platinum nanoparticles stabilized by trifluoromethylphenyl fragments (PtTFPB, dia. 2.20 nm),[35] dodecyne-stabilized platinum (PtHC12, dia. 1.34 nm) nanoparticles,[3] and a Pt foil as the controls.

5.3 Experimental section

Chemicals. Platinum chloride ($PtCl_2$, 99+%, ACROS), 1-octadecene (ODE, 98%, ACROS), 1-dodecyne (HC12, 98%, Sigma-Aldrich), 1,2-propanediol (ACROS), sodium acetate trihydrate ($NaOAc{\cdot}3H_2O$, MC&B), and potassium trichloro(ethylene)platinate(II) hydrate (Zeise's salt, $K[Cl_3Pt(C_2H_4)]$, Sigma-Aldrich) were all used as received. The synthesis and characterization of [[(1-methylethyl)imino]methyl]ferrocene (Fc-imine) have been described previously.[2] All solvents were obtained from typical commercial sources and used without further treatment. Water was supplied by a Barnstead Nanopure water system (18.3 MΩ·cm).

Synthesis of Platinum Nanoparticles. Platinum nanoparticles capped by alkene derivatives were prepared by adopting a procedure that was used previously.[36] In brief, 0.1 mmol of $PtCl_2$ was dissolved in 3 mL of concentrated hydrochloric acid (12.1 M); then, the prepared solution was condensed to 1 mL, neutralized with sodium carbonate, and centrifuged to remove undissolved salts. The supernatant and 1 mmol of NaOAc were added to 100 mL of 1,2-propanediol. The mixed solution was heated to 165 °C under vigorous stirring and kept for 1 h. After the colloid solution was cooled to room temperature, 0.3 mmol of 1-octadecene (at a three-fold molar excess of $PtCl_2$) dissolved in 50 mL of toluene was added, and the mixed solution was stirred

magnetically for 7 days. The toluene phase was then collected, dried with rotary evaporation, and rinsed extensively with a copious amount of acetonitrile to remove excessive ligands. The resulting nanoparticles were denoted as PtODE.

Platinum nanoparticles capped by 1-dodecyne (PtHC12) were prepared in a similar fashion except that 1-dodecyne was used instead for nanoparticle surface functionalization and extraction.[3]

The synthesis of platinum nanoparticles stabilized by trifluoromethylphenyl fragments (PtTFPB, dia. 2.20 nm) has been detailed previously by the coreduction of H_2PtCl_4 and trifluoromethylphenyl diazonium salts.[35] In brief, the diazonium salts were synthesized from para-trifluoromethylphenyl aniline (0.5 mmol), sodium nitrite (0.52 mmol), and 35% perchloric acid (0.45 mL) in an ice-water bath. The resulting diazonium salt and H_2PtCl_4 (0.1 mmol) were codissolved in a mixed solvent of H_2O−THF (1:1 V/V) into which a freshly prepared $NaBH_4$ solution (0.2 M, 5 mL) was added slowly under magnetic stirring, leading to the formation of a dark brown solution that signified the production of aryl-stabilized Pt nanoparticles.[17, 37]

Reactivity of Platinum Nanoparticles. The reactivity of the PtODE nanoparticles prepared above was tested with Fc-imine.[2] Experimentally, 4 mg of PtODE nanoparticles and 12 mg of Fc-imine were codissolved into 2 mL of dry CH_2Cl_2 under vigorous stirring for 7 days. Upon the completion of the reaction, the solution was dried by rotary evaporation and rinsed with acetonitrile for several times to remove excessive free ligands.

Characterization. The morphology and size of the Pt nanoparticles were characterized by transmission electron microscopy studies (TEM, Philips CM300 at 300 kV). ^{1}H NMR spectroscopic measurements were carried out with a Varian Unity Inova 600 MHz NMR spectrometer. UV-vis spectroscopic studies were performed with an ATI Unicam UV4 spectrometer using a 1 cm quartz cuvette with a resolution of 1 nm. Photoluminescence characteristics were examined with a PTI fluorospectrometer. FTIR measurements were carried out with a PerkinElmer FTIR spectrometer (Spectrum One, spectral resolution 4 cm^{-1}), where the samples were prepared by casting the particle solutions onto a ZnSe disk.

X-ray absorption spectroscopic (XAS) studies were performed using the PNC-CAT bending magnet beamline (Sector 20) of the Advanced Photon Source at Argonne National Laboratory, IL. A Si(111) double-crystal monochromator with Rh-coated focusing mirrors was employed for wavelength selection; the incident beam was further detuned to 80% of maximum flux to reject higher harmonics. Data were acquired in fluorescence mode using a liquid-nitrogen-cooled, 32-element Ge detector, with a Pt foil and gas ionization chambers used for in-line energy calibration. To enhance EXAFS signal intensity, measurements were performed at controlled temperatures. Data processing and EXAFS fitting were performed using WinXAS software,[38] and the amplitude and phase scattering factors used in the fits were obtained from model structures using FEFF8.[39] To fit the k^3-weighted EXAFS spectra, a two-stage process was implemented. In the first stage, the energy shift (ΔE_0) and Debye–Waller coefficient (σ^2) values of all scattering paths were correlated to obtain a reasonable

starting value for the coordination number (CN) of the Pt–C path. In the second stage, this CN was fixed while allowing the σ^2 values to vary independently, and a single ΔE_0 value was again used to obtain the final fit. Uncertainty in parameter values was determined by weighting the corresponding off-diagonal matrix elements by the reduced χ^2 value of the fit while also taking into consideration shot noise in the Fourier-transformed EXAFS spectrum (15–25 Å).[40]

Electrochemistry. Voltammetric measurements were carried out with a CHI 440 electrochemical workstation. A polycrystalline gold disk electrode (sealed in glass tubing) was used as the working electrode. A Ag/AgCl wire and a Pt coil were used as the reference and counter electrodes, respectively. The gold electrode was first polished with alumina slurries of 0.5 μm and then cleaned by sonication in 0.1 M HNO_3, H_2SO_4, and Nanopure water successively. Prior to data collection, the electrolyte solution was deaerated by bubbling ultrahigh-purity N_2 for at least 20 min and blanketed with a nitrogen atmosphere during the entire experimental procedure.

5.4 Results and Discussion

Figure 5.1 depicts a representative TEM micrograph of the PtODE nanoparticles. It can be seen that the nanoparticles are well-separated without apparent aggregation, suggesting sufficient protection of the nanoparticles by the capping ligands, and the majority of the nanoparticles are within the narrow range of 1 to 2 nm in diameter, with the average core diameter of 1.34 ± 0.39 nm, as depicted in the right inset. Additionally, from high-resolution imaging in the left inset, one can see that the

nanoparticles exhibit clearly defined lattice fringes and the interlayer spacing of 0.23 nm is consistent with the (111) crystal planes of fcc platinum (PDF Card 4-802).

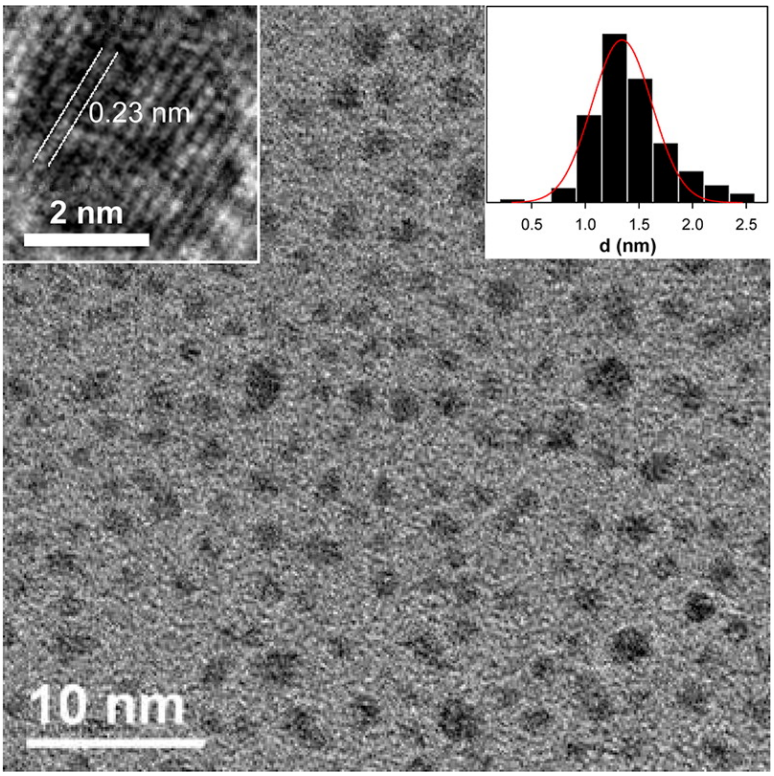

Figure 5.1. Representative TEM image of platinum colloids prepared by thermolytic reduction of $PtCl_2$ in 1,2-propanediol. Scale bar 10 nm. Upper left inset is a high-resolution TEM image where the lattice fringes of a nanoparticle can be seen at a spacing of 0.23 nm, corresponding to Pt(111) crystal planes. Scale bar 2 nm. Upper right inset shows the nanoparticle core size histogram. Red curve is the Gaussian fit.

The formation of Pt nanoparticles was also manifested in UV-vis absorption measurements, as shown in the inset to Figure 5.2. The largely featureless exponential decay profile is in good agreement with the Mie scattering of nanosized Pt colloids.[41] Interestingly, the resulting PtODE nanoparticles exhibit apparent photoluminescence.

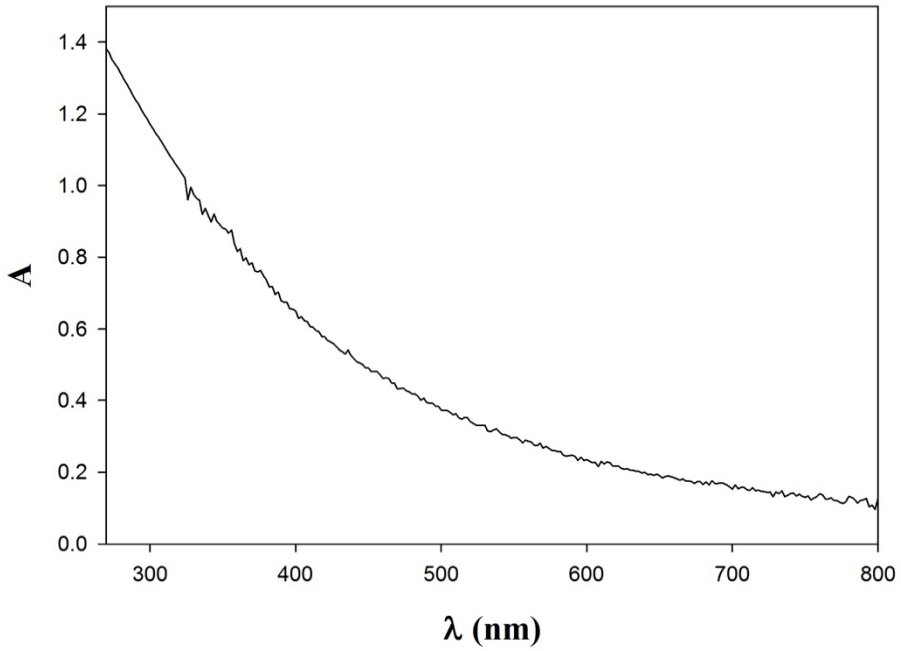

Figure 5.2. UV-vis absorption spectrum of PtODE nanoparticles in CH_2Cl_2.

Figure 5.3 shows the excitation and emission spectra of the PtODE nanoparticles, with a clearly defined excitation peak (λ_{ex}) at 360 nm and an emission peak (λ_{em}) at 452 nm. Note that in a previous study with alkyne-functionalized Pt nanoparticles (such as 1-dodecyne-capped Pt nanoparticles, PtHC12),[3] similar photoluminescence features were observed at λ_{ex} = 352 nm and λ_{em} = 430 nm, which was accounted for by the formation of Pt–acetylide (Pt–C≡C)/Pt–vinylidene (Pt=C=C) interfacial bonds such that the particle-bound acetylene moieties behaved analogously to diacetylene derivatives (C≡C–C≡C). In the present study, the fact that the resulting nanoparticles exhibit apparent photoluminescence suggests that a similar interfacial linkage was

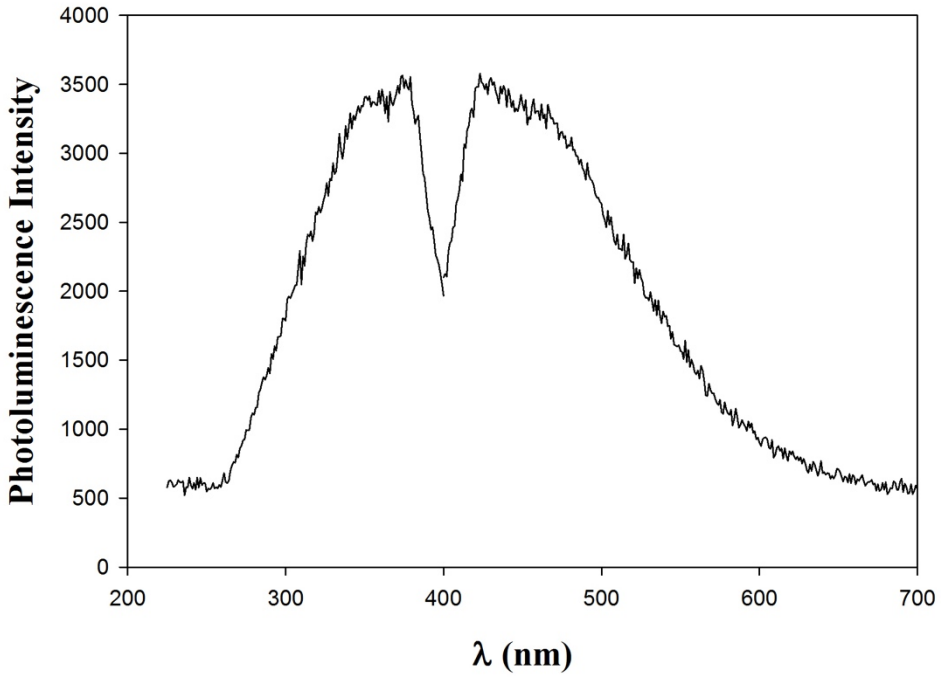

Figure 5.3. Photoluminescence spectrum of PtODE nanoparticles in CH_2Cl_2.

formed, possibly as a result of dehydrogenation of the alkene ligands on the nanoparticle surface. That is, it is likely that the eventual nanoparticle-bound ligands involved either vinylidene or alkynyl species in which the conjugated interfacial bonds led to intraparticle charge delocalization and hence photoluminescence, as observed previously with alkyne-capped nanoparticles.[23, 28, 34] Note that the formation of vinylidene species has indeed been confirmed for ethylene molecules absorbed on single-crystal Pt surfaces.[32-34] Such a hypothesis is also supported by a control experiment with Zeise's salt, $K[PtCl_3(C_2H_4)]$, where an olefin is coordinated to the Pt(II) metal center in an η^2 configuration by $d\pi$–$p\pi$ interactions.[42, 43] The fact that no

photoluminescence was observed with Zeise's salt indicates that no such structure was formed at the metal–ligand interface in PtODE nanoparticles.

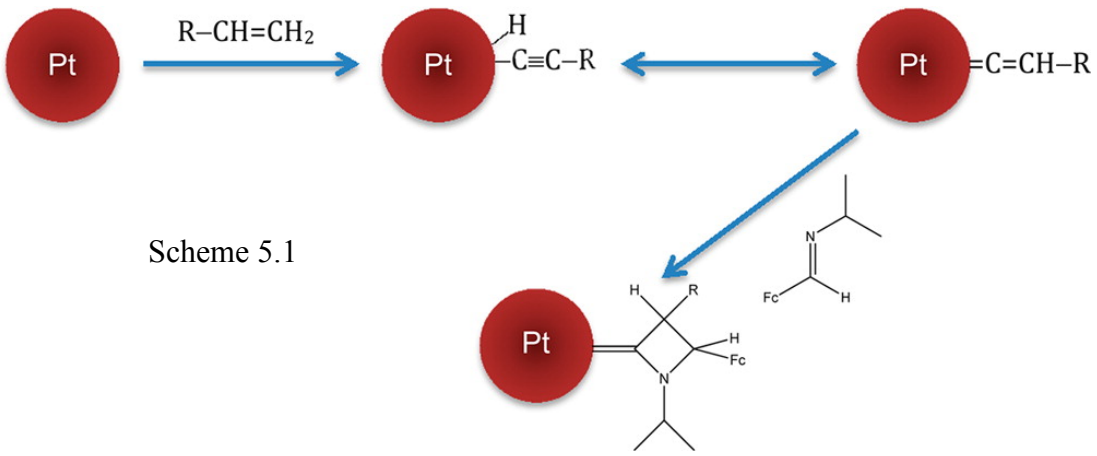

Scheme 5.1

The structures of the PtODE nanoparticles were further examined by FTIR measurements. Figure 5.4 depicts the FTIR spectra of monomeric ODE ligands and PtODE nanoparticles. For monomeric ODE (green curve), several characteristic bands can be identified at 3077 cm^{-1} for the =C–H stretch, 1641 cm^{-1} for the C=C stretch, and 995 and 910 cm^{-1} for the out-of-plane =C–H bends (with an overtone of the 910 cm^{-1} absorption at 1817 cm^{-1}).[44] In contrast, the stretching and bending vibrations of the terminal =C–H groups vanished with the PtODE nanoparticles (black curve; the broad band centered 3500 cm^{-1} most likely arose from residual water), signifying drastic structural transformations of the ODE ligands when bound onto the Pt nanoparticles. Note that in Zeise's salt, the C=C stretching vibration is typically found at 1526 cm^{-1}. [45] The absence of such a feature with the PtODE nanoparticles also

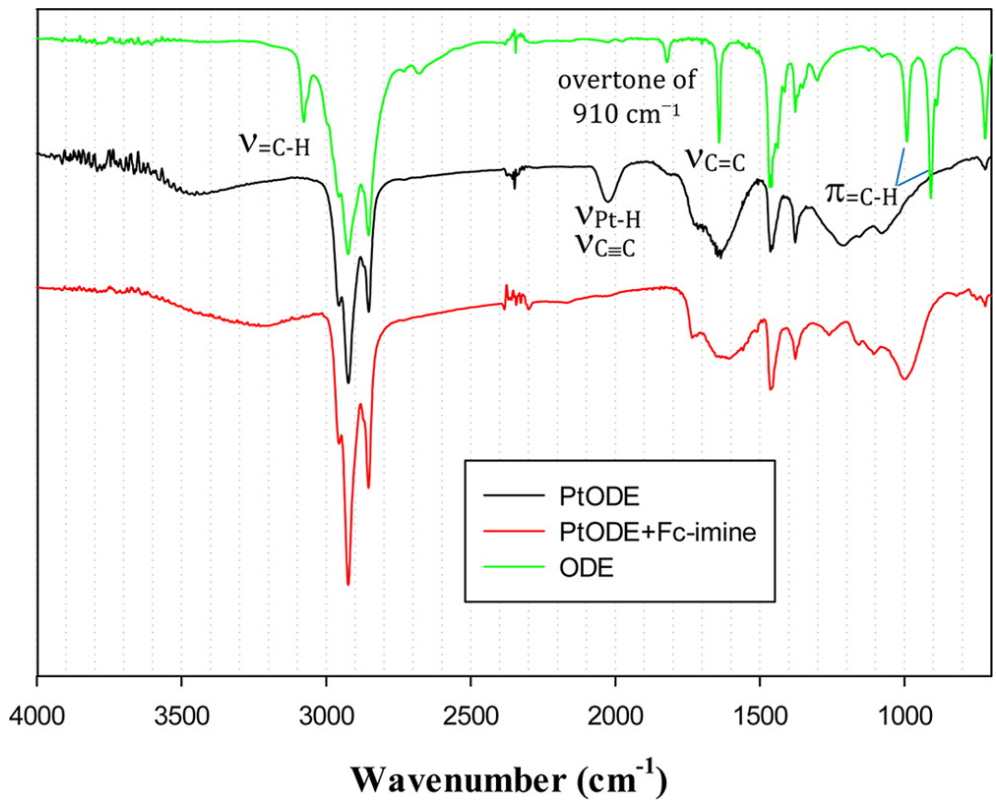

Figure 5.4. FTIR spectra of PtODE nanoparticles (black curve) and monomeric ODE (green curve). The spectrum of the PtODE nanoparticles after reacting with Fc-imine is also shown as the red curve.

suggests that it is unlikely that the ODE ligands were bound onto the Pt nanoparticle surface in the η^2 configuration. Concurrently, a new broad peak emerged at ~2023 cm^{-1} that has been previously observed with alkyne-functionalized Pt nanoparticles and ascribed to the combined contributions from nanoparticle-bound C≡C stretching[1-3, 7] and =C=C vibrations. This suggests that the ODE ligands, at least in part, underwent dehydrogenation reactions on the Pt surface to form acetylide/vinylidene derivatives and, hence, Pt–acetylide/Pt–vinylidene (Pt–C≡C/Pt=C=C) bonds, as depicted in Scheme 5.1. Note that the dehydrogenation reactions of alkenes on platinum surfaces

are rather complex, involving a range of reaction species.[17, 33, 35, 37] Therefore, the formation of other dehydrogeneration products at the interface, which are likely spectroscopically silent within the present experimental context, cannot be excluded.

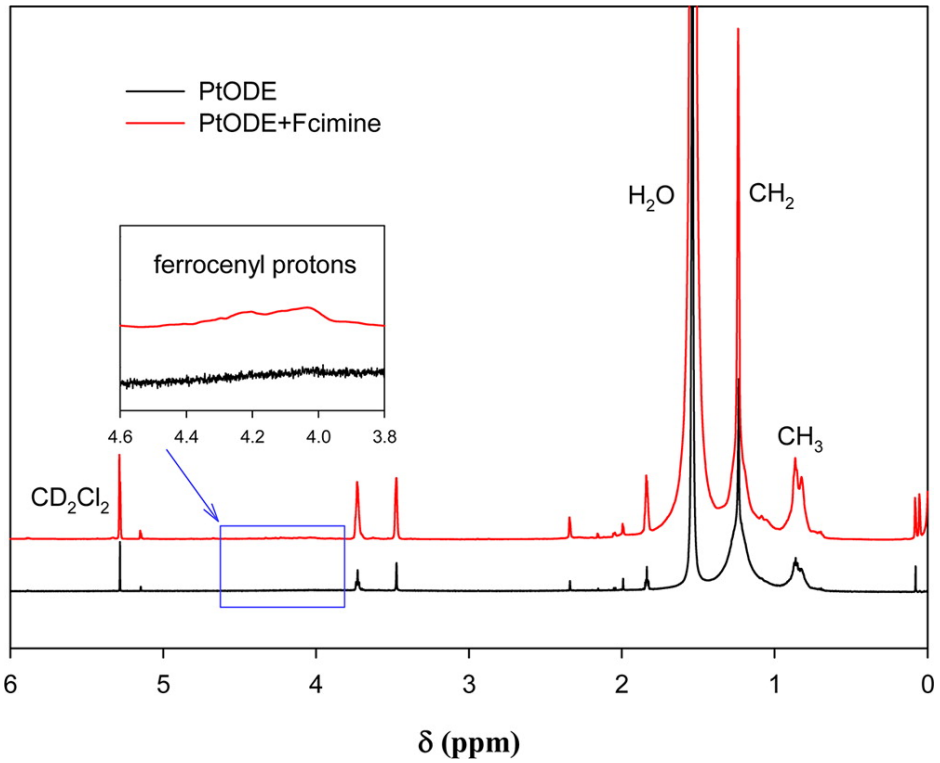

Figure 5.5. ^{1}H NMR spectra of PtODE nanoparticles before and after reactions with Fc-imine in CD_2Cl_2. Inset is an enlarged view of the section between 3.8 and 4.6 ppm.

Such a structural model is further confirmed by the selective reactivity of the PtODE nanoparticles with imine derivatives. As previously demonstrated with alkyne-functionalized ruthenium nanoparticles,[2] the metal–acetylide interfacial bonds may be involved in a dynamic equilibrium with metal–vinylidene linkages through a tautomeric rearrangement process, which has been known to react selectively with imine derivatives to form a heterocyclic azetidinylidene complex (Scheme 5.1).[1, 46]

We used a ferrocene-imine (Fc-imine) derivative as the illustrating example where the redox-active ferrocenyl moiety might be exploited as a molecular probe. Figure 5.5 shows the ^{1}H NMR spectra of the PtODE nanoparticles before and after reaction with Fc-imine. It can be seen that for the as-prepared PtODE nanoparticles (black curve), a prominent broad peak appears at ~0.9 ppm, which can be assigned to the terminal methyl (CH_3) protons of the ODE ligands, and (part of) the methylene (CH_2) protons can be identified by the peak centered at 1.2 ppm. The peak centered at 1.5 ppm can be assigned to protons of residual H_2O in the sample, and the three tiny peak around 1.8, 3.5, and 3.7 ppm can be ascribed to protons from residual acetonitrile, methanol, and ethanol, respectively; however, no olefin protons can be seen, which are anticipated to appear at about 4.9 and 5.8 ppm.[47] These observations indicate that the nanoparticles were spectroscopically clean and free of any excess ligands, and, importantly, that the olefin moieties are indeed the anchoring groups that bind to the nanoparticle surface. This most probably occurs via their platinum-catalyzed dehydrogenation into acetylene derivatives, where the close proximity to the nanoparticle core surface causes the signals of relevant protons to be broadened into the baseline.[11, 12, 27, 48] A very consistent spectral profile was observed for the PtODE nanoparticles after reactions with Fc-imine (red curve), except that an additional broad peak emerged within the range of 3.9 to 4.3 ppm, as illustrated in the Figure 5.5 inset, which is consistent with the ferrocenyl ring protons; and based on the integrated peak areas of the ferrocenyl and methyl protons, the ferrocene surface concentration was estimated to be 4.3%.[1, 46] Again, the absence of any sharp NMR feature indicates that the ferrocenyl moieties

were indeed incorporated onto the nanoparticle surface, most likely by the imido transfer reactions (Scheme 5.1), with no contributions from ferrocenyl monomers.[2] This behavior may be accounted for by the self-assembly of the ODE ligands onto the Pt nanoparticle surface, which then underwent dehydrogenation reactions to form Pt–acetylide interfacial bonds, thus causing the nanoparticles to behave analogously to those functionalized by acetylene derivatives.[2]

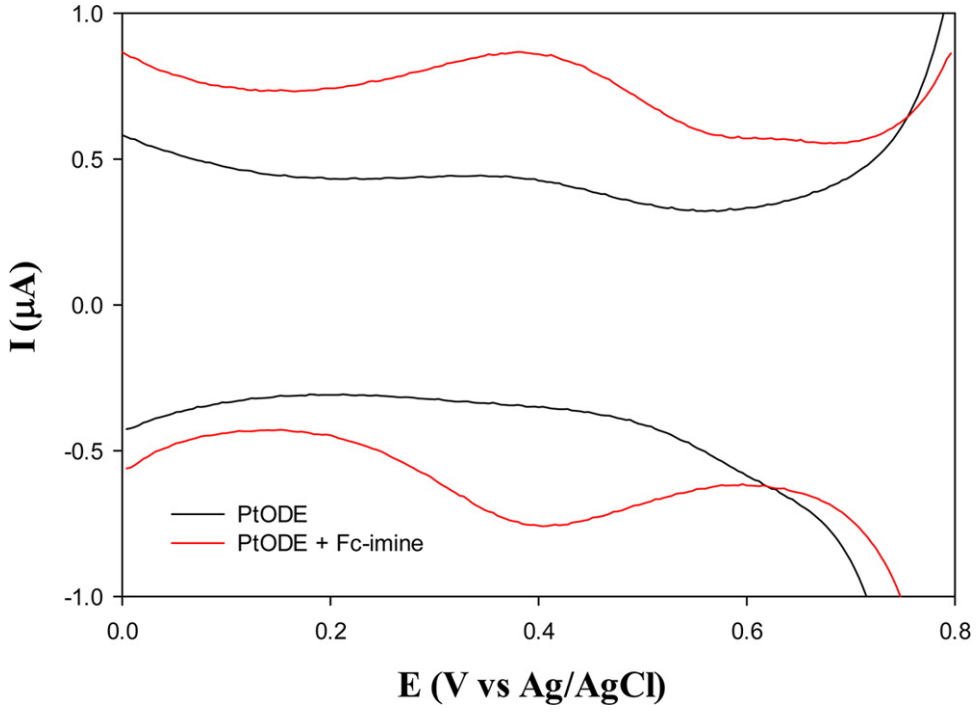

Figure 5.6. SWVs of PtODE (black curve) before and (red curve) after reactions with Fc-imine in DMF with 0.1 M TBAP. Nanoparticle concentration 2 mg/mL, gold electrode surface area 1.57 mm^2, DC ramp 4 mV/s, and pulse amplitude 25 mV.

The unique reactivity of PtODE nanoparticles with Fc-imine was also manifested in FTIR measurements. From Figure 5.4, one can see that after the reaction of PtODE nanoparticles with Fc-imine (red curve) the vibration band at 2030 cm^{-1}

vanished as a result of imido transfer at the metal–ligand interface where the platinum–acetylide/platinum–vinylidene (Pt–C≡C/Pt=C=C) bonds disappeared (Scheme 5.1). The successful incorporation of the ferrocenyl moieties onto the PtODE nanoparticle surface was further evidenced by electrochemical measurements in DMF with 0.10 M tetrabutylammonium perchlorate (TBAP) as the supporting electrolyte. Figure 5.6 shows the square-wave voltammograms (SWVs) of PtODE nanoparticles (black curve) before and (red curve) after reactions with Fc-imine. In contrast with the featureless voltammetric responses of the as-prepared PtODE nanoparticles, a pair of well-defined voltammetric peaks can be seen with a formal potential of +0.39 V (vs Ag/AgCl) for the PtODE nanoparticles after reaction with Fc-imine. This can be ascribed to the redox reactions of the ferrocenyl moieties incorporated onto the PtODE nanoparticle surface ($Fc^+ + e^- \leftrightarrow Fc$). The relatively large peak splitting ($\Delta E_p \approx 20$ mV) may be ascribed to the surrounding of the ferrocenyl moieties by the long aliphatic hydrophobic ligands, as the energetically unfavorable environment would render it difficult for counterions to reach the resulting ferrocenium ions and hence impede the electron-transfer kinetics.[49]

X-ray absorption spectroscopy was then employed to probe the local atomic structure and interfacial Pt-ligand bonding of the PtODE nanoparticles. Figure 5.7a depicts the X-ray absorption near-edge spectrum (XANES) at the Pt L_3 absorption edge of the PtODE nanoparticles, along with those of PtTFPB (dia. 2.20 nm)[35] and PtHC12 (dia. 1.34 nm) nanoparticles,[3] and a Pt foil. There are several aspects that warrant attention here. First, it can be seen that the Pt L_3 absorption edges of the three

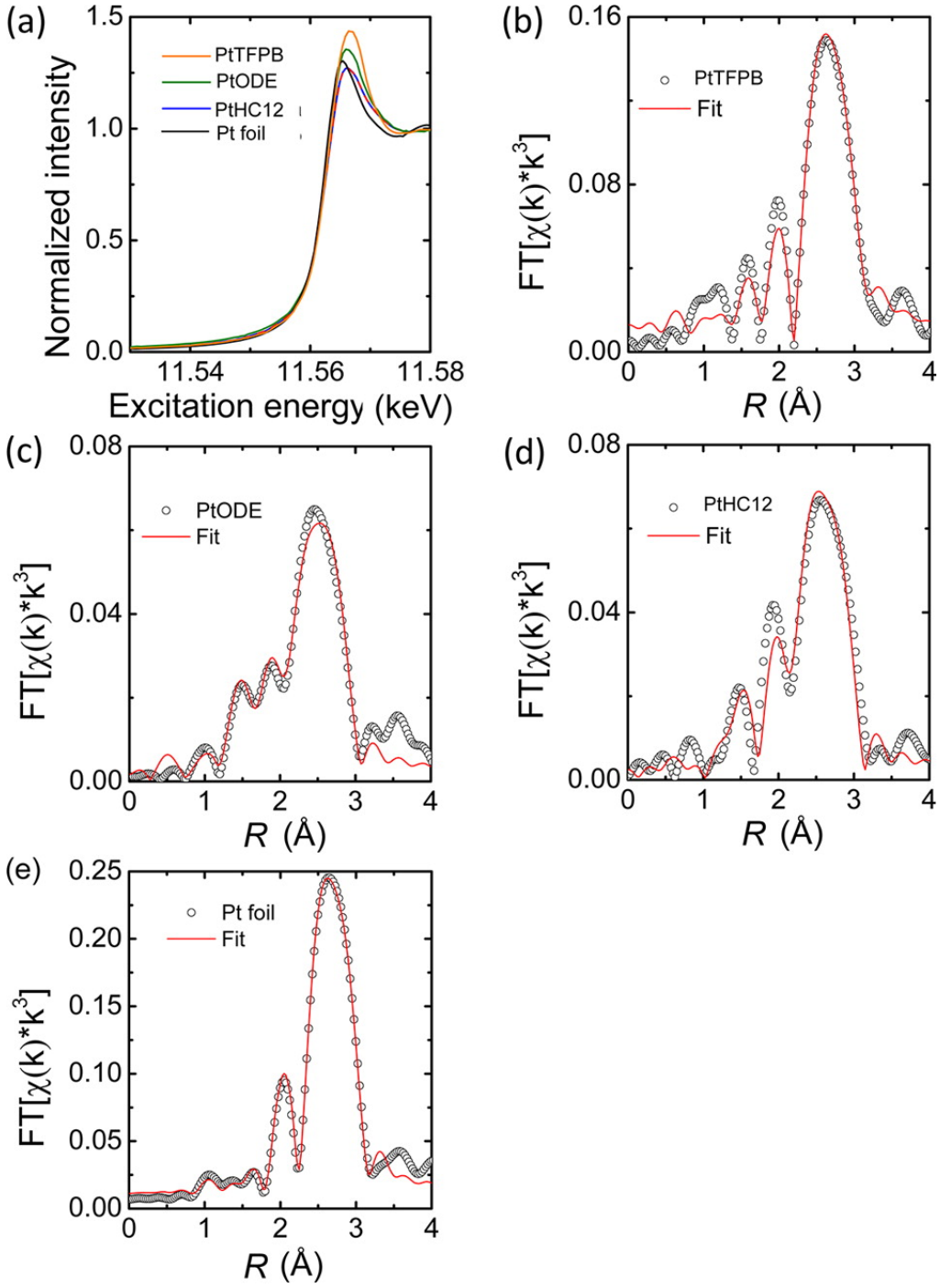

Figure 5.7. (a) XANES and (b–e) Fourier-transformed EXAFS spectra of PtTFPB, PtODE, and PtHC12 nanoparticles and a Pt foil reference acquired at the Pt L_3 absorption edge. Symbols are experimental data and red curves are the corresponding fits.

nanoparticles were all apparently shifted to a higher binding energy than that of the Pt foil: PtTFPB (11.566 keV) > PtODE ≈ PtHC12 (11.565 keV) > Pt foil (10.564 keV). Similar behaviors have also been observed in XPS measurements, wherein a blue shift of the binding energy is typically observed of the core and valence electrons for transition-metal nanoparticles relative to those of their bulk counterparts. This is largely accounted for by the interplay between the effects of quantum confinement (nanoparticle size) and reduction of surface coordination.[50] It is interesting to note that whereas the PtODE and PtHC12 nanoparticles are smaller than PtTFPB, the more positively shifted Pt L_3 absorption edge of the latter is likely due to the strong electron-withdrawing trifluoromethyl (CF_3) moieties.

Second, the intense XANES peak following the absorption edge (the white line) arises from occupied Pt 2p to unoccupied 5d electronic transition, and a more intense white line corresponds to a lower d-electron density.[51, 52] From Figure 5.7a, the white line peak intensity and breadth can be seen to increase in the order of PtHC12 < Pt foil < PtODE < PtTFPB, suggesting a progressive decrease in the Pt d-electron density.[51] Note that extensive intraparticle charge delocalization occurs in PtHC12 nanoparticles between the particle-bound C≡C/=C=C moieties, with the metal cores as the conducting media.[3] Spectroscopic studies suggest a marked diminishment of the acetylene bonding order, wherein the conjugated metal–ligand interfacial bonds likely involve partial filling of the empty Pt d orbitals by ligand π electrons, leading to a decrease in the white line intensity as compared with that of bulk Pt. In contrast, the number of unoccupied Pt d states in the PtTFPB nanoparticles was likely enhanced by

the strong electron-withdrawing trifluoromethyl moieties, such that the corresponding white line peak intensity was the highest among the series. The fact that the PtODE nanoparticles fell in the intermediate range signifies that the interfacial bonding order was most likely in between that of PtHC12 (Pt−C≡C/Pt=C=C) and PtTFPB (Pt−Csp^2), implying that indeed various dehydrogenation products were formed when the alkene ligands were bound onto the Pt nanoparticle surface in PtODE (Scheme 5.1).[30, 32-34]

In addition to the electronic information gleaned from XANES analysis, significant structural information may also be obtained by examining the extended X-ray absorption fine structure (EXAFS) data. Fitting of the Fourier-transformed EXAFS spectra in panels b−e was then carried out to extract parameters pertinent to the local structure of the samples, with the corresponding parameter values summarized in Table 5.1. It can be seen that in comparison with bulk Pt (Pt foil) where the Pt−Pt coordination number (CN) is 12, the CN values are much lower for the nanoparticle samples, lying only in the narrow range of 5 to 6. Such low CNs are often observed in nanoparticles due to their relatively large number of low-coordinate surface atoms and are reflective of their nanoscale dimensions.[52] Consistent behaviors were also observed in the estimation of the Pt−Pt bond length, which was 2.75 Å for PtTFPB, 2.69 Å for PtODE, and 2.72 Å for PtHC12, all slightly smaller than that of bulk Pt (2.77 Å). This may be accounted for by lattice contraction of nanosized particles.[50]

Furthermore, it can be seen from Table 1 that the average Pt−C CN of PtODE nanoparticles is 0.9, which is close to that of the PtTFPB and PtHC12 nanoparticles

(0.8). Note that based on a truncated octahedral core structure and the average nanoparticle core diameter the fraction of surface atoms might be estimated to be 87.3% for PtODE and PtHC12 and 57.2% for PtTFPB.[48] This signifies that the number of ligands bound to each surface Pt atom is ~1.03 for PtODE, 0.92 for PtHC12, and 1.53 for PtTFPB nanoparticles. That is, the nanoparticles were all capped densely by the respective organic capping ligands. In fact, TEM measurements (Figure 5.1) showed good dispersion of the nanoparticles without apparent agglomeration, signifying effective passivation of the nanoparticles by the organic capping ligands.

Table 5.1. Structural Parameters Obtained from Fitting of the Pt L_3-Edge Fourier-Transformed EXAFS Spectra

	PtTFPB		**PtODE**		**PtHC12**		**Pt foil**
bond	**Pt–C**	**Pt–Pt**	**Pt–C**	**Pt–Pt**	**Pt–C**	**Pt–Pt**	**Pt–Pt**
CN	0.8	5.2(8)	0.9	6.3(4)	0.8	6.0(1)	12
***R* (Å)**	2.05(5)	2.750(6)	2.01(1)	2.690(4)	1.91(3)	2.72(1)	2.767(2)
σ^2 (Å^2)	0.006(6)	0.0023(7)	0.003(2)	0.0081(4)	0.003(3)	0.007(1)	0.0043(2)
ΔE_0 (eV)	4(1)		-1(1)		2(3)		5.2(5)

Further structural insights can be obtained from analysis of the mean Pt–C bond length. As depicted in Table 5.1, the Pt–C bond length is determined to be 2.05 Å for PtTFPB nanoparticles that feature largely Pt–Csp^2 single bonds[35] and 1.91 Å for PtHC12 nanoparticles that are known to exhibit a Pt–C≡C/Pt=C=C interfacial bond.[3] Note that these are in very good agreement with results in a previous study of diplatinum complexes with C8 and C12 sp carbon chains where the Pt–C≡C bond length was estimated to be 1.99 Å and that of Pt–Csp^2 was estimated to be 2.06 Å.[53]

For PtODE nanoparticles the Pt–C bond length from EXAFS is 2.01 Å, which is in the intermediate between those of PtTFPB and PtHC12, suggesting that the bonding order is between those of Pt–C≡C/Pt=C=C and Pt–Csp^2. Again, this is likely due to the formation of various interfacial structures of the ODE ligands on the Pt surfaces (e.g., alkenes, alkylidenes, alkylidynes, etc.), some of which were spectroscopically silent within the present experimental context.[33, 34] Finally, one may notice that when ethylene is adsorbed on Pt(111) surfaces forming di-σ interfacial bonds, the Pt–C bond length is estimated to be at least 2.21 Å, markedly larger than those observed here with the three nanoparticles.[54]

5.5 Conclusions

Stable platinum nanoparticles were successfully prepared by the functionalization of alkene derivatives. Spectroscopic measurements suggested that at least part of the alkene ligands underwent dehydrogenation reactions on the platinum nanoparticle surface forming Pt–C≡C/Pt=C=C interfacial bonds, a structure that was identified when alkynes were self-assembled onto the nanoparticle surface. Further structural insights were obtained from X-ray absorption measurements, which indicated that the effective metal–ligand interfacial bonds were most likely in the intermediate between those of Pt–C≡C/Pt=C=C and Pt–Csp^2. Results from this study further enhance the "tool box" for nanoparticle surface functionalization, where increasingly complicated manipulation of their structures and properties may be achieved.

5.6 References

1. Chen, W., et al., *Alkyne-Protected Ruthenium Nanoparticles.* Journal of Physical Chemistry C, 2010. **114**(42): p. 18146-18152.

2. Kang, X., et al., *Alkyne-functionalized ruthenium nanoparticles: ruthenium-vinylidene bonds at the metal-ligand interface.* J Am Chem Soc, 2012. **134**(3): p. 1412-1415.

3. Liu, K., et al., *Platinum nanoparticles functionalized with acetylene derivatives: Electronic conductivity and electrocatalytic activity in oxygen reduction.* Journal of Electroanalytical Chemistry, 2013. **688**: p. 143-150.

4. Kang, X.W., Y. Song, and S.W. Chen, *Nitrene-functionalized ruthenium nanoparticles.* Journal of Materials Chemistry, 2012. **22**(36): p. 19250-19257.

5. Zhang, S., K.L. Chandra, and C.B. Gorman, *Self-assembled monolayers of terminal alkynes on gold.* Journal of the American Chemical Society, 2007. **129**(16): p. 4876-+.

6. Kang, X.W., et al., *Alkyne-Stabilized Ruthenium Nanoparticles: Manipulation of Intraparticle Charge Delocalization by Nanoparticle Charge States.* Angewandte Chemie-International Edition, 2010. **49**(49): p. 9496-9499.

7. Kang, X.W. and S.W. Chen, *Electronic conductivity of alkyne-capped ruthenium nanoparticles.* Nanoscale, 2012. **4**(14): p. 4183-4189.

8. Maity, P., et al., *Binding Motif of Terminal Alkynes on Gold Clusters.* Journal of the American Chemical Society, 2013. **135**(25): p. 9450-9457.

9. Deming, C.P., et al., *Alkyne-Protected AuPd Alloy Nanoparticles for Electrocatalytic Reduction of Oxygen.* Chemelectrochem, 2015. **2**(11): p. 1719-1727.

10. Chen, W., et al., *Carbene-functionalized ruthenium nanoparticles.* Chemistry of Materials, 2006. **18**(22): p. 5253-5259.

11. Chen, W., et al., *Nanoparticle-mediated intervalence transfer.* Journal of the American Chemical Society, 2008. **130**(36): p. 12156-12162.

12. Chen, W., et al., *Pyrene-Functionalized Ruthenium Nanoparticles: Novel Fluorescence Characteristics from Intraparticle Extended Conjugation.* Journal of Physical Chemistry C, 2009. **113**(39): p. 16988-16995.

13. Vignolle, J. and T.D. Tilley, *N-Heterocyclic carbene-stabilized gold nanoparticles and their assembly into 3D superlattices.* Chemical Communications, 2009(46): p. 7230-7232.

14. Kang, X.W., et al., *Intraparticle Charge Delocalization of Carbene-Functionalized Ruthenium Nanoparticles Manipulated by Selective Ion Binding.* Langmuir, 2011. **27**(20): p. 12636-12641.

15. Chen, W., S. Pradhan, and S.W. Chen, *Photoluminescence and conductivity studies of anthracene-functionalized ruthenium nanoparticles.* Nanoscale, 2011. **3**(5): p. 2294-2300.

16. Kang, X.W., et al., *Manipulation of Intraparticle Charge Delocalization by Selective Complexation of Transition-Metal Ions with Histidine Moieties.* Analytical Chemistry, 2012. **84**(4): p. 2025-2030.

17. Mirkhalaf, F., J. Paprotny, and D.J. Schiffrin, *Synthesis of metal nanoparticles stabilized by metal-carbon bonds.* Journal of the American Chemical Society, 2006. **128**(23): p. 7400-7401.

18. Ghosh, D. and S.W. Chen, *Palladium nanoparticles passivated by metal-carbon covalent linkages.* Journal of Materials Chemistry, 2008. **18**(7): p. 755-762.

19. Ghosh, D. and S.W. Chen, *Solid-state electronic conductivity of ruthenium nanoparticles passivated by metal-carbon covalent bonds.* Chemical Physics Letters, 2008. **465**(1-3): p. 115-119.

20. Chen, W., et al., *Intervalence transfer of ferrocene moieties adsorbed on electrode surfaces by a conjugated linkage.* Chemical Physics Letters, 2009. **471**(4-6): p. 283-285.

21. Joo, S.-W. and K. Kim, *Adsorption of phenylacetylene on gold nanoparticle surfaces investigated by surface-enhanced Raman scattering.* Journal of Raman Spectroscopy, 2004. **35**(7): p. 549-554.

22. Maity, P., et al., *Organogold Clusters Protected by Phenylacetylene.* Journal of the American Chemical Society, 2011. **133**(50): p. 20123-20125.

23. Zaera, F., *An organometallic guide to the chemistry of hydrocarbon moieties on transition metal surfaces.* Chemical Reviews, 1995. **95**(8): p. 2651-2693.

24. Koestner, R.J., M.A. Vanhove, and G.A. Somorjal, *Molecular-Structure of Hydrocarbon Monolayers on Metal-Surfaces.* Journal of Physical Chemistry, 1983. **87**(2): p. 203-213.

25. Belluco, U., et al., *Platinum-alkynyl and -alkyne complexes: old systems with new chemical and physical perspectives.* Journal of Organometallic Chemistry, 2000. **600**(1-2): p. 37-55.

26. Hu, P.G., et al., *Platinum Nanoparticles Functionalized with Ethynylphenylboronic Acid Derivatives: Selective Manipulation of Nanoparticle Photoluminescence by Fluoride Ions.* Langmuir, 2014. **30**(18): p. 5224-5229.

27. Chen, W., et al., *Pyrene-Functionalized Ruthenium Nanoparticles as Effective Chemosensors for Nitroaromatic Derivatives.* Analytical Chemistry, 2010. **82**(2): p. 461-465.

28. Valcarcel, A., et al., *Theoretical study of dehydrogenation and isomerisation reactions of propylene on Pt(111).* Journal of Catalysis, 2006. **241**(1): p. 115-122.

29. Kubota, J., et al., *Reversibly adsorbed pi-bonded ethene on Pt(111) surfaces by infrared reflection absorption spectroscopy.* Langmuir, 1996. **12**(7): p. 1926-1927.

30. Lee, A.F. and K. Wilson, *Fast x-ray spectroscopy study of ethene on clean and SO4 precovered Pt{111}.* Journal of Vacuum Science & Technology A, 2003. **21**(3): p. 563-568.

31. Stair, P.C. and G.A. Somorjai, *Adsorption of Acetylene on (111) Crystal-Face of Platinum - Detection of 2 Chemically Different Adsorption States by Low-*

Energy Electron-Diffraction. Chemical Physics Letters, 1976. **41**(2): p. 391-393.

32. Aleksandrov, H.A., et al., *Ethylene conversion to ethylidyne on Pd(111) and Pt(111): A first-principles-based kinetic Monte Carlo study.* Journal of Catalysis, 2012. **285**(1): p. 187-195.

33. Zaera, F. and D. Chrysostomou, *Propylene on Pt(111) I. Characterization of surface species by infra-red spectroscopy.* Surface Science, 2000. **457**(1-2): p. 71-88.

34. Koestner, R.J., et al., *Evidence for the Formation of Stable Alkylidyne Structures from C-3 and C-4 Unsaturated-Hydrocarbons Adsorbed on the Pt(111) Single-Crystal Surface.* Surface Science, 1982. **116**(1): p. 85-103.

35. Zhou, Z.Y., et al., *Ligand-Mediated Electrocatalytic Activity of Pt Nanoparticles for Oxygen Reduction Reactions.* Journal of Physical Chemistry C, 2012. **116**(19): p. 10592-10598.

36. Liu, K., Y. Song, and S.W. Chen, *Electrocatalytic activities of alkyne-functionalized copper nanoparticles in oxygen reduction in alkaline media.* Journal of Power Sources, 2014. **268**: p. 469-475.

37. Delamar, M., et al., *Covalent Modification of Carbon Surfaces by Grafting of Functionalized Aryl Radicals Produced from Electrochemical Reduction of Diazonium Salts.* Journal of the American Chemical Society, 1992. **114**(14): p. 5883-5884.

38. Ressler, T., *WinXAS: a program for X-ray absorption spectroscopy data analysis under MS-Windows.* Journal of Synchrotron Radiation, 1998. **5**: p. 118-122.

39. Ankudinov, A.L., et al., *Real-space multiple-scattering calculation and interpretation of x-ray-absorption near-edge structure.* Physical Review B, 1998. **58**(12): p. 7565-7576.

40. Newville, M., B.I. Boyanov, and D.E. Sayers, *Estimation of uncertainties in XAFS data.* Journal of Synchrotron Radiation, 1999. **6**: p. 264-265.

41. Creighton, J.A. and D.G. Eadon, *Ultraviolet Visible Absorption-Spectra of the Colloidal Metallic Elements.* Journal of the Chemical Society-Faraday Transactions, 1991. **87**(24): p. 3881-3891.

42. Gerisch, M., et al., *Synthesis and characterization of platinum(II) complexes with terminal alkynes analogous to Zeise's salt - structure of [K(18-crown-6)][PtCl3(PhC CD)]center dot CH2Cl2.* Journal of Organometallic Chemistry, 1997. **548**(2): p. 247-253.

43. Ding, S.W. and C.A. McDowell, *Zeise's salt studied by high resolution solid state C-13 CPMAS and H-1 SPEDA NMR spectroscopy.* Chemical Physics Letters, 1997. **268**(1-2): p. 194-200.

44. Silverstein, R.M., G.C. Bassler, and T.C. Morrill, *Spectrometric Identification of Organic Compounds, 5th ed.* 1991, New York: Wiley.

45. Grogan, M.J. and K. Nakamoto, *Infrared Spectra and Normal Coordinate Analysis of Metal-Olefin Complexes .I. Zeises Salt Potassium Trichloro*

(Ethylene) Platinate (2) Monohydrate. Journal of the American Chemical Society, 1966. **88**(23): p. 5454-&.

46. Zayed, M.A. and H. Fischer, *Investigation of novel organometallics by thermal spectroscopic methods.* Journal of Thermal Analysis and Calorimetry, 2000. **61**(3): p. 897-908.

47. Spectral Database for Organic Compounds SDBS. http://sdbs.db.aist.go.jp/sdbs/cgi-bin/cre_index.cgi.

48. Hostetler, M.J., et al., *Alkanethiolate gold cluster molecules with core diameters from 1.5 to 5.2 nm: Core and monolayer properties as a function of core size.* Langmuir, 1998. **14**(1): p. 17-30.

49. Rowe, G.K. and S.E. Creager, *Interfacial Solvation and Double-Layer Effects on Redox Reactions in Organized Assemblies.* Journal of Physical Chemistry, 1994. **98**(21): p. 5500-5507.

50. Aruna, I., et al., *Size dependence of core and valence binding energies in Pd nanoparticles: Interplay of quantum confinement and coordination reduction.* Journal of Applied Physics, 2008. **104**(6).

51. Duchesne, P.N. and P. Zhang, *Local structure of fluorescent platinum nanoclusters.* Nanoscale, 2012. **4**(14): p. 4199-4205.

52. Duchesne, P.N., et al., *Local Structure, Electronic Behavior, and Electrocatalytic Reactivity of CO-Reduced Platinum-Iron Oxide Nanoparticles.* Journal of Physical Chemistry C, 2013. **117**(49): p. 26324-26333.

53. Peters, T.B., et al., *C-8 and C-12 sp carbon chains that span two platinum atoms: The first structurally characterized 1,3,5,7,9,11-hexayne.* Organometallics, 1999. **18**(17): p. 3261-3263.

54. Watson, G.W., et al., *Density functional theory calculations on the interaction of ethene with the {111} surface of platinum.* Journal of Physical Chemistry B, 2000. **104**(27): p. 6439-6446.

Chapter 6

Effects of para-Substituents of Styrene Derivatives on Their Chemical Reactivity on Platinum Nanoparticle Surfaces

6.1 Abstract

Stable platinum nanoparticles were successfully prepared by the self-assembly of *para*-substituted styrene derivatives onto the platinum surfaces as a result of platinum-catalyzed dehydrogenation and transformation of the vinyl groups to the acetylene ones, forming platinum–vinylidene/–acetylide interfacial bonds. Transmission electron microscopic measurements showed that the nanoparticles were well dispersed without apparent aggregation, suggesting sufficient protection of the nanoparticles by the organic capping ligands, and the average core diameter was estimated to be 2.0 ± 0.3 nm, 1.3 ± 0.2 nm, and 1.1 ± 0.2 nm for the nanoparticles capped with 4-*tert*-butylstyrene, 4-methoxystyrene, and 4-(trifluoromethyl)styrene, respectively, as a result of the decreasing rate of dehydrogenation with the increasing Taft (polar) constant of the *para*-substituents. Importantly, the resulting nanoparticles exhibited unique photoluminescence, where an increase of the Hammett constant of the *para*-substituents corresponded to a blue-shift of the photoluminescence emission, suggesting an enlargement of the HOMO–LUMO band gap of the nanoparticle-bound acetylene moieties. Furthermore, the resulting nanoparticles exhibited apparent electrocatalytic activity towards oxygen reduction in acidic media, with the best performance among the series of samples observed with the 4-*tert*-butylstyrene-capped nanoparticles due to an optimal combination of the nanoparticle core size and ligand effects on the bonding interactions between platinum and oxygen species.

6.2 Introduction

Organically functionalized transition metal nanoparticles have been attracting extensive research interests from both fundamental and technological perspectives, as their unique optical and electronic properties can be readily manipulated by the chemical nature of the metal cores, the protecting ligands, and the metal–ligand interfacial bonding interactions.[1-6] In fact, in a series of recent studies, a variety of metal–ligand interfacial bonding interactions have been exploited for nanoparticle surface functionalization.[7-14] Among these, metal–carbene (M=C) π bonds are formed by the self-assembly of diazo derivatives on nanoparticle surfaces,[9-11] whereas metal–acetylide (M–C≡C)/metal–vinylidene (M=C=C) bonds are produced by taking advantage of the strong affinity of acetylene moieties to transition-metal surfaces.[12-23] With the formation of such conjugated bonds at the metal–ligand interface, effective intraparticle charge delocalization occurs between particle-bound functional moieties, as manifested in spectroscopic and electrochemical measurements.[16, 19-21] Notably, such nanoparticle-mediated electronic communication has been found to be facilitated by the conducting metal cores and metal–ligand interfacial linkages, which offers a fundamental framework for further and more complicated manipulation of the nanoparticle optical/electronic properties.[11] For instance, for alkyne-caped metal nanoparticles, intraparticle charge delocalization between the particle-bound acetylene moieties may be enhanced (weakened) by the injection (removal) of electrons to (from) the nanoparticle cores, as a result of the manipulation of the metal–ligand bonding interactions.[16] The metal–ligand interfacial bonds may also be readily controlled by deliberate

modification of the organic capping ligands with selected functional moieties that exhibit specific interactions with certain molecules and ions.[21, 24, 25]

More recently, it has been shown that olefin derivatives may also be exploited as a new kind of capping ligand for the preparation of stable Pt nanoparticles.[22] It was found that the resulting nanoparticles exhibited photoluminescence in the visible range, similar to that of Pt nanoparticles functionalized with acetylene derivatives.[15-23] Spectroscopic and electrochemical measurements revealed that the nanoparticles might involve the formation of Pt–acetylide (Pt–C≡C)/Pt–vinylidene (Pt=C=C) interfacial bonds on the Pt nanoparticle surface, as a result of dehydrogenation and transformation of the olefin moieties catalyzed by the Pt nanoparticles. Mechanistically, the chemical reactivity of the olefin ligands is key to the success of nanoparticle surface functionalization. This is the primary motivation for the present study, where we employ a series of para-substituted styrene derivatives as capping ligands for platinum nanoparticle surface functionalization, and examine and compare the chemical reactivity of the ligands, the optical properties and electrocatalytic activities of the eventual nanoparticles within the context of the electron-withdrawing properties of the para-substituents.

It is well-known that within a multi-substituted phenyl ring, apparent electronic interactions occur between the substituent moieties, which may be quantified by the Hammett constant (σ).[26-30] For instance, the acidity of benzoic acid increases with the increasing Hammett constant (electron-withdrawing) of the para-substituent groups.[26, 29, 30] In fact, for platinum nanoparticles functionalized with para-

substituted aliphatic fragments (by using diazonium derivatives as the precursors), we have observed that the electrocatalytic activity towards oxygen reduction reaction (ORR) increases markedly with the increasing Hammett constant of the para-substituent groups, which is ascribed to subtle diminishment of the nanoparticle core electron density and hence reduced interactions with oxygen intermediates, as predicted by the so-called volcano plot.[28]

Herein, three styrene derivatives with different para-substituent groups, 4-tert-butylstyrene (TBS), 4-methoxystyrene (MOS), and 4-(trifluoromethyl)styrene (TFMS), were selected as the protecting ligands for nanoparticle functionalization, where the corresponding Hammett constant of the para-substituents varied rather widely, ranging from electron-donating methoxy ($\sigma = -0.27$) and tert-butyl ($\sigma = -0.20$) groups to the electron-withdrawing trifluoromethyl group ($\sigma = +0.54$).[27] Experimentally, stable nanoparticles were obtained with all three capping ligands and exhibited clearly defined photoluminescence emissions where the peak positions were found to blue-shift with increasing electron-withdrawing capability of the para-substituent groups. Moreover, the nanoparticles exhibited apparent electrocatalytic activity towards ORR in acidic media, and the best performance among the series was observed with the TBS-capped nanoparticles, most probably due to an optimal combination of the nanoparticle core size and electronic properties of the para-substitution.

6.3 Experimental section

Chemicals. Platinum chloride ($PtCl_2$, 99+%, ACROS), sodium acetate trihydrate ($NaOAc \cdot 3H_2O$, MC&B), sodium carbonate (Na_2CO_3, 99.5%, ACROS),

hydrochloric acid (HCl, 37%, ACROS), 4-tert-butylstyrene (TBS, 94%, Alfa Aesar), 4-methoxystyrene (MOS, ⩾ 98%, Sigma-Aldrich), and 4-(trifluoromethyl)styrene (TFMS, 96%, Combi-Blocks Inc.) were all used as received. All solvents were obtained from typical commercial resources at their highest purity and used without further treatment. Water was supplied by a Barnstead Nanopure water system (18.3 MΩ cm).

Synthesis of platinum nanoparticles. Styrene derivative functionalized Pt nanoparticles were prepared by adopting the method developed previously.[19, 22] Briefly, 0.1 mmol of $PtCl_2$ was dissolved in 1 mL of concentrated HCl (12.1 M) at 80 °C, and the obtained solution was neutralized with Na_2CO_3 and centrifuged to remove undissolved salts. The supernatant as well as 1 mmol of NaOAc were added into 100 mL of 1,2-propanediol. The mixed solution was heated up to 165 °C under vigorous stirring for 1 h, and the appearance of a dark brown color signified the formation of "bare" platinum colloids. Once the colloid solution was cooled down to 60 °C, 0.3 mmol of a styrene derivative (TBS, MOS, or TFMS) dissolved in 40 mL of toluene was added (corresponding to a three-fold molar excess of the organic ligands to $PtCl_2$), and the mixed solution was stirred at 60 °C overnight. It was found that with the TBS ligands, almost all the nanoparticles were transferred to the toluene phase, whereas only partial transfer was achieved with the other two ligands. The toluene phase was collected with a separatory funnel, dried with rotary evaporation, and rinsed extensively with a copious amount of acetonitrile (for TBS) or isooctane (for MOS and TFMS) to remove excess ligands, affording purified nanoparticles which were denoted as PtTBS, PtMOS, and PtTFMS, respectively.

Characterization. The morphology and size of the nanoparticles were characterized by transmission electron microscopic studies (TEM, Philips CM300, 300 kV). ^{1}H NMR spectroscopic measurements were carried out with a Varian Unity Inova 500 MHz NMR spectrometer. UV-vis absorption studies were performed with a Perkin-Elmer Lambda 35 spectrometer with a resolution of 1 nm using a 1 cm quartz cuvette. Photoluminescence characteristics were examined with a PTI fluorospectrometer. Infrared measurements were carried out with a Perkin-Elmer FTIR spectrometer (Spectrum One, at a resolution of 4 cm^{-1}) where the samples were prepared by casting the particle solutions onto a ZnSe disk. Thermogravimetric analysis (TGA) was performed with a Perkin-Elmer Pyris 1 Thermogravimetric Analyzer under an ultrahigh-purity N_2 (99.999%) flow at a temperature rate of 10 °C min^{-1}, where the organic contents (by weight) were estimated to be 13.7% for PtTBS, 18.7% for PtMOS, and 33.4% for PtTFMS nanoparticles. X-ray photoelectron spectra (XPS) were recorded with a PHI5400 instrument equipped with an Al Kα source operated at 350 W and at 10^{-9} Torr. The spectra were referenced to the Si 2p peak of a silicon substrate.

Electrochemistry. Electrochemical studies were carried out with a CHI710 electrochemical workstation using a Pt counter electrode and a Ag/AgCl reference electrode at room temperature. Note that the Ag/AgCl reference electrode was calibrated against a reversible hydrogen electrode (RHE), and the results in the present study were all referred to RHE. The working electrode was a rotating ring-disk electrode (RRDE, AFE7R9GCAU from Pine Instrument Co.) with a glassy carbon disk (GC, diameter 5.61 mm) and a gold ring. The collection efficiency (N) was determined

to be 40% by RRDE measurements in 5 mM $K_4Fe(CN)_6$ + 0.1 M KNO_3.[31] The RRDE electrode was prepared according to a procedure proposed by Gloaguen et al.,[32] which has also been adopted in a number of ORR studies.[33-38] In a typical experiment, 500 μg of the platinum nanoparticles obtained above was mixed with 2 mg of XC-72 carbon black (corresponding to a nanoparticle:carbon mass ratio of 1: 4) in 500 μL toluene along with 5 μL of Nafion 117 solution (5 wt%), and dispersed under sonication. A measured volume (ca. 5 μL) of the catalyst ink was then dropcast on the freshly polished GC disk of the RRDE. The solvent was evaporated at room temperature yielding a catalyst loading of ca. 5 μg.

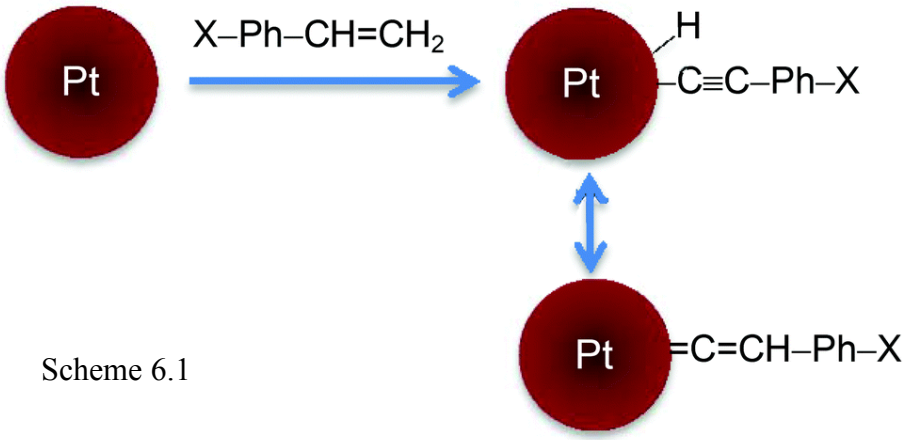

Scheme 6.1

6.4 Results and discussion

As mentioned above, functionalization of Pt nanoparticles by the styrene derivatives was evidenced by the transfer of the nanoparticles from the alcohol phase to toluene. This was due to the replacement of the original acetate ligands by the hydrophobic styrene derivatives that underwent platinum-catalyzed dehydrogenation to produce acetylene derivatives and self-assembled onto the Pt nanoparticle surface

forming Pt–vinylidene (Pt=C=C)/Pt–acetylide (Pt–C≡C) interfacial bonds (Scheme

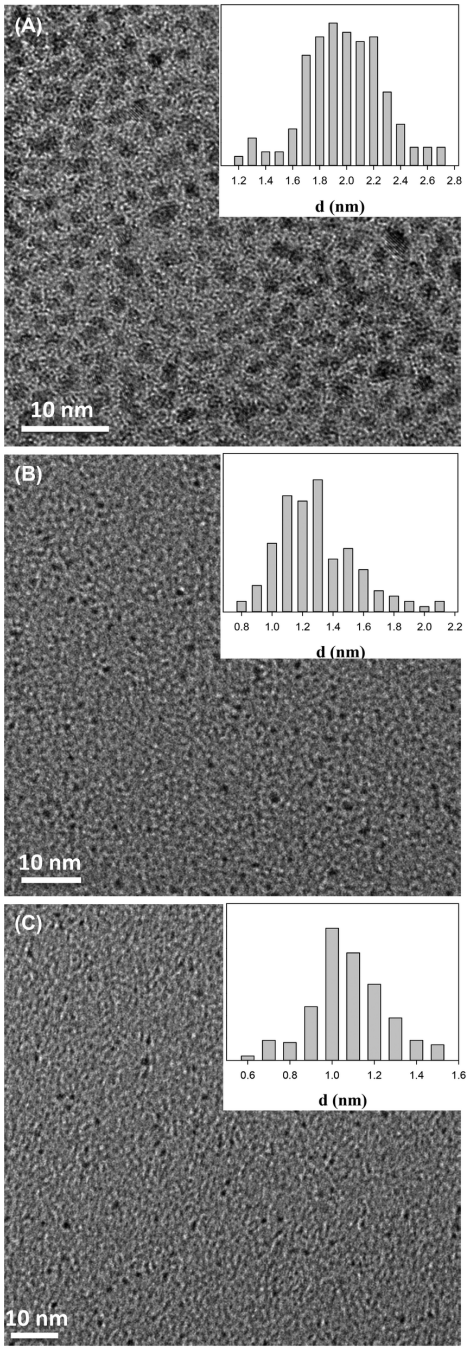

Figure 6.1. Representative TEM images of (A) PtTBS, (B) PtMOS, and (C) PtTFMS. Scale bar are all 10 nm. Insets are the corresponding core size histograms.

6.1).[22] Figure 6.1 depicts the representative TEM micrographs of the three styrene derivative-functionalized Pt nanoparticles. It can be seen that the nanoparticles were all well separated without apparent aggregation, suggesting sufficient protection of the nanoparticles by the capping ligands, due to the apparent chemical reactivity of the olefin moieties on the Pt nanoparticle surface.[22] Interestingly, whereas the same "bare" platinum colloids (average core diameter 2.8 ± 0.6 nm)[19] were used prior to styrene functionalization, the eventual nanoparticles were markedly smaller and exhibited a clear variation of the core size. From the core histograms (Figure 1 insets), one can see that the majority of the PtTBS nanoparticles are within the narrow range of 1.7 to 2.3 nm in diameter, with the average diameter at 2.0 ± 0.3 nm. In contrast, the PtMOS nanoparticles were somewhat smaller, mostly between 1.0 and 1.5 nm with the average diameter at 1.3 ± 0.2 nm; and the PtTFMS nanoparticles were even smaller at 1.1 ± 0.2 nm. This suggests a variation of the chemical reactivity of the three styrene derivatives on platinum nanoparticle surfaces. In fact, previous studies have shown that the rate of dehydrogenation reactions depends on the polar effect of the para-substituents, decreasing with the increasing Taft (polar) constant (σ^*).[39-41] Of the three styrene derivatives under study, the Taft constant increases in the order of tert-butyl ($\sigma^* = -0.30$) < methoxy (($\sigma^* = +1.81$) < trifluoromethyl (($\sigma^* = +2.61$). That is, in comparison with simple olefin, the rate of dehydrogenation would be enhanced with TBS but diminished with MOS or TFMS. Consequently, dehydrogenation of TBS may occur on Pt nanoparticles of a wide range of particle core sizes whereas for MOS and

TFMS they were most likely limited to smaller sizes of the Pt nanoparticles that were more active in catalyzing dehydrogenation reactions.[42-48]

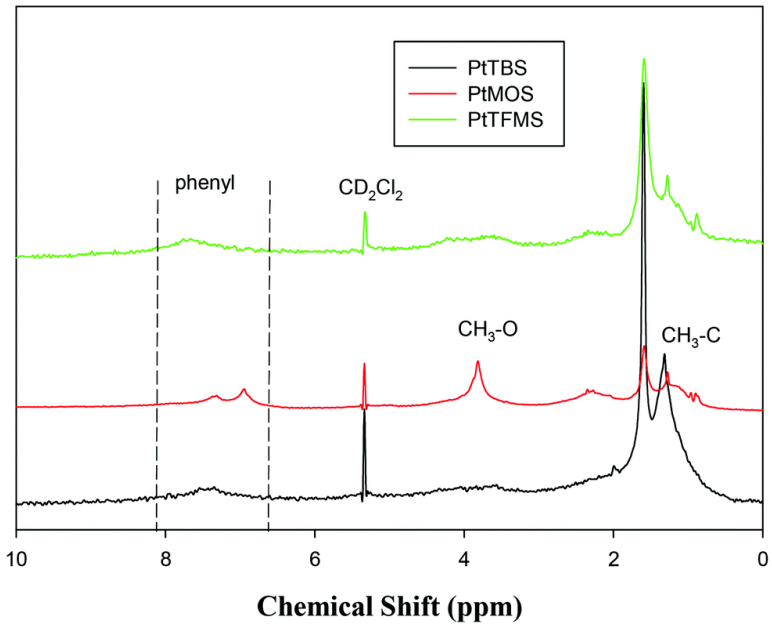

Figure 6.2. ^{1}H NMR spectra of PtTBS (black), PtMOS (red), and PtTFMS (green) nanoparticles in CD_2Cl_2.

The structures of the obtained Pt nanoparticles were then examined by ^{1}H NMR measurements. Figure 6.2 shows the ^{1}H NMR spectra of the PtTBS (black), PtMOS (red), and PtTFMS (green) nanoparticles. For PtTBS nanoparticles the phenyl protons might be identified with the broad peak centered at 7.43 ppm, and the terminal methyl protons at 1.31 ppm. The fact that only broad features were observed suggests that the nanoparticles were spectroscopically clean, and free of excess monomeric ligands[9, 11, 24, 49-51] (the sharp peak at ca. 1.60 ppm was due to residual water). This is consistent with the platinum-catalyzed dehydrogenation of the styrene ligands into

acetylene derivatives that then self-assembled onto the nanoparticle surface, such that the close proximity to the nanoparticle core surface rendered the signals of relevant protons to be broadened into the baseline.[9, 11, 24, 49-51] Similar behaviors can be found with the other two nanoparticle samples: for PtMOS, the phenyl protons appeared as two broad peaks at 7.33 and 6.96 ppm (due to interactions with the electronegative oxygen moiety), and the methoxy protons at 3.83 ppm, whereas for PtTFMS, the phenyl protons can be identified with the broad peak at 7.69 ppm. It should be noted that the observed variations of the chemical shifts of the phenyl protons are consistent with the electron-withdrawing properties of the para-substituents, as manifested by the corresponding Hammett constants (σ): −0.27 for MOS, −0.20 for TBS, and +0.54 for TFMS.[52] Notably, no olefin protons can be found, which are anticipated to emerge at ca. 5.22, 5.74, and 6.69 ppm. These observations indicate the successful dehydrogenation of the terminal vinyl groups of the styrene derivatives which were then self-assembled onto the platinum nanoparticle surface and that the nanoparticles were indeed free of excess ligands.

Further structural insights were obtained in FTIR measurements. Figure 6.3 depicts the FTIR spectra of the PtTBS (black), PtMOS (red), and PtTFMS (green) nanoparticles. One can see that all three nanoparticles exhibited a small vibrational band at ca. 3068 cm^{-1}, which may be assigned to the phenyl ring C–H vibrations. Another rather well-defined vibrational band can be seen at 2039 cm^{-1} for PtTBS, 2057 cm^{-1} for PtMOS, and 2040 and 2084 cm^{-1} for PtTFMS. This may be ascribed to the

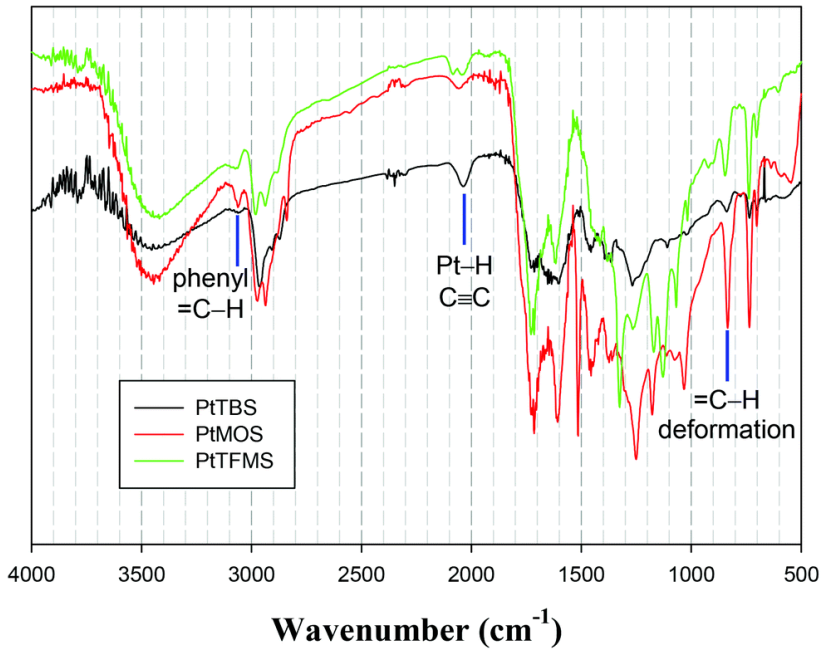

Figure 6.3. FTIR spectra of PtTBS (black), PtMOS (red), and PtTFMS (green) nanoparticles.

combined contributions of the nanoparticle-bound C≡C and =C=C stretches that were formed when the olefin moieties were dehydrogenated forming acetylene groups that self-assembled on Pt surfaces[19, 22] (Scheme 6.1). This has been observed previously with alkyne-functionalized transition-metal nanoparticles where the formation of Pt–vinylidene (Pt=C=C) bonds and intraparticle charge delocalization due to the conjugated metal–ligand interfacial bonds led to a marked red shift of the C≡C vibrational energy, as compared to that of monomeric acetylene moieties.[17, 19] Additional vibrational features include the band near 840 cm^{-1} which most likely arose from the out-of-plane C–H deformation of para-substituted phenyl rings. For PtMOS, the C–O–C symmetric stretching can be identified at 1032 cm^{-1}, while the asymmetric

stretching bands appear at 1247 cm^{-1} along with two shoulders at 1289 cm^{-1} and 1313 cm^{-1}.[53] For PtTFMS nanoparticles, the C–F asymmetric and symmetric stretching vibrations can be found at 1128 and 1172 cm^{-1}, as well as 1327 cm^{-1} respectively.[54] Furthermore, one may see that no olefin (=C–H) vibrations can be found (>3080 cm^{-1}), signifying that indeed the styrene derivatives underwent dehydrogenation reactions on platinum surfaces forming acetylene moieties that were bound onto the Pt nanoparticles and the resulting nanoparticles were free of monomeric ligands (Figure 6.2).

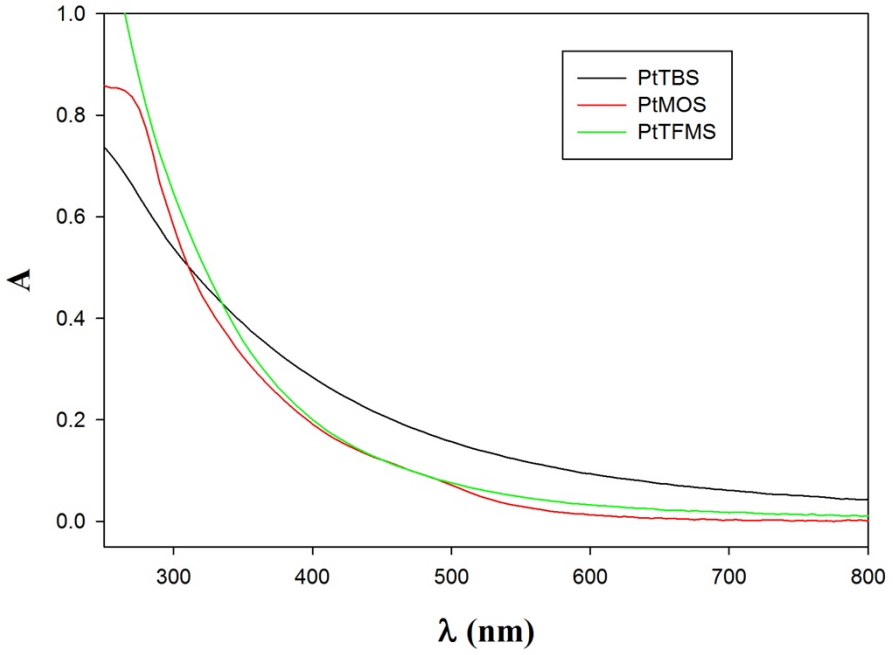

Figure 6.4. UV-vis absorption spectra of PtTBS (black), PtMOS (red), PtTFMS (green) nanoparticles in CH_2Cl_2.

The Pt nanoparticles were then characterized by UV-vis absorption measurements. As depicted in the inset to Figure 6.4, the three nanoparticles exhibited only an exponential decay profile with decreasing photon energy, characteristic of

nanosized metal particles (the so-called Mie scattering).[55, 56] However, the PtMOS (red) and PtTFMS (blue) nanoparticles showed a much steeper decay than PtTBS (black), consistent with the smaller dimensions of the former as determined in TEM measurements (Figure 6.1). The photoluminescence characterization was also carried out. As shown in Figure 6.5, the PtTBS (black), PtMOS (red), and PtTFMS (blue) nanoparticles all displayed apparent and strong photoluminescence, in contrast to the featureless profile observed with the "bare" platinum colloids (green curves). The observed photoluminescence can be attributed to the formation of Pt–C≡C/Pt=C=C

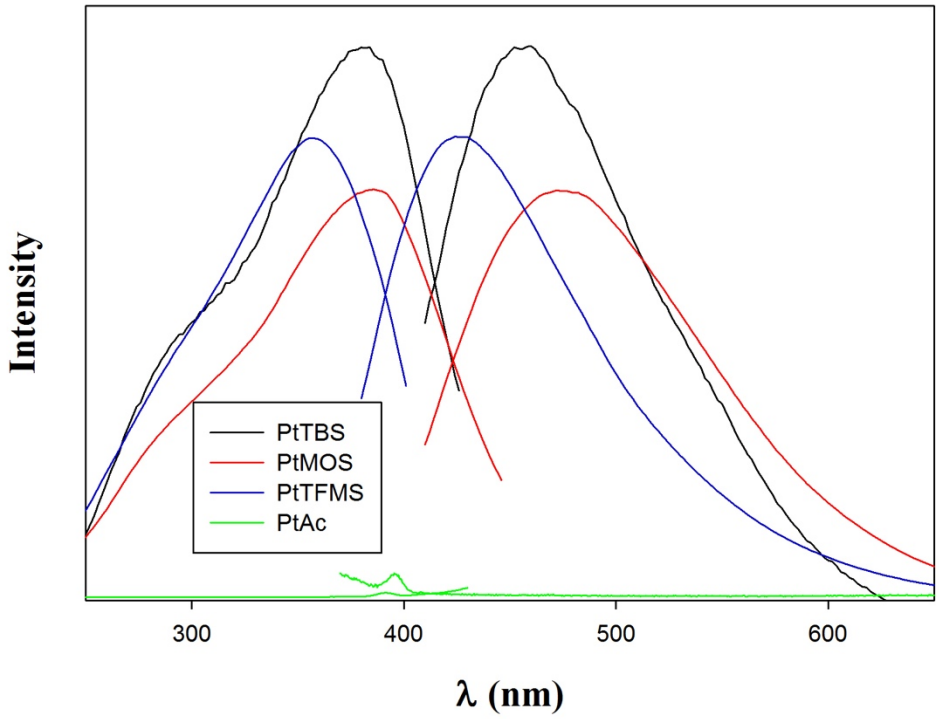

Figure 6.5. Excitation and emission spectra of PtTBS (black), PtMOS (red), PtTFMS (blue) nanoparticles in CH_2Cl_2 and "bare" platinum colloids (green) in 1,2-propanediol.

interfacial bonds as a result of dehydrogenation of the styrene derivatives such that the acetylene moieties bound on the surface of Pt nanoparticles acted analogously to diacetylene derivatives (−C≡C−C≡C−). Similar behaviors have been observed when 1-octadecene was used as the capping ligand.[22] In addition, by using quinine sulphate (1 μM in a 0.05 M H_2SO_4 solution) as a standard, the quantum yields were calculated to be at 0.24%, 5.90%, and 3.90% for the PtTBS, PtMOS, and PtTFMS nanoparticles, respectively.[57, 58] A closer analysis shows that the photoluminescence characteristics actually varied rather significantly with the organic capping ligands. Specifically, one can see that the excitation and emission maxima were identified at 380 nm and 455 nm for PtTBS, 385 nm and 475 nm for PtMOS, and 355 nm and 425 nm for PtTFMS. This suggests that the effective HOMO−LUMO band gap of the particle-bound acetylene derivatives decreases in the order of PtTFMS > PtTBS > PtMOS. Notably, it has been demonstrated that a decrease (increase) of the HOMO−LUMO band gap can be induced by the incorporation of electron-donating (-withdrawing) para-substituent groups to elevate (lower) the molecular HOMO level.[59-63] In the present study, the Hammett constants (σ) increase in the order of methoxy (−0.27) < tert-butyl (−0.20) < trifluoromethyl (+0.54),[26, 27] in good agreement with the variation of the observed nanoparticle photoluminescence emissions. The electronic effects from the organic capping ligands were also reflected in the XPS measurements (Figure 6.6), where the binding energies of the Pt 4f electrons increased in the order of PtMOS < PtTBS < PtTFMS, again, consistent with the order of the Hammett constants. One may also note that the nanoparticle core sizes were

similar between PtMOS and PtTFMS (Figure 6.1), yet these two nanoparticles exhibited markedly different photoluminescence. This suggests that the core size

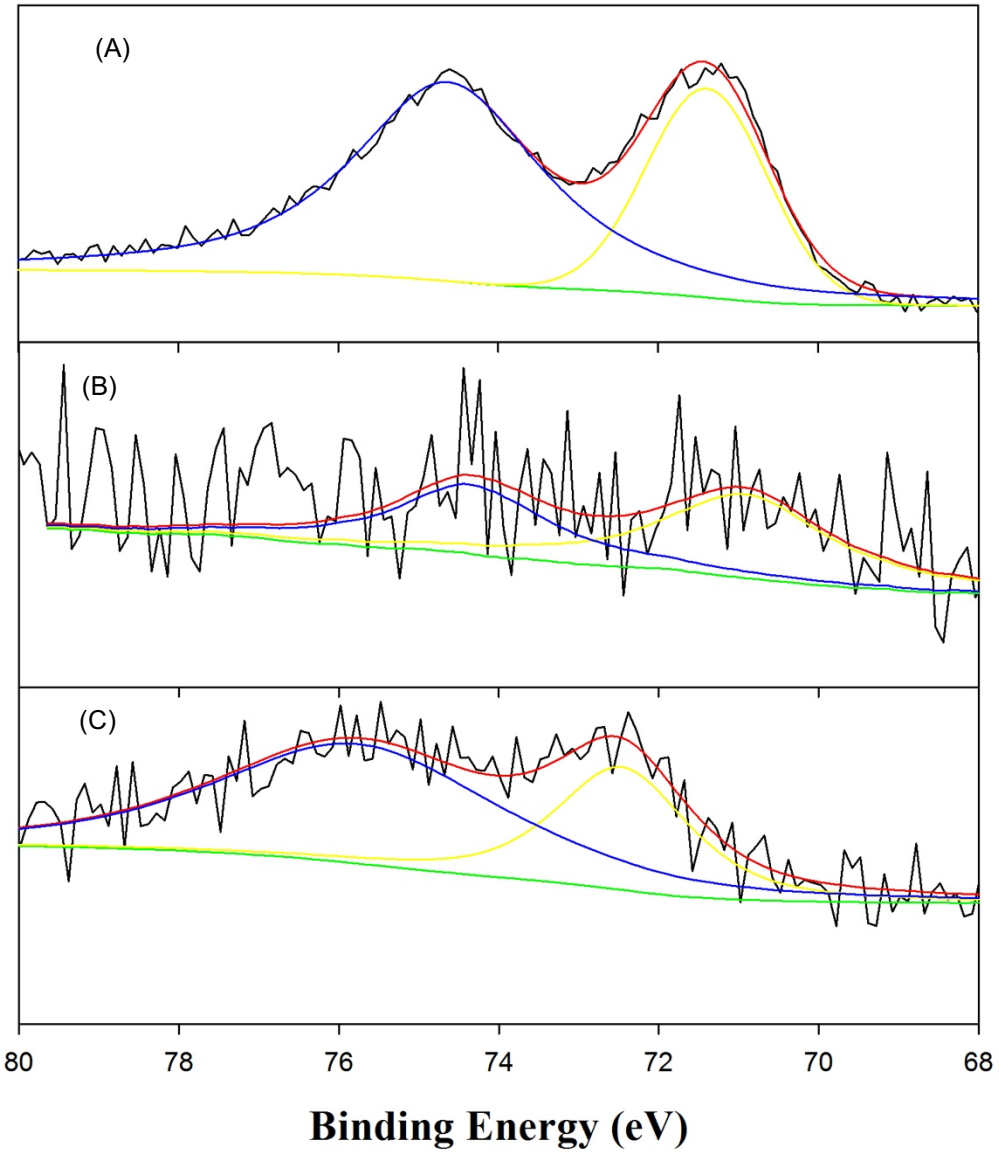

Figure 6.6. XPS spectra of Pt4f electrons in (A) PtTBS, (B) PtMOS, and (C) PtTFMS nanoparticles. Black curves are experimental data and colored curves are deconvolution fits. The binding energies are listed below.

played only a negligible role in determining the nanoparticle photoluminescence; instead, the photoluminescence arose primarily from intraparticle charge delocalization between the nanoparticle-bound acetylene moieties such that they behaved analogously to diacetylene derivatives.[15-23]

The impacts of the para-substituent groups on the nanoparticle electrocatalytic activity towards ORR were then examined by voltammetric measurements in acidic media. Prior to ORR tests, the catalyst-modified electrodes were subjected to an electrochemical activation treatment by rapid potential cycling (500 mV s^{-1}) between 0 and +1.2 V (vs. RHE) in a nitrogen-saturated 0.1 M $HClO_4$ solution until a steady voltammogram was obtained (Figure 6.7). One can see that both PtTBS and PtTFMS nanoparticles exhibited rather well-defined butterfly voltammetric features, characteristic of platinum electrode surfaces;[28, 64-66] yet no such profiles were observed with the PtMOS nanoparticles, implying that it was difficult to electrochemically remove the MOS ligands. This is somewhat unexpected and the origin is not fully understood at this point. One possible explanation is that the strong electron-donating para-methoxy groups led to enhanced strength of the metal–ligand interfacial bonds (vide ante).[16] Figure 6.8(A) depicts the RRDE voltammograms in an oxygen-saturated 0.1 M $HClO_4$ solution at the rotation rate of 1600 rpm. It can be seen that when the electrode potential was swept negatively, nonzero cathodic currents started to emerge for all three samples, suggesting apparent electrocatalytic activity towards ORR; however, the voltammetric profiles clearly differed among the samples. For the PtTBS nanoparticles (black curve), the onset potential for ORR may be

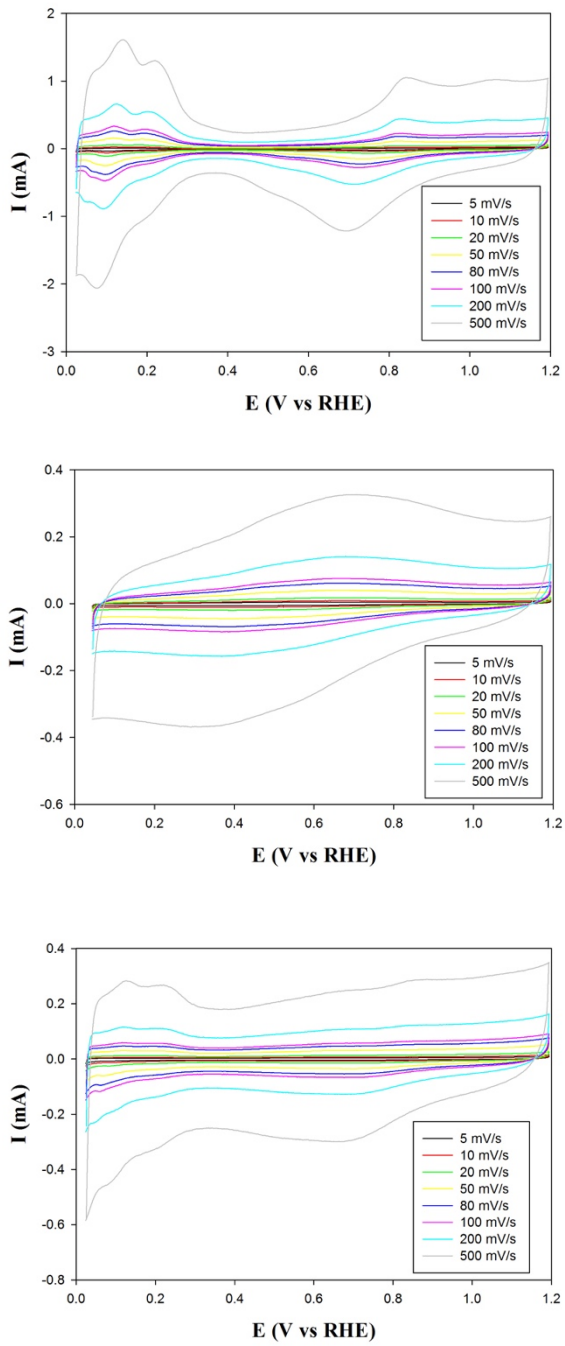

Figure 6.7. Cyclic voltammograms of a glassy carbon electrode modified with (top) PtTBS, (middle) PtMOS, and (bottom) PtTFMS nanoparticles in 0.1 M $HClO_4$ at various potential scan rates. The nanoparticle loadings were all 5 μg, corresponding to a platinum mass of 4.31, 4.06, and 3.33 μg, respectively, as determined by TGA measurements.

identified at around +1.00 V (vs. RHE), and the currents reached a plateau at around

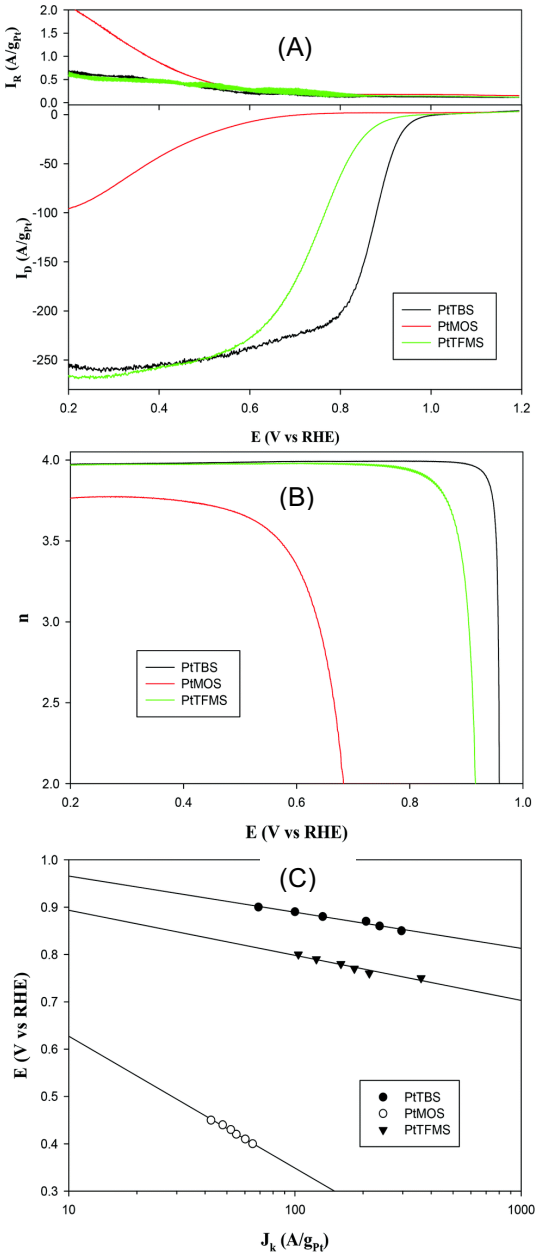

Figure 6.8. (A) RRDE voltammograms of a glassy carbon electron modified with PtTBS, PtMOS and PtTFMS nanoparticles in oxygen-saturated 0.1 M $HClO_4$ at the rotation rate of 1600 RPM. Potential sweep rate 10 mV s^{-1}. The nanoparticle loadings were all 5 μg, corresponding to a platinum mass of 4.31, 4.06, and 3.33 μg, respectively, as determined by TGA measurements. (B) Variation of the number of electron transfers (n) with electrode potentials. Data were calculated from the RRDE voltammograms in panel (A). (C) Tafel plots of the three nanoparticles. Data were calculated from the RRDE voltammograms in panel (A).

+0.80 V (vs. RHE). Such a performance is very comparable to that of commercial Pt/C

catalysts.[28] For the PtTFMS nanoparticles, the activity was somewhat lower, where the onset potential was estimated to be +0.95 V and the current plateau was reached at potentials more negative than +0.60 V. However, for the PtMOS nanoparticles, the RRDE voltammograms did not show apparent cathodic currents until the potential was as negative as +0.80 V, and the current plateau was reached at a far more negative potential of around +0.20 V. Furthermore, one may see that the limiting current also varied among the three nanoparticles. For instance, the limiting currents (mass activity) at +0.20 V and 1600 rpm decrease in the order of PtTFMS (258 A g_{Pt}^{-1}) ≈ PtTBS (254 A g_{Pt}^{-1}) ≫ PtMOS (96 A g_{Pt}^{-1}). Taken together, these observations suggest that PtTBS nanoparticles stood out as the best catalyst among the series of styrene-functionalized platinum nanoparticles towards ORR.

In addition, by setting the ring potential at +1.5 V, collection experiments were carried out to monitor the amounts of peroxide intermediates generated during ORR. It can be seen that for all three samples, the ring currents (I_R) were about two orders of magnitude lower than those at the disk (I_D), suggesting that only minimal amounts of peroxide species were generated during oxygen reduction. In fact, the number of electron transfers (n) can be evaluated by the following equation, $n = 4I_D/(I_D + I_R/N)$.[31, 67, 68] Using the data obtained at 1600 RPM as an example (panel (A)), the n values were calculated for the three samples, as shown in panel (B). It is notable again that the PtTBS nanoparticles exhibited the best ORR performance with the n values above 3.97 within a wide potential range of +0.10 to +0.90 V, suggesting that oxygen primarily underwent four-electron reduction to water, $O_2 + 4H^+ + 4e^- \rightarrow 2H_2O$, with negligible

amounts of peroxide byproducts. PtTFMS nanoparticles also exhibited comparable n values above 3.95 but within a somewhat smaller potential range from +0.10 to +0.80 V. The PtMOS nanoparticles showed the lowest ORR activity among the series, with n values about 3.75 but only at potentials more negative than +0.40 V.

The variation of the electrocatalytic activity towards ORR is further manifested in Koutecky–Levich analysis, where the kinetic current density (I_k) was estimated by removing the diffusion-limited currents (I_L) from the measured voltammetric currents (I_D), $1/I_D = 1/I_L + 1/I_k$. From the Tafel plot in panel (C), one can see that whereas for all three samples the kinetic current density increased markedly with increasingly negative electrode potentials, the activity clearly varied among the samples, decreasing sharply in the order of PtTBS > PtTFMS ≫ PtMOS. Again, the exceedingly low activity of PtMOS might be ascribed to the inaccessibility of the nanoparticle surfaces (Figure 6.7). For the other two nanoparticles, one can see that whereas the para-trifluoromethyl group exhibited a higher Hammett constant ($\sigma = +0.54$) than the tert-butyl group ($\sigma = -0.20$), the activity of PtTBS was actually markedly better than that of PtTFMS. At first glance, this seems to contradict the results observed earlier with para-substituted aryl-functionalized platinum (Pt–Ar–R, with R = $-CH_3$, –F, –Cl, $-OF_3$, and $-CF_3$) nanoparticles,[28] where the ORR activity was found to increase with the increasing Hammett constant of the para-substituent groups. This was accounted for by the (subtly) weakened interactions of the platinum catalysts with oxygen species, as predicted by the so-called volcano plot. Note that in the prior study,[28] the nanoparticles all fell in the narrow range of core diameters from 1.8 to 2.5 nm. For the

PtTBS nanoparticles that are also within this size range (2.0 ± 0.3 nm in diameter, Figure 6.1), the ORR activity actually fit nicely in the changing trend of the Pt–Ar–R nanoparticle series.[28] However, for the PtTFMS sample, the nanoparticle core size was substantially smaller at 1.1 ± 0.2 nm (Figure 6.1), therefore, although the trifluoromethyl group was more electron-withdrawing, the ORR activity was markedly lower. This suggests that the core size effects played a predominant role in the determination of the nanoparticle ORR activity.[69, 70] It might be interpreted by enhanced oxygen adsorption due to the diminished nanoparticle core size,[71, 72] as manifested by the more negative peak potential for the electroreduction of platinum oxide, which was +0.67 V for PtTFMS and +0.70 V for PtTBS (Figure 6.7). For PtTBS nanoparticles, the high ORR activity among the series may be ascribed to an optimal combination of the nanoparticle core size and electronic contributions from the para-substitutions of the organic ligands.

6.5 Conclusions

In this study, stable platinum nanoparticles were prepared by using para-substituted styrene derivatives as the capping ligands, as a result of platinum-catalyzed dehydrogenation and transformation of the olefin groups to acetylene moieties that then self-assembled onto the platinum nanoparticle surface forming platinum–vinylidene/platinum–acetylene interfacial bonds. The chemical reactivity of the styrene ligands was found to vary with the Taft (polar) constant of the para-substituents, as manifested in TEM measurements where the resulting nanoparticles exhibited a clear variation of the core size. FTIR and NMR spectroscopic

measurements confirmed the successful attachments of the organic ligands onto the nanoparticle surface. In photoluminescence measurements a marked discrepancy was observed for the excitation/emission peak positions, suggesting that the HOMO–LUMO band gap of the nanoparticle-bound acetylene moieties might be enlarged by electron-withdrawing para-substituents of the capping ligands, and the photoluminescence emission arose largely from intraparticle charge delocalization between the particle-bound acetylene moieties with negligible contributions from the nanoparticle cores. Electrochemically the resulting nanoparticles exhibited apparent electrocatalytic activity towards ORR, with the best performance among the series observed with the PtTBS nanoparticles, due to an optimal combination of the nanoparticle core size and para-substitutions of the capping ligands that manipulated the electronic interactions between platinum and oxygen species. These results further highlight the significance of interfacial engineering in the manipulation of nanoparticle optical and electronic properties.

6.6 References

1. Chen, S.W., *Impacts of Metal-Ligand Bonding Interactions on the Electron-Transfer Chemistry of Transition-Metal Nanoparticles*, in *Electroanalytical Chemistry: A Series of Advances*. 2009, Taylor and Francis. p. 105-124.
2. Murray, R.W., *Nanoelectrochemistry: Metal nanoparticles, nanoelectrodes, and nanopores.* Chemical Reviews, 2008. **108**(7): p. 2688-2720.
3. Chen, S.W., Z.H. Zhao, and H. Liu, *Charge Transport at the Metal-Organic Interface.* Annual Review of Physical Chemistry, Vol 64, 2013. **64**: p. 221-245.

4. Yang, G., et al., *Gold Nanoparticle Monolayers with Tunable Optical and Electrical Properties.* Langmuir, 2016. **32**(16): p. 4022-4033.

5. Vasantha, V.A., et al., *Salt-Responsive Polysulfabetaines from Acrylate and Acrylamide Precursors: Robust Stabilization of Metal Nanoparticles in Hyposalinity and Hypersalinity.* Langmuir, 2015. **31**(40): p. 11124-11134.

6. Wang, B., et al., *Methodology for Robust Superhydrophobic Fabrics and Sponges from In Situ Growth of Transition Metal/Metal Oxide Nanocrystals with Thiol Modification and Their Applications in Oil/Water Separation.* Acs Applied Materials & Interfaces, 2013. **5**(5): p. 1827-1839.

7. Mirkhalaf, F., J. Paprotny, and D.J. Schiffrin, *Synthesis of metal nanoparticles stabilized by metal-carbon bonds.* Journal of the American Chemical Society, 2006. **128**(23): p. 7400-7401.

8. Laurentius, L., et al., *Diazonium-Derived Aryl Films on Gold Nanoparticles: Evidence for a Carbon-Gold Covalent Bond.* Acs Nano, 2011. **5**(5): p. 4219-4227.

9. Chen, W., et al., *Carbene-functionalized ruthenium nanoparticles.* Chemistry of Materials, 2006. **18**(22): p. 5253-5259.

10. Kang, X.W., et al., *Intraparticle Charge Delocalization of Carbene-Functionalized Ruthenium Nanoparticles Manipulated by Selective Ion Binding.* Langmuir, 2011. **27**(20): p. 12636-12641.

11. Chen, W., et al., *Nanoparticle-mediated intervalence transfer.* Journal of the American Chemical Society, 2008. **130**(36): p. 12156-12162.

12. Zhang, S., K.L. Chandra, and C.B. Gorman, *Self-assembled monolayers of terminal alkynes on gold.* Journal of the American Chemical Society, 2007. **129**(16): p. 4876-+.

13. Maity, P., et al., *Binding Motif of Terminal Alkynes on Gold Clusters.* Journal of the American Chemical Society, 2013. **135**(25): p. 9450-9457.

14. Ford, M.J., R.C. Hoft, and A. McDonagh, *Theoretical study of ethynylbenzene adsorption on Au(111) and implications for a new class of self-assembled monolayer.* Journal of Physical Chemistry B, 2005. **109**(43): p. 20387-20392.

15. Chen, W., et al., *Alkyne-Protected Ruthenium Nanoparticles.* Journal of Physical Chemistry C, 2010. **114**(42): p. 18146-18152.

16. Kang, X.W., et al., *Alkyne-Stabilized Ruthenium Nanoparticles: Manipulation of Intraparticle Charge Delocalization by Nanoparticle Charge States.* Angewandte Chemie-International Edition, 2010. **49**(49): p. 9496-9499.

17. Kang, X., et al., *Alkyne-functionalized ruthenium nanoparticles: ruthenium-vinylidene bonds at the metal-ligand interface.* J Am Chem Soc, 2012. **134**(3): p. 1412-1415.

18. Kang, X.W. and S.W. Chen, *Electronic conductivity of alkyne-capped ruthenium nanoparticles.* Nanoscale, 2012. **4**(14): p. 4183-4189.

19. Liu, K., et al., *Platinum nanoparticles functionalized with acetylene derivatives: Electronic conductivity and electrocatalytic activity in oxygen reduction.* Journal of Electroanalytical Chemistry, 2013. **688**: p. 143-150.

20. Phebus, B.D., et al., *Intraparticle donor-acceptor dyads prepared using conjugated metal-ligand linkages.* Physical Chemistry Chemical Physics, 2013. **15**(40): p. 17647-17653.

21. Hu, P.G., et al., *Platinum Nanoparticles Functionalized with Ethynylphenylboronic Acid Derivatives: Selective Manipulation of Nanoparticle Photoluminescence by Fluoride Ions.* Langmuir, 2014. **30**(18): p. 5224-5229.

22. Hu, P.G., et al., *Self-Assembly and Chemical Reactivity of Alkenes on Platinum Nanoparticles.* Langmuir, 2015. **31**(1): p. 522-528.

23. Hu, P.G., et al., *Electrocatalytic activity of alkyne-functionalized AgAu alloy nanoparticles for oxygen reduction in alkaline media.* Nanoscale, 2015. **7**(21): p. 9627-9636.

24. Chen, W., et al., *Pyrene-Functionalized Ruthenium Nanoparticles: Novel Fluorescence Characteristics from Intraparticle Extended Conjugation.* Journal of Physical Chemistry C, 2009. **113**(39): p. 16988-16995.

25. Kang, X.W., et al., *Manipulation of Intraparticle Charge Delocalization by Selective Complexation of Transition-Metal Ions with Histidine Moieties.* Analytical Chemistry, 2012. **84**(4): p. 2025-2030.

26. Hammett, L.P., *The effect of structure upon the reactions of organic compounds benzene derivatives.* Journal of the American Chemical Society, 1937. **59**: p. 96-103.

27. Hansch, C., A. Leo, and R.W. Taft, *A Survey of Hammett Substituent Constants and Resonance and Field Parameters.* Chemical Reviews, 1991. **91**(2): p. 165-195.

28. Zhou, Z.Y., et al., *Ligand-Mediated Electrocatalytic Activity of Pt Nanoparticles for Oxygen Reduction Reactions.* Journal of Physical Chemistry C, 2012. **116**(19): p. 10592-10598.

29. Hollingsworth, C.A., P.G. Seybold, and C.M. Hadad, *Substituent effects on the electronic structure and pK(a) of benzoic acid.* International Journal of Quantum Chemistry, 2002. **90**(4-5): p. 1396-1403.

30. Huang, Y., et al., *Modeling Molecular Acidity with Electronic Properties and Hammett Constants for Substituted Benzoic Acids.* Journal of Physical Chemistry A, 2011. **115**(51): p. 14697-14707.

31. Zhou, Z.Y., et al., *Enhancement of the electrocatalytic activity of Pt nanoparticles in oxygen reduction by chlorophenyl functionalization.* Chemical Communications, 2012. **48**(28): p. 3391-3393.

32. Gloaguen, F., et al., *Kinetic-Study of Electrochemical Reactions at Catalyst-Recast Ionomer Interfaces from Thin Active Layer Modeling.* Journal of Applied Electrochemistry, 1994. **24**(9): p. 863-869.

33. Markovic, N.M., et al., *Oxygen Reduction Reaction on Pt and Pt Bimetallic Surfaces: A Selective Review.* Fuel Cells, 2001. **1**(2): p. 105-116.

34. Wang, R.Y., et al., *Nanoporous surface alloys as highly active and durable oxygen reduction reaction electrocatalysts.* Energy & Environmental Science, 2012. **5**(1): p. 5281-5286.

35. Shao, M.H., et al., *Structural dependence of oxygen reduction reaction on palladium nanocrystals.* Chemical Communications, 2011. **47**(23): p. 6566-6568.

36. Spanos, I., et al., *PtxCo1-x alloy NPs prepared by colloidal tool-box synthesis: The effect of de-alloying on the oxygen reduction reaction activity.* International Journal of Hydrogen Energy, 2014. **39**(17): p. 9143-9148.

37. Wang, C., N.M. Markovic, and V.R. Stamenkovic, *Advanced Platinum Alloy Electrocatalysts for the Oxygen Reduction Reaction.* Acs Catalysis, 2012. **2**(5): p. 891-898.

38. Tang, Q.W., et al., *Effect of Surface Manganese Valence of Manganese Oxides on the Activity of the Oxygen Reduction Reaction in Alkaline Media.* Acs Catalysis, 2014. **4**(2): p. 457-463.

39. Gulkova, D. and M. Kraus, *Substituent Effects on the Rate of Dehydrogenation of Primary and Secondary Alcohols.* Journal of Molecular Catalysis, 1994. **87**(1): p. 47-55.

40. Yang, M.C., R.M. Rioux, and G.A. Somorjai, *Reaction kinetics and in situ sum frequency generation surface vibrational spectroscopy studies of cycloalkene hydrogenation/dehydrogenation on Pt(111): Substituent effects and CO poisoning.* Journal of Catalysis, 2006. **237**(2): p. 255-266.

41. Buelow, M.T. and A.J. Gellman, *Correlations between substituent effects for surface reactions and catalytic reactions.* Journal of Molecular Catalysis a-Chemical, 1998. **131**(1-3): p. 55-70.

42. Rioux, R.M., et al., *Influence of Particle Size on Reaction Selectivity in Cyclohexene Hydrogenation and Dehydrogenation over Silica-Supported Monodisperse Pt Particles.* Catalysis Letters, 2008. **126**(1-2): p. 10-19.

43. Vajda, S., et al., *Subnanometre platinum clusters as highly active and selective catalysts for the oxidative dehydrogenation of propane.* Nature Materials, 2009. **8**(3): p. 213-216.

44. Kon, K., S.M.A.H. Siddiki, and K.I. Shimizu, *Size- and support-dependent Pt nanocluster catalysis for oxidant-free dehydrogenation of alcohols.* Journal of Catalysis, 2013. **304**: p. 63-71.

45. Zhu, J., et al., *Size-Dependent Reaction Mechanism and Kinetics for Propane Dehydrogenation over Pt Catalysts.* Acs Catalysis, 2015. **5**(11): p. 6310-6319.

46. Nakamura, M., M. Yamada, and A. Amano, *Size distribution of platinum dispersed on charcoal and its effect on the dehydrogenation of 2,3-dimethylbutane.* Journal of Catalysis, 1975. **39**(1): p. 125-133.

47. Kumar, M.S., et al., *Dehydrogenation of propane over Pt-SBA-15: Effect of Pt particle size.* Catalysis Communications, 2008. **9**(5): p. 747-750.

48. Kumar, M.S., et al., *Dehydrogenation of propane over Pt-SBA-15 and Pt-Sn-SBA-15: Effect of Sn on the dispersion of Pt and catalytic behavior.* Catalysis Today, 2009. **142**(1-2): p. 17-23.

49. Chen, W., et al., *Pyrene-Functionalized Ruthenium Nanoparticles as Effective Chemosensors for Nitroaromatic Derivatives.* Analytical Chemistry, 2010. **82**(2): p. 461-465.

50. Hostetler, M.J., et al., *Alkanethiolate gold cluster molecules with core diameters from 1.5 to 5.2 nm: Core and monolayer properties as a function of core size.* Langmuir, 1998. **14**(1): p. 17-30.

51. Terrill, R.H., et al., *Monolayers in Three Dimensions: NMR, SAXS, Thermal, and Electron Hopping Studies of Alkanethiol Stabilized Gold Clusters.* Journal of the American Chemical Society, 1995. **117**(50): p. 12537-12548.

52. Silverstein, R.M., G.C. Bassler, and T.C. Morrill, *Spectrometric Identification of Organic Compounds, 5th ed.* 1991, New York: Wiley.

53. Katritzky, A.R. and N.A. Coats, *Infrared Absorption of Substituents in Aromatic Systems .1. Methoxy-Compound and Ethoxy-Compounds.* Journal of the Chemical Society, 1959(Jun): p. 2062-2066.

54. Randle, R.R. and D.H. Whiffen, *The Characteristic Infrared Absorption Frequencies of Aromatic Trifluoromethyl Compounds.* Journal of the Chemical Society, 1955: p. 1311-1313.

55. Creighton, J.A. and D.G. Eadon, *Ultraviolet Visible Absorption-Spectra of the Colloidal Metallic Elements.* Journal of the Chemical Society-Faraday Transactions, 1991. **87**(24): p. 3881-3891.

56. Jain, P.K., et al., *Calculated absorption and scattering properties of gold nanoparticles of different size, shape, and composition: Applications in*

biological imaging and biomedicine. Journal of Physical Chemistry B, 2006. **110**(14): p. 7238-7248.

57. Brouwer, A.M., *Standards for photoluminescence quantum yield measurements in solution (IUPAC Technical Report).* Pure and Applied Chemistry, 2011. **83**(12): p. 2213-2228.

58. Suzuki, K., et al., *Reevaluation of absolute luminescence quantum yields of standard solutions using a spectrometer with an integrating sphere and a back-thinned CCD detector.* Physical Chemistry Chemical Physics, 2009. **11**(42): p. 9850-9860.

59. Zophel, L., V. Enkelmann, and K. Mullen, *Tuning the HOMO-LUMO Gap of Pyrene Effectively via Donor-Acceptor Substitution: Positions 4,5 Versus 9,10.* Organic Letters, 2013. **15**(4): p. 804-807.

60. Eakins, G.L., et al., *Tuning HOMO-LUMO levels: trends leading to the design of 9-fluorenone scaffolds with predictable electronic and optoelectronic properties.* Journal of Physical Organic Chemistry, 2011. **24**(11): p. 1119-1128.

61. Priya, P.A., C.P. Kala, and D.J. Thiruvadigal, *Investigation on the influence of substitute groups in organic nanodevices.* International Journal of nanoelectronics and materials, 2010. **3**(1): p. 1-7.

62. Hsieh, C.P., et al., *Synthesis and characterization of porphyrin sensitizers with various electron-donating substituents for highly efficient dye-sensitized solar cells.* Journal of Materials Chemistry, 2010. **20**(6): p. 1127-1134.

63. Wu, J., et al., *A tetrathiafulvalene-tetracyanoanthraquinodimethane (TTF-TCNAQ) diad with a chemically tunable HOMO-LUMO gap.* Tetrahedron, 2007. **63**(46): p. 11282-11286.

64. He, G.Q., et al., *Oxygen Reduction Catalyzed by Platinum Nanoparticles Supported on Graphene Quantum Dots.* Acs Catalysis, 2013. **3**(5): p. 831-838.

65. Markovic, N.M. and P.N. Ross, *Electrocatalysts by design: from the tailored surface to a commercial catalyst.* Electrochimica Acta, 2000. **45**(25-26): p. 4101-4115.

66. Spendelow, J.S. and A. Wieckowski, *Noble metal decoration of single crystal platinum surfaces to create well-defined bimetallic electrocatalysts.* Physical Chemistry Chemical Physics, 2004. **6**(22): p. 5094-5118.

67. Niu, W., et al., *Mesoporous N-Doped Carbons Prepared with Thermally Removable Nanoparticle Templates: An Efficient Electrocatalyst for Oxygen Reduction Reaction.* Journal of the American Chemical Society, 2015. **137**(16): p. 5555-5562.

68. Tang, Y.F., et al., *Electrocatalytic Activity of Nitrogen-Doped Carbon Nanotube Cups.* Journal of the American Chemical Society, 2009. **131**(37): p. 13200-13201.

69. Shao, M.H., A. Peles, and K. Shoemaker, *Electrocatalysis on Platinum Nanoparticles: Particle Size Effect on Oxygen Reduction Reaction Activity.* Nano Letters, 2011. **11**(9): p. 3714-3719.

70. Perez-Alonso, F.J., et al., *The Effect of Size on the Oxygen Electroreduction Activity of Mass-Selected Platinum Nanoparticles.* Angewandte Chemie-International Edition, 2012. **51**(19): p. 4641-4643.

71. Briot, P., et al., *Effect of Particle-Size on the Reactivity of Oxygen-Adsorbed Platinum Supported on Alumina.* Applied Catalysis, 1990. **59**(1): p. 141-152.

72. Han, B.C., C.R. Miranda, and G. Ceder, *Effect of particle size and surface structure on adsorption of O and OH on platinum nanoparticles: A first-principles study.* Physical Review B, 2008. **77**(7).

Chapter 7

Electrocatalytic Activity of Alkyne-Functionalized AgAu Alloy Nanoparticles for Oxygen Reduction in Alkaline Media

7.1 Abstract

1-Dodecyne-functionalized AgAu alloy nanoparticles were synthesized by chemical reduction of metal salt precursors at varied initial feed ratios. Transmission electron microscopic measurements showed that the nanoparticles were all rather well dispersed with the average core diameter in the narrow range of 3 to 5 nm. X-ray photoelectron spectroscopic studies confirmed the formation of AgAu alloy nanoparticles with the gold concentration ranging from approximately 25 at% to 55 at%. Consistent results were obtained in UV-vis spectroscopic measurements where the nanoparticle surface plasmon resonance red-shifted almost linearly with increasing gold concentrations. The self-assembly of 1-dodecyne ligands on the nanoparticle surface was manifested in infrared spectroscopic measurements. Importantly, the resulting nanoparticles exhibited apparent electrocatalytic activity for oxygen reduction in alkaline media, and the performance was found to show a volcano variation in the Au content in the alloy nanoparticles, with the best performance observed for the samples with *ca.* 35.5 at% Au. The enhanced catalytic activity, as compared to pure Ag nanoparticles or even commercial Pt/C catalysts, was accounted for by the unique metal–ligand interfacial bonding interactions as well as alloying effects that increased metal–oxygen affinity.

7.2 Introduction

Low-temperature fuel cell technology has been attracting considerable interest as a means of directly converting chemical energy into electrical energy because of the attractive efficiency and environmental benefits.[1, 2] The types of fuel cells under

active development include alkaline fuel cells (AFC), polymer electrolyte membrane fuel cells (PEMFC), and alkaline polymer electrolyte fuel cells (APEFC).[1, 3] In these systems, because of the sluggish kinetics of the oxygen reduction reaction (ORR) at the cathode, $O_2 + 2H_2O + 4e^- \rightarrow 4OH^-$, a large amount of platinum is typically required to catalyze the reaction so that a sufficiently high current density can be generated for practical applications.[4] Such dependence on Pt catalysts has significantly hindered the widespread application of fuel cells due to the high costs and limited reserves of Pt.[4] Therefore, numerous efforts have been devoted to the improvement of Pt efficiency and/or to the development of Pt-free effective alternative catalysts.[5-8] In recent years, non-Pt catalysts, such as carbon nanomaterials,[9, 10] metal oxides,[11, 12] and non-Pt-group metals,[13-15] have been reported to exhibit considerable mass-specific activities. However, carbon nanomaterials and metal oxides in general suffer from low volume-specific activity and insufficient electronic conductivity, respectively. Non-Pt metals or metal alloys might be a promising alternative because of their high electronic conductivity and abundant catalytic sites to fulfil the requirements for fuel cell catalysis,[13, 16, 17] especially with the significant progress in the study of alkaline polymer electrolytes used in APEFC,[18, 19] which provide a low-corrosion environment to mitigate the instability of non-Pt metal catalysts in acidic electrolytes commonly used in PEMFC.

Among these, silver has been gaining increasing attention as a viable candidate for non-Pt catalyst materials for ORR in alkaline media since the early stage of AFC.[20-22] Compared with other non-Pt catalysts, such as Pd,[23, 24] Au,[25, 26]

Ni,[27, 28] and Co,[27, 28] silver is relatively inexpensive and displays high catalytic activity where ORR proceeds via the 4-electron reduction route.[21, 22] However, the overall catalytic activity of Ag for ORR remains inferior to that of Pt, as manifested by a more negative onset potential, lower kinetic current density, and smaller electron-transfer number. Apparently, further improvement of the ORR activity is necessary in order for silver to be competitive and viable in ORR electrocatalysis. This is the primary motivation of the present study.

Note that a number of strategies have been proposed and explored to improve the electrocatalytic performance of metal catalysts for ORR, including manipulation of elemental composition,[29-31] size,[31-33] morphology,[31, 34-36] and surface atomic arrangement.[31, 37, 38] Whereas the enhancement mechanism has not been fully understood, modification of the d-band centers and formation of lattice geometrical strains have been suggested as two leading factors that may impact the binding of oxygen and reaction intermediates on the metal surfaces and hence the eventual ORR performance. Of these, alloying with a second metal is an effective route to the enhancement of the ORR performance by combining the effects of elemental composition and surface structures of the metal catalysts.[29, 39, 40] Remarkably, whereas the ORR catalytic performance of gold alone is even lower, AgAu alloyed catalysts have been found to display a significantly improved performance as a result of increasing metal–oxygen affinity.[3, 41] For instance, by coating Ag onto Au electrode surfaces, the ORR activity in 0.1 M KOH was found to increase by half an order of magnitude.[3] In another study, by incorporating only ca. 5% of gold onto Ag

nanoparticles by galvanic exchange reactions, the resulting nanoparticles were over seven times more active than the original silver nanoparticles in ORR.[41]

It should be noted that in these prior studies, the composition of the AgAu bimetallic alloy catalysts has remained unoptimized for ORR. Herein, 1-dodecyne functionalized AgAu alloy nanoparticles were prepared by chemical reduction of metal salt precursors at different initial feed ratios and used as a model system to examine the ORR electrocatalytic activity, using pure Ag nanoparticles as the comparative example.[41, 42] This is partly motivated by some of our previous studies where alkynes served as effective capping ligands for nanoparticle stabilization and functionalization and the resulting nanoparticles exhibited apparent electrocatalytic activity, as compared to those capped with alkanethiolates, thanks to the unique metal–ligand interfacial bonding interactions.[43, 44] The results indicated that the sample with ca. 35.5 at% Au exhibited the best ORR catalytic activity among the series, most probably as a result of the optimized metal–oxygen affinity.

7.3 Experimental section

Chemicals. Silver nitrate ($AgNO_3$, Fisher Scientific), hydrogen tetrachloroauric acid ($HAuCl_4$, ACROS), sodium borohydride (NaBH4, ≥98%, ACROS), tetra-n-octylammonium bromide (TOABr, 98%, ACROS), 1-oleylamine (>40%, TCI), and 1-dodecyne (98%, ACROS) were all used as received without any further purification. Solvents were purchased at the highest purity available from typical commercial sources and also used as received. Water was deionized with a Barnstead Nanopure water system (18.3 MΩ·cm).

Synthesis of AgAu alloy nanoparticles. Experimentally, $AgNO_3$ and $HAuCl_4$ (2 mmol in total at six different feed ratios, denoted as #1 to #6 with decreasing Au contents) were dissolved in 5 mL of water. The solution was mixed with 5 mL of a toluene solution of TOABr (0.6 mmol) under vigorous stirring for 1 h. The organic phase was then collected, into which was added 400 μL of 1-oleyamine. After magnetic stirring for 1 h, 1 mL of a freshly prepared $NaBH_4$ solution (80 mg mL^{-1}) in water was added into the solution where the color was found to turn dark red immediately, signifying the formation of nanoparticles. The reaction mixture was stirred for 4 h before the organic phase was collected and washed five times with methanol to remove the phase transfer catalysts, excessive reagents, and reaction byproducts. The collected nanoparticles were then dissolved in CH2Cl2 along with 0.6 mmol of 1-dodecyne. The mixed solutions were stirred overnight and washed with methanol five times to remove free ligands.

Characterization. The morphology and size of the nanoparticles were characterized by transmission electron microscopic studies (TEM, Philips CM300 at 300 kV). Experimentally, a dilute solution of the nanoparticles (<1 mg mL^{-1} in CH_2Cl_2) was prepared and dropcast onto a TEM grid. At least 200 nanoparticles were measured to obtain a size histogram. UV-vis spectra were collected with a Unicam ATI UV4 spectrometer using a 1 cm quartz cuvette. FTIR measurements were carried out with a Perkin-Elmer FTIR spectrometer (Spectrum One, spectral resolution 4 cm^{-1}), where the samples were prepared by casting the particle solutions onto a NaCl disk. X-ray photoelectron spectra (XPS) were recorded with a PHI 5400/XPS instrument equipped

with an Al Kα source operated at 350 W and 10^{-9} Torr. Silicon wafers were sputtered by using argon ions to remove carbon from the background and used as substrates with the binding energy of Si 2p electrons as the reference.

Electrochemistry. The electrochemical setup consisted of a CHI710 electrochemical workstation with a Pt counter electrode and a Ag/AgCl reference electrode at room temperature. The working electrode was a rotating ring-disk electrode (RRDE, AFE7R9GCAU from Pine Instrument Co.) with a glassy carbon disk (GC, diameter 5.61 mm) and a gold ring. The collection efficiency (N) was determined to be 40% by RRDE measurements in 5 mM $K_4Fe(CN)_6$ + 0.1 M KNO_3.[45] The RRDE electrode was prepared according to a procedure proposed by Gloaguen et al.,[46] which has been used extensively in ORR studies.[47-52] In a typical experiment, 250 μg of the AgAu nanoparticles was mixed with 1 mg of XC-72 carbon black (metal: carbon mass ratio = 1:4) in 250 mL of toluene with 2.5 μL of a Nafion® 117 solution (5 wt%) and dispersed under sonication. A measured volume (ca. 6 μL) of this catalyst ink was then transferred via a Hamilton microliter syringe onto the freshly polished glassy carbon disk. The solvent was evaporated at room temperature yielding a catalytic loading of 30 μg with ca. 6 μg of nanoparticles (20 wt%).

7.4 Results and discussion.

The size and morphology of the AgAu alloy nanoparticles were first characterized by TEM measurements, as shown in Figure 7.1. It can be seen that the nanoparticles were all dispersed very well without significant aggregation, indicating effective protection of the nanoparticles by using the 1-dodecyne ligands. Statistical

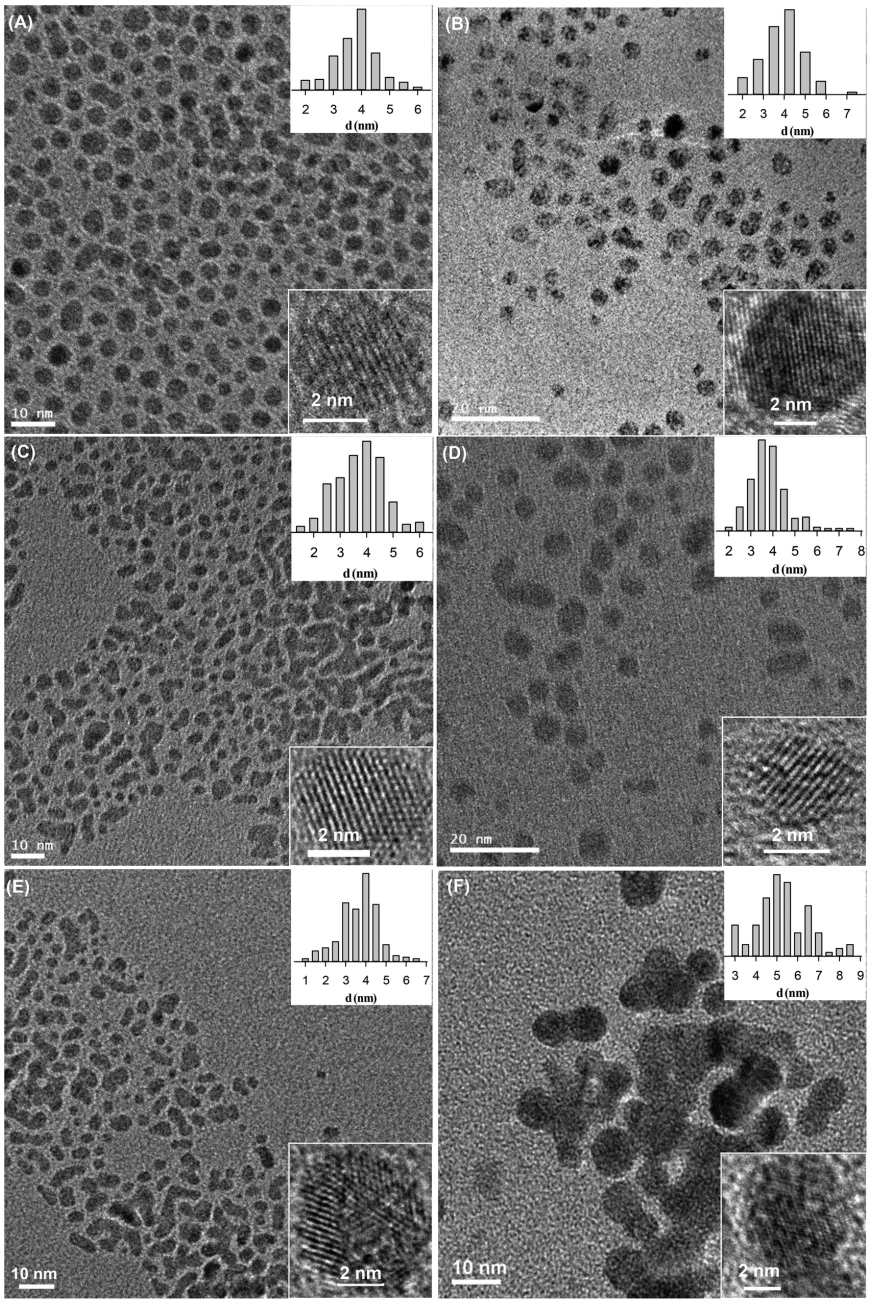

Figure 7.1. Representative TEM micrographs of AgAu nanoparticles at varied atomic compositions: (A) #1, (B) #2, (C) #3, (D) #4, and (E) #5, and (F) #6. Lower insets are the corresponding high-resolution images and upper insets the core size histograms.

analysis based on over 200 nanoparticles showed that the average core diameter of the

AgAu alloy nanoparticles was rather consistent at around 4.0 nm, except for sample #6 which is somewhat larger: (A, #1) 3.85 ± 0.64 nm, (B, #2) 3.97 ± 0.94 nm, (C, #3) 3.78 ± 0.95 nm, (D, #4) 3.68 ± 0.67 nm, (E, #5) 3.79 ± 0.84 nm, and (F, #6) 5.17 ± 1.14 nm, as depicted in the respective upper inset (and summarized in Table 7.1). Furthermore, the nanoparticles all exhibited well-defined crystalline lattice fringes, as highlighted in the lower insets, with an interlayer spacing of 0.235 nm that is consistent with the (111) planes of both fcc silver (PDF Card #4-783) and gold (PDF Card #4-784).

Table 7.1 Summary of the average core diameter (d, nm), gold atomic concentration (at%), electrochemical surface area (ECSA, $m^2\ g^{-1}$), onset potential (E_{onset}, V vs. RHE), specific activity (J_s, A m^{-2}), mass activity (J_m, A g^{-1}) and Tafel slopes in ORR of AgAu nanoparticles.

AgAu		**#1**	**#2**	**#3**	**#4**	**#5**	**#6**
d (nm)		3.85 ± 0.64	3.97 ± 0.94	3.78 ± 0.95	3.68 ± 0.67	3.79 ± 0.84	5.17 ± 1.14
Au at%		56.5	51.5	39.2	35.5	31.5	26.7
ECSA ($m^2\ g^{-1}$)		41.8	41.4	29.5	40.0	25.8	20.9
E_{onset} (V)		+0.90	+0.90	+0.90	0.92	0.91	0.89
J_s (A m^{-2}, +0.85 V)		75.2	33.5	43.4	95.6	45.2	38.2
Tafel slope (mV dec^{-1})	$J_s < 2.5$ A m^{-2}	58.4	66.6	63.1	62.4	84.8	89.2
	$J_s > 2.5$ A m^{-2}	108.6	113.1	115.9	109.4	109.5	131.6

The elemental compositions of the AgAu alloy nanoparticles were then quantified by XPS measurements. Figure 7.2 depicts the survey profiles for the (left

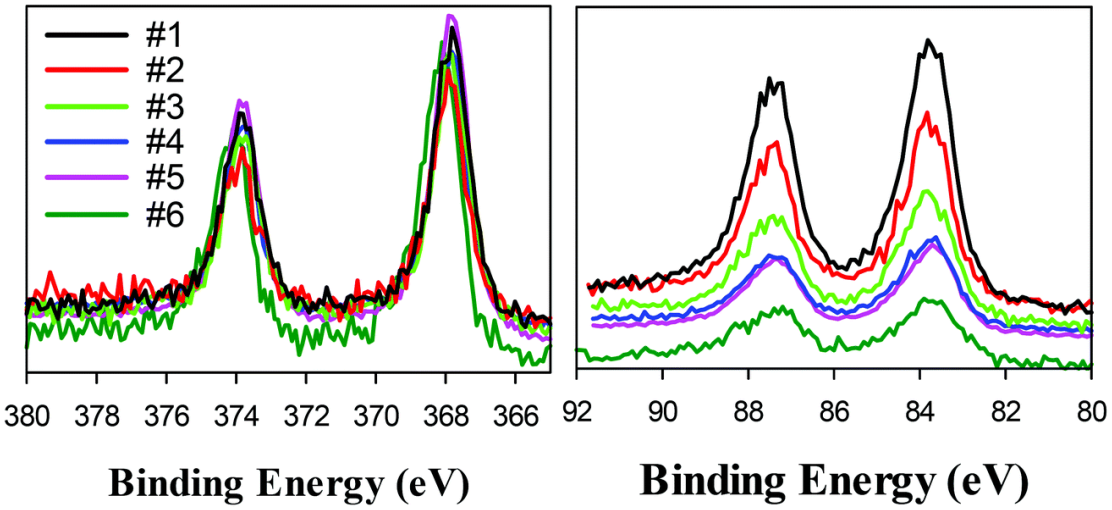

Figure 7.2. XPS spectra of the (left panel) Ag 3d and (right panel) Au 4f electrons of the six AgAu alloy nanoparticles.

panel) Ag 3d and (right panel) Au 4f electrons of the six nanoparticle samples. It can be seen that the binding energies of the Ag 3d electrons for all samples were rather consistent with a doublet centered at 367.9 and 373.9 eV, suggesting metallic silver in the nanoparticles.[53, 54] Similar behaviors can be observed with the Au 4f electrons where the doublets were centered at 83.8 and 87.4 eV for all samples, in good agreement with Au(0).[55] In addition, based on the ratio of the integrated peak areas of the Ag 3d and Au 4f electrons, the atomic fractions of gold in the alloy nanoparticles were estimated to be (A, #1) 56.5%, (B, #2) 51.5%, (C, #3) 39.2%, (D, #4) 35.5%, (E, #5) 31.2%, and (F, #6) 26.7%, which is consistent with the results from UV-vis spectroscopic measurements (vide infra). The results are also summarized in Table 7.1.

Figure 7.3 shows the UV-vis absorption spectra of the six AgAu alloy nanoparticles. It can be seen that all samples exhibited an exponential decay profile, arising from the so-called Mie scattering of nanosized metal nanoparticles, onto which

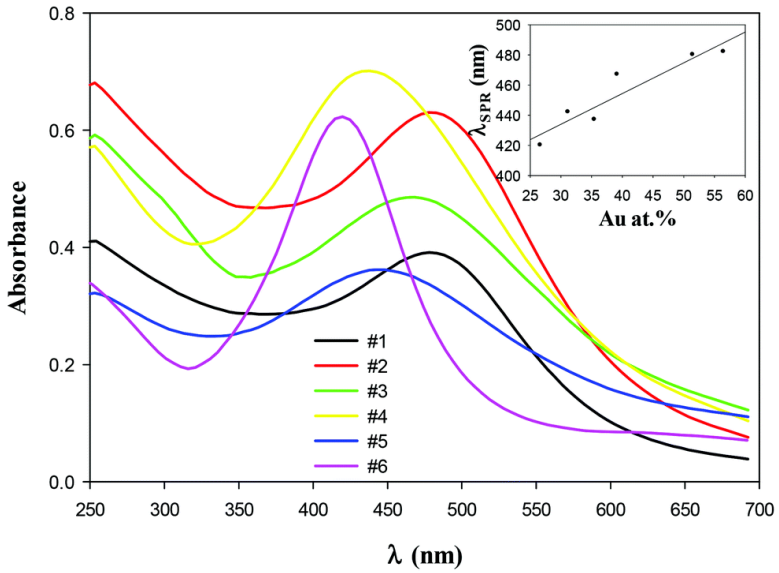

Figure 7.3. UV-vis absorption spectra of the six AgAu alloy nanoparticles in CH_2Cl_2. The inset shows the variation in the corresponding SPR positions with gold contents in the nanoparticles. Symbols are experimental data and line is the linear regression.

is superimposed an apparent absorption peak that is the surface plasmon resonance (SPR) characteristic of the corresponding nanoparticles. It is known that pure gold and silver nanoparticles exhibit well-defined SPR in the visible region at around 520 nm and 400 nm, respectively.[56] For gold and silver alloy nanoparticles, the SPR peak is typically found between these two wavelength positions, varying with the elemental compositions of the nanoparticles.[57] In fact, from the inset of Figure 7.3, it can be seen that the SPR peak positions exhibited an almost linear red-shift with increasing gold contents in the alloy nanoparticles: 482 nm (sample #1, black curve), 480 nm (sample #2, red curve), 464 nm (sample #3, green curve), 436 nm (sample #4, yellow curve), 434 nm (sample #5, blue curve), and 421 nm (sample #6, pink curve). Furthermore, the appearance of a single absorption peak suggests that the AgAu alloy

nanoparticles rather than a simple mixture of gold and silver monometallic nanoparticles were formed. Note that Link and coworkers have reported similar observations, in which the surface plasmon band position of gold-silver alloy nanoparticles were found to shift linearly with the atomic contents.[58]

The successful incorporation of 1-dodecyne ligands onto the surface of AgAu alloy nanoparticles was manifested in FTIR measurements. Figure 7.4 shows the FTIR spectra of the six AgAu alloy nanoparticle samples (solid curves). The most significant observation is the disappearance of the ≡C–H vibrational stretch at 3314 cm^{-1} which is well-defined with monomeric alkynes (dashed curve), suggesting the ready cleavage of the ≡C–H bonds upon the self-assembly of the ligands onto the AgAu alloy

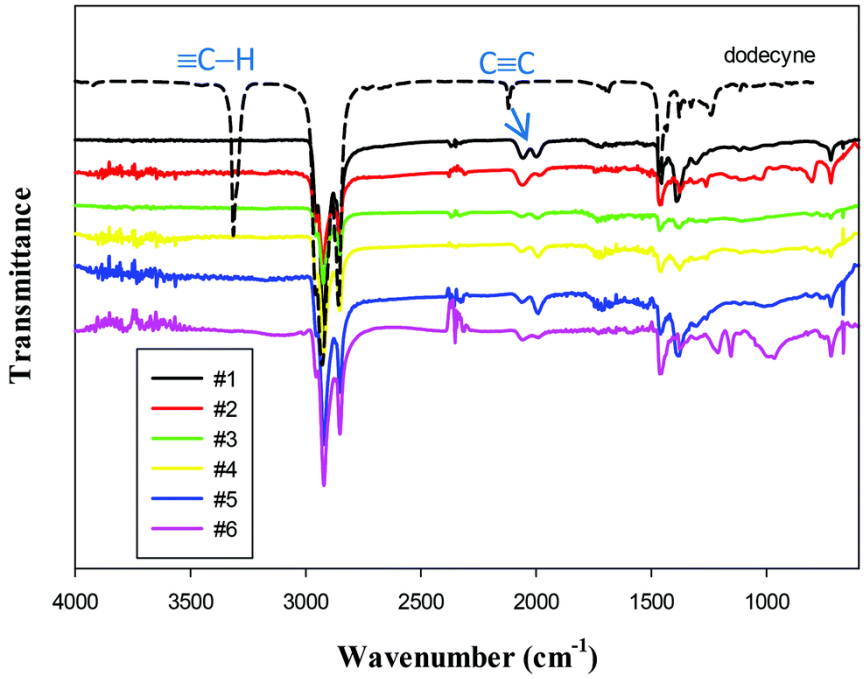

Figure 7.4. FTIR spectra of AgAu nanoparticles at varied atomic compositions (solid curves). The spectrum for the 1-dodecyne monomers is also included as the dashed curve.

nanoparticle surface. In addition, the vanished ≡C−H vibrational stretch also indicates that the nanoparticles were free of excessive monomeric ligands. Furthermore, the C≡C stretch, which appeared at 2119 cm^{-1} for the monomeric ligands (dashed curve), was found to red-shift and split into two bands at around 1990 cm^{-1} and 2060 cm^{-1}. This may be ascribed to the formation of the M(Ag/Au)−acetylide/M(Ag/Au)−vinylidene (M(Ag/Au)−C≡C/M(Ag/Au)=C=C) interfacial bonds and the resulted intraparticle charge delocalization due to the conjugated metal−ligand interface such that the particle-bound acetylene moieties behaved analogously to diacetylene derivatives (C≡C−C≡C). Similar behaviors have also been observed previously with nanoparticles functionalized with other acetylene derivatives.[44, 59, 60]

The electrocatalytic activity in oxygen reduction of the six samples prepared above was then examined and compared by electrochemical measurements. Note that before oxygen reduction reaction measurements, the catalysts-modified electrodes were subjected to an electrochemical activation treatment by rapid potential cycling (at 500 mV s^{-1}) between 0 and +1.2 V (vs. RHE) in a nitrogen-saturated 0.1 M NaOH solution until a steady voltammogram was obtained. The adsorption of oxygen was used for the quantitative assessments of the effective electrochemical surface area and the results are summarized in Table 7.1. It can be seen that ECSA exhibited a roughly monotonic decrease with decreasing gold (increasing silver) contents in the AgAu nanoparticles, probably because of the somewhat stronger bonding interactions of alkynes with Ag than with Au,[41, 42] which led to fewer ligands being removed during the electrochemical activation process at higher Ag concentrations. In fact, in

comparison with the geometrical surface area of the nanoparticles (assuming a spherical shape), the fraction of the nanoparticle surface that was electrochemically accessible can be estimated to be (#1) 41.5%, (#2) 41.2%, (#3) 25.9%, (#4) 33.4%, (#5) 21.6%, and (#6) 23.1%. This also implied only partial removal of the alkyne capping ligands from the nanoparticle surface. Similar behaviors have been observed previously.[45]

Figure 7.5 depicts the RRDE voltammograms of a glassy-carbon disk electrode modified with a calculated amount of each sample in an oxygen-saturated 0.1 M NaOH solution at varied rotation rates (from 100 to 2500 rpm). It can be seen that for all samples, apparent cathodic currents at the disk electrode started to emerge at around +0.9 V (vs. RHE) and the currents reached a plateau at sufficiently negative potentials (around +0.6 V vs. RHE), which suggests effective electrochemical activity in oxygen reduction, despite (partial) capping of the metal cores by the organic ligands; and the voltammetric currents increased with increasing electrode rotation rates. Yet, the performance can be seen to vary somewhat with the elemental compositions of the nanoparticle catalysts. For instance, at any given rotation rate, the limiting currents appear to be maximal with sample (D). In fact, at the same catalyst loadings, the limiting currents at +0.50 V at 1600 rpm are (A, #1) 912 μA, (B, #2) 880 μA, (C, #3) 823 μA, (D, #4) 1040 μA, (E, #5) 928 μA, and (F, #6) 634 μA. A similar trend can be seen with the onset potentials (Table 7.1): (A, #1) +0.90 V, (B, #2) 0.90 V, (C, #3) +0.90 V, (D, #4) +0.92 V, (E, #5) +0.91 V, and (F, #6) +0.89 V. Note that in a previous

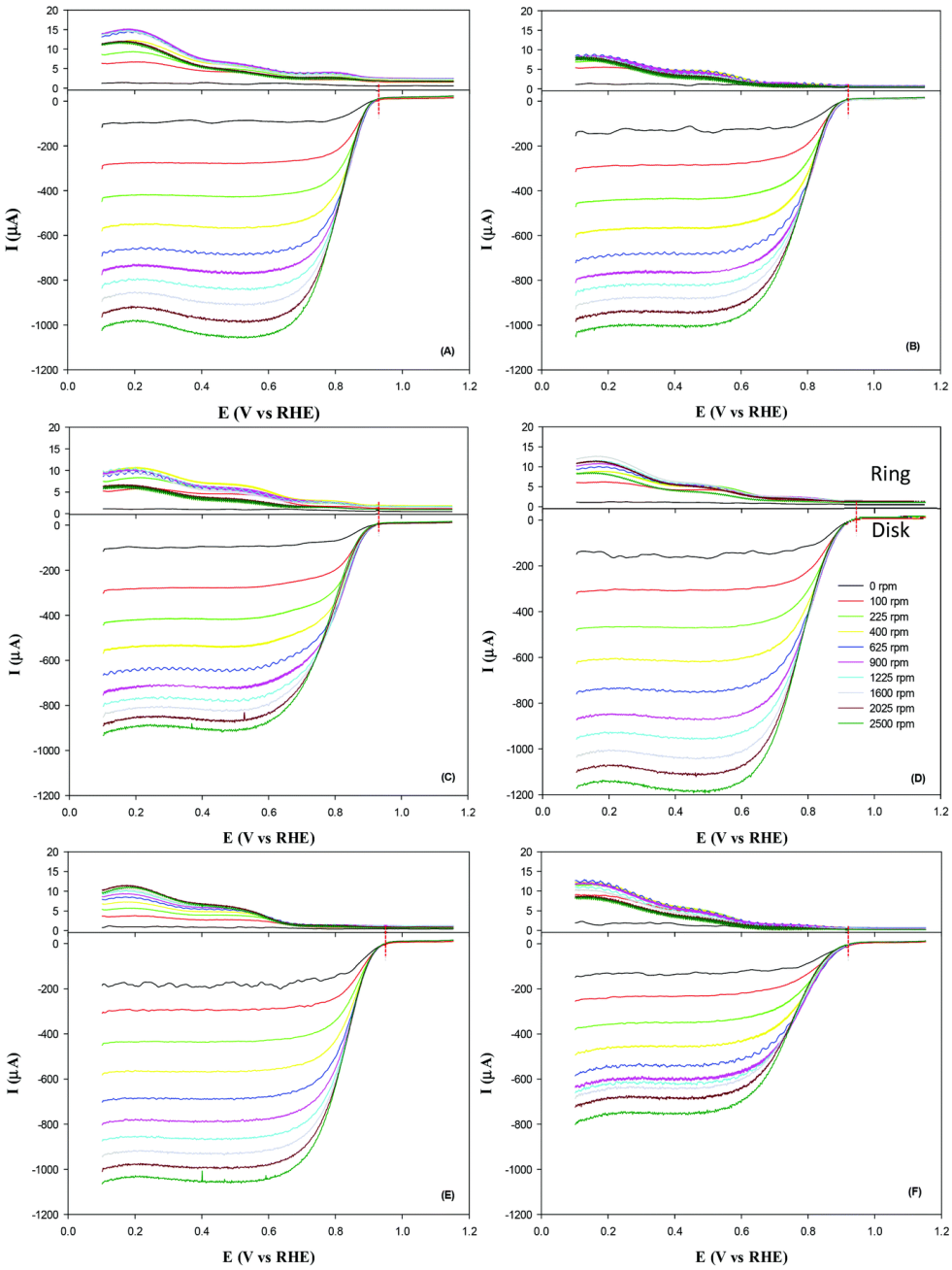

Figure 7.5. RRDE voltammograms of a glassy carbon electron modified with the six AgAu nanoparticles in oxygen-saturated 0.1 M NaOH at varied rotation rates (specified in figure legends). Red vertical bars indicate the onset potentials. The loading of AgAu nanoparticle catalysts was all 6 μg. Disk potential ramp was 10 mV s^{-1} and the ring potential was set to +1.5 V.

study with alkanethiolate-passivated silver nanoparticles of similar size, the onset

potential was found to be markedly more negative at around +0.80 V.[41] These observations suggest that sample (D) (with 35.5 at% of Au) stood out as the best catalyst in the series, which is rather comparable to leading commercial Pt/C catalysts.[61]

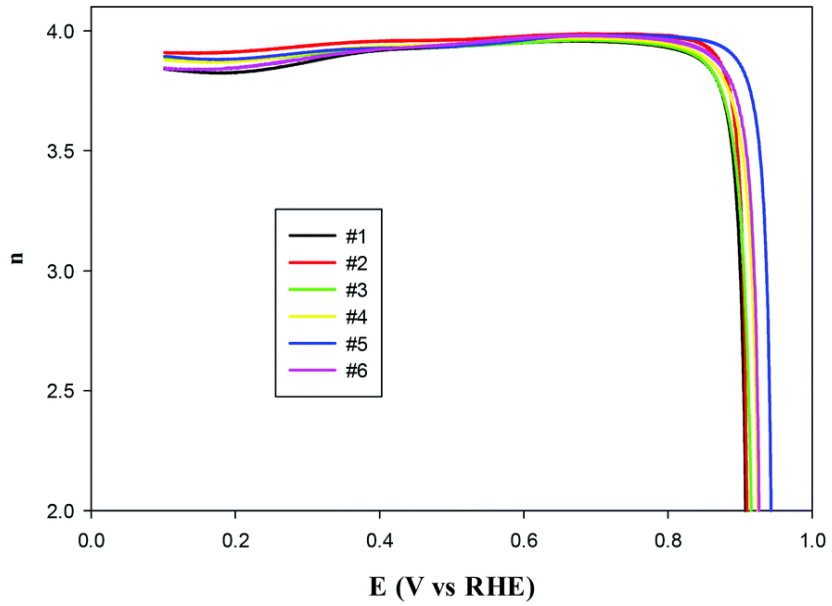

Figure 7.6. Variation in the number of electrons transferred (n) in ORR at AgAu nanoparticles with electrode potentials. Data were calculated from the RRDE voltammograms at 1600 RPM in Figure 7.5.

In addition, the amounts of hydrogen peroxide generated during the oxygen reduction reaction were monitored by collection experiments at the ring electrode which was set to a potential of +1.5 V (vs. RHE). It is clear from Figure 7.5 that the ring currents were about two orders of magnitude smaller than those on disk electrodes at all rotation rates for all samples. In fact, the number of electrons transferred (n) during the oxygen reduction reaction can be estimated by $n = 4I_D/(I_D + I_R/N)$, where I_D and I_R are the disk and ring currents, respectively.[45] By using disk and ring currents

generated at 1600 rpm as an example, *n* values were calculated for all AgAu nanoparticles, as shown in Figure 7.6. Notably, all the six samples exhibited a remarkable ORR performance, with the n values in the narrow range of 3.8 to 4.0 within the wide potential range of +0.85 to +0.10 V, suggesting that oxygen primarily underwent four-electron reduction to hydroxide (OH^-) with minimal amounts of peroxide byproducts. In contrast, in the previous study with hexanethiolate-passivated silver nanoparticles, the n value at similar electrode potentials was much lower at only ca. 2.5, which was improved to a little over 3.0 when ~5 at% Au was incorporated onto the nanoparticles by interfacial engineering.[41] Taken together, these results suggest that alloying of silver nanoparticles with gold is effective in improving the ORR activity which may be optimized at a controlled gold concentration.

In order to quantitatively compare the intrinsic catalytic activity, the electron-transfer kinetics was further analyzed by the Koutecky–Levich method, as shown in Figure 7.7. As the disk voltammetric current (I_D) may include both kinetic (I_k) and diffusion-controlled (I_d) contributions, the Koutecky–Levich equation is expressed as follows:

$$\frac{1}{I_D} = \frac{1}{I_k} + \frac{1}{I_d} = \frac{1}{I_k} + \frac{1}{B\omega^{1/2}} \qquad (7.1a)$$

$$B = 0.62nFAC_O D_O^{2/3} \nu^{-1/6} \qquad (7.1b)$$

$$I_k = nAF\kappa C_O \qquad (7.1c)$$

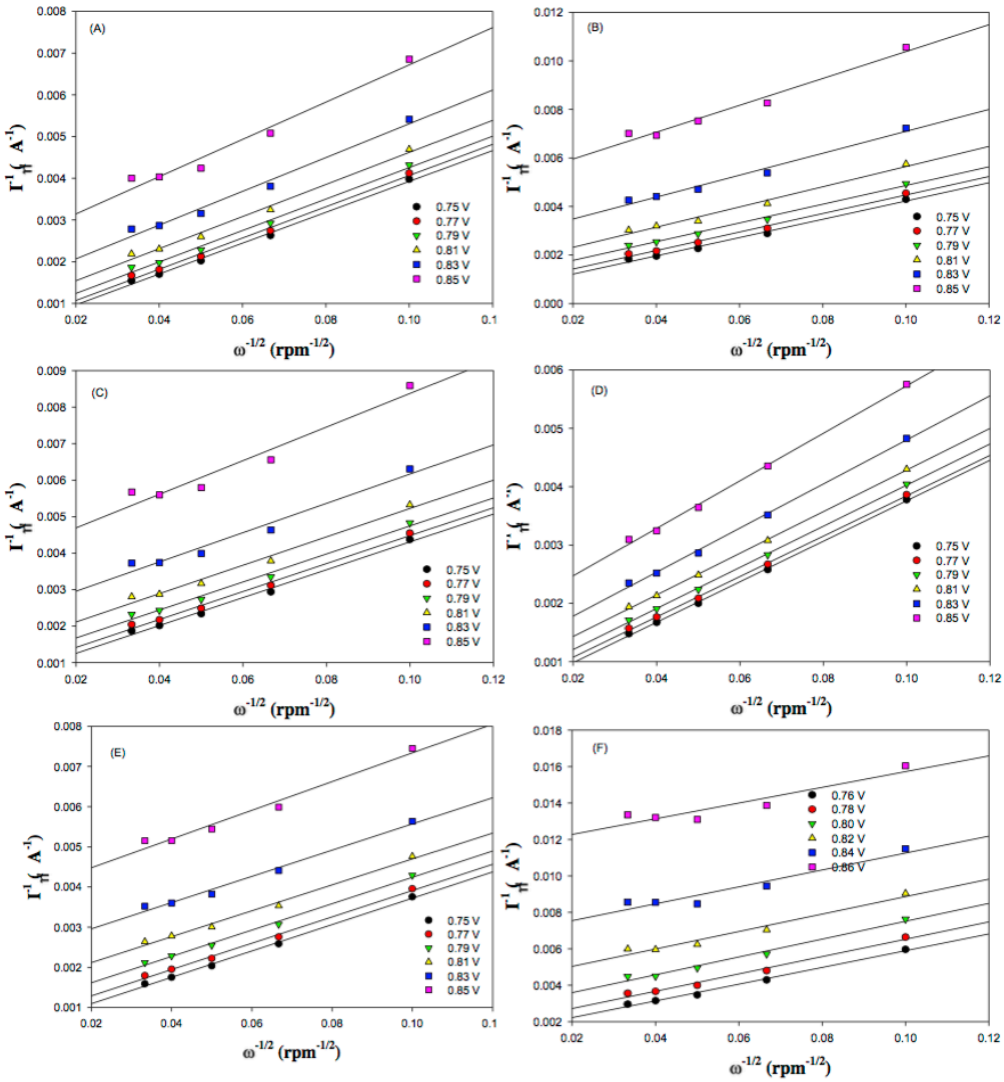

Figure 7.7. Koutecky–Levich plots of the six AgAu nanoparticles in oxygen-saturated 0.1 M NaOH at varied rotation rates (specified in figure legends). Symbols are experimental data from Figure 7.5 and lines are linear regressions.

where ω is the electrode rotation rate, n is the electron-transfer number, F is the Faraday constant (96485 C mol^{-1}), A is the geometric surface area of the electrode, C_O is the oxygen concentration in O_2-saturated solutions (1.26×10^{-6} mol cm^{-3}),[62] D_O is the diffusion coefficient of O_2 in 0.1 M NaOH aqueous solution (1.93×10^{-5} cm^2 s^{-1}),[63]

ν is the kinematic viscosity of the solution (1.09×10^{-2} cm^2 s^{-1}),[64] κ is the electron-transfer rate constant. In fact, all six sample catalysts show good linearity of the Koutecky–Levich plots (I_D^{-1} vs. $\omega^{-1/2}$) within the potential range of +0.75 V to +0.85 V, where contributions from the kinetic component were significant, and the slopes were rather consistent for each nanoparticle suggesting consistent electron transfer kinetics within the electrode potential range. This observation is usually taken as a strong indication of a first-order reaction with respect to dissolved oxygen.

In addition, the kinetic currents might be quantitatively estimated from the y-axis intercepts of the linear regression of the Koutecky–Levich plots, as depicted in the Tafel plot of Figure 7.8. It can be seen that for all nanoparticle catalysts, the area-specific kinetic current density (J_s, I_k normalized by the respective ECSA in Table 7.1) increased as the potential became more negative. Yet, the specific activity varied rather sensitively with the nanoparticle compositions. For instance, at +0.85 V, J_k increases in the order of (#2) 0.81 A m^{-2} < (#3) 1.47 A m^{-2} < (#5) 1.75 A m^{-2} < (#1) 1.80 A m^{-2} < (#6) 1.83 A m^{-2} < (#4) 2.39 A m^{-2}. A similar trend can be seen with the mass-specific activity (J_m, I_k normalized by the nanoparticle mass loading): (#2) 33.5 A g^{-1} < (#6) 38.2 A g^{-1} < (#3) 43.4 A g^{-1} < (#5) 45.2 A g^{-1} < (#1) 75.2 A g^{-1} < (#4) 95.6 A g^{-1}. These data are also listed in Table 7.1. The comparison can be better manifested in the inset of Figure 7.8 where the specific activity exhibited a volcano-shaped variation in the gold contents in the alloy nanoparticles and reached the maximum with sample #4, suggesting that the optimal concentration of Au was about 35.5 at% for ORR. Note that no apparent kinetic current and hence ORR catalytic activity was observed for

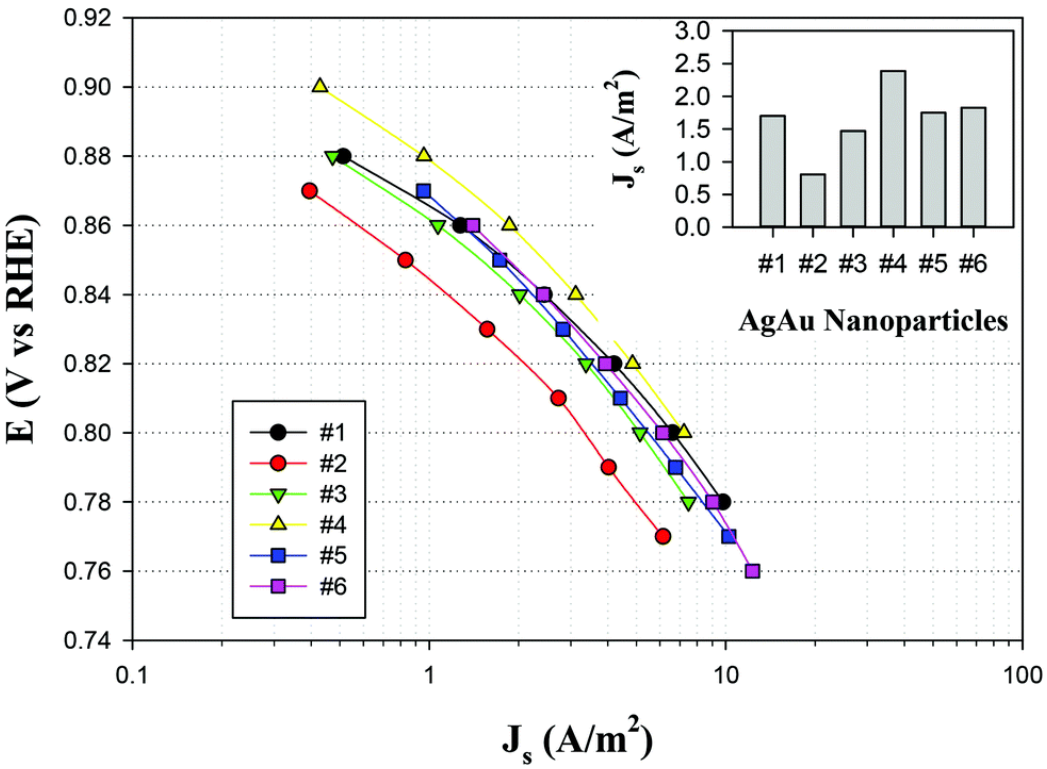

Figure 7.8. Tafel plot of the AgAu nanoparticles in oxygen reduction. Symbols are experimental data extracted from the y-axis intercepts of the corresponding Koutecky–Levich plots and lines are for eye-guiding only. The inset shows the comparison of the kinetic current density at +0.85 V among the six AgAu nanoparticle samples.

polycrystalline silver electrodes, monometallic Ag nanoparticles or AgAu bimetallic Janus nanoparticles (ca. 5 at% of Au) at the same electrode potential.[41, 65]

Furthermore, the Tafel plots of the six nanoparticle catalysts display two linear segments of different slopes (Table 7.1). One should note that for the oxygen reduction reaction, the Tafel slopes are typically found at 60 mV dec^{-1} or 120 mV dec^{-1}, where the former corresponds to a pseudo two-electron reaction as the rate determining step, and the latter one suggests that the rate determining step is presumed to be a first-electron reduction of oxygen, implying that the subsequent reduction and O–O bond

breaking steps are facile.[66] In the present study, at the kinetic current densities lower than 2.5 A m^{-2} (low overpotential region), linear regressions show that the slopes are all close to 60 mV dec^{-1} except for samples #5 and #6 where the slopes are close to 90 mV dec^{-1}; whereas at kinetic current densities above 2.5 A m^{-2} (high overpotential region), the corresponding slopes were all around 120 mV dec^{-1}. These observations suggest a similar oxygen reduction mechanism for the six AgAu alloy nanoparticles. That is, in the low overpotential region, the reaction rate was mainly controlled by the pseudo two-electron reduction reaction (possibly involving the breaking of the O–O bonds), whereas at high overpotentials the rate determining step was likely the first-electron reduction of oxygen. Such Tafel behaviors have been also observed and reported previously for Pt or Pd catalysts,[67] suggesting that the catalytic mechanism of ORR on AgAu resembles that on Pt or Pd, which involves O–O bond breaking and adsorption of oxygenate intermediates, but is distinctly different from that on pure Ag or Au catalysts, where it could be kinetically favorable for outer-sphere electron transfers.[68]

It is most likely that the improved performance (with onset potentials up to +0.92 V and a remarkable kinetic current density) of AgAu alloy nanoparticles over Ag or Au nanoparticles alone is due to the enhanced surface oxygen absorption. It has been shown by both theoretical calculations and experimental studies that the adsorption energies (AE) of oxygen could be manipulated by metal alloying, where the effect on the AE of oxygen is not linearly dependent on the original AE.[3, 69] In fact, it has been reported by Wang et al. that more O^{2-} species were found on the AgAu alloy

surface than on pure Ag or Au surfaces, and the amount of O^{2-} species varied with different Ag/Au ratios.[70] Therefore, in the present study, it is most likely that the marked enhancement of the ORR performance was due to improved surface oxygen affinity by alloying Ag and Au, leading to a positive shift of the equilibrium potential for the first electron transfer reaction and hence a reduced overpotential and positive shift of the onset potential.[68] Moreover, enhanced absorption of oxygen also facilitates the breaking of the O–O bond, resulting in an increase of kinetic current densities. Nevertheless, the increased surface affinity toward oxygen is at the expense of forming strongly bound O and OH species as a result of water oxidation.[71] If the O and OH species produced during ORR are strongly adsorbed onto the catalyst surface, further reduction of O_2 may be inhibited, since the activation energies for O and OH reduction have been found to be relatively high in the low overpotential region in which fuel cell cathodes would ideally be operated.[2] Thus, an optimal oxygen affinity is required to be strong enough to facilitate the first electron transfer to oxygen, but not too strong to inhibit the release of absorbed OH species. Results presented above show that AgAu alloy nanoparticles with approximately 35.5 at% gold display the optimal oxygen affinity, leading to the highest kinetic current density among the series.

As shown in Table 7.2, the electrocatalytic performance of the AgAu nanoparticles prepared above for ORR remained subpar as compared to that of state-of-the art commercial Pt/C catalysts that typically exhibit an onset potential more positive than +0.96 V, a specific activity (J_s) of ~2 A m^{-2} and a mass activity (J_m) of 160 A g^{-1} even at +0.90 V.[45] However, the ORR activity of the AgAu nanoparticles

in the present study, especially sample #4 (n = 3.8 to 4.0 within the potential range of +0.10 V to +0.85 V, onset potential +0.92 V, J_s = 2.39 A m^{-2}, and J_m = 95.6 A g^{-1} at +0.85 V), was markedly better than, or at least comparable to, that of leading Ag-based electrocatalysts reported in the literature. For instance, Slanac et al. prepared AgPd alloy particles (dia. ~5 nm) by simultaneous reduction of Ag and Pd precursors and found that Ag_4Pd exhibited the best electrocatalytic activity (n = 3.7, onset potential +0.91 V, J_m = 598 A g^{-1} at the potential of +0.72 V) for ORR.[72] In another study, Ag_4Pd alloy particles were prepared by co-reduction of Ag and Pd salts and deposited on multiwalled carbon nanotube (MWCNT) surfaces, which exhibited an onset potential of +0.91 V for ORR, but with a low n number of only 2.25 and a low specific activity of only 0.22 A m^{-2}.[73] In contrast, Jiang et al. reported a rather high ORR activity with Pd@Ag/C hybrids (onset potential +0.93 V, J_s = 32 A m^{-2}, and J_m = 1000 A g^{-1} at +0.85 V). However, the Pd@Ag/C hybrids were synthesized by growing Pd onto the surface of carbon supported Ag nanoparticles, where the catalytic activity was most likely due to Pd on the surface whereas the Ag component was not even involved in the catalytic reaction.[74] In another study, Tsai et al. prepared core–shell–shell Ag–Pt–Ag nanocubes by epitaxial growth. Despite the incorporation of Pt into the alloy structures, the ORR activity was rather modest with n = 3.95, onset potential +0.90 V, and J_m = 1.78 A g^{-1} at +0.85 V.[75]

Table 7.2 Summary of ORR activity of leading Ag-based and Pt/C electrocatalysts for ORR in the literature

	J_s (A/m^2, +0.85 V vs. RHE)	J_m (A/g, +0.85 V vs. RHE)	n	E_{onset} (V vs. RHE)
AgAu Janus nanoparticles[41]			3.36	+0.80
Ag nanoparticle–MWCNTs[76]	~1 (+0.80 V)			+0.81
Ag nanoparticles (15 wt.%)–ECNF[77]			3.9	+0.88
Core–shell–shell Ag–Pt–Ag nanocubes[75]		~1.78	3.95	+0.90
Ag–MnO_x/VC[78]		<125 (+0.82 V)	3.5	+0.92
Ag_4Pd_1/MWCNTs[73]	~0.22		2.25	+0.91
Pd@Ag/C[74]	~32	1000		+0.93
Au@Ag[3]	~1.6			+0.92
Ag_4Pd[72]			3.7	+0.91
Ag nanosheets on Ti/TiO_2 electrode[79]		~0.063		+0.92
Pt/C[45]	2 (+0.90 V)	~160 (+0.90 V)	~4	+0.96

7.5 Conclusions

In summary, 1-dodecyne-capped AgAu alloy nanoparticle samples were successfully prepared by chemical reduction of the metal salt precursors at varied initial feed ratios. TEM measurements showed that the resulting nanoparticles exhibited an average core size within the narrow range of 3 to 5 nm in diameter, and XPS measurements showed that the corresponding gold contents varied from about 25 at% to 55 at%. Consistent results were obtained in UV-vis absorption measurements, where an almost linear red-shift of the plasmon absorption peak positions was observed with increasing Au content. More importantly, electrochemical measurements showed that

the alloy nanoparticles all exhibited apparent electrocatalytic activity for ORR, and the sample with 35.5 at% Au was found to display the best catalytic activity among the series, within the context of onset potential, number of electrons transferred and kinetic current density. Such a performance is likely due to the unique metal–ligand interfacial bonding interactions as well as enhanced metal–oxygen affinity from the alloying effects.

7.6 References

1. Steele, B.C.H. and A. Heinzel, *Materials for fuel-cell technologies.* Nature, 2001. **414**(6861): p. 345-352.
2. Norskov, J.K., et al., *Origin of the Overpotential for Oxygen Reduction at a Fuel-Cell Cathode.* Journal of Physical Chemistry B, 2004. **108**: p. 17886-17892.
3. Yang, C., et al., *Activating Ag by even more inert Au: a peculiar effect on electrocatalysis toward oxygen reduction in alkaline media.* Chem Commun (Camb), 2013. **49**(94): p. 11023-5.
4. Tang, D.P., et al., *Alkaline polymer electrolyte fuel cells: Principle, challenges, and recent progress.* Science China-Chemistry, 2010. **53**(2): p. 357-364.
5. Gasteiger, H.A., et al., *Activity benchmarks and requirements for Pt, Pt-alloy, and non-Pt oxygen reduction catalysts for PEMFCs.* Applied Catalysis B-Environmental, 2005. **56**(1-2): p. 9-35.

6. Toda, T., et al., *Enhancement of the electroreduction of oxygen on Pt alloys with Fe, Ni, and Co.* Journal of the Electrochemical Society, 1999. **146**(10): p. 3750-3756.

7. Liu, Z.C., et al., *Synthesis, dealloying, and ORR electrocatalysis of PDDA-stabilized Cu-rich Pt alloy nanoparticles.* Journal of the Electrochemical Society, 2007. **154**(11): p. B1192-B1199.

8. Stamenkovic, V.R., et al., *Trends in electrocatalysis on extended and nanoscale Pt-bimetallic alloy surfaces.* Nature Materials, 2007. **6**(3): p. 241-247.

9. Gong, K.P., et al., *Nitrogen-Doped Carbon Nanotube Arrays with High Electrocatalytic Activity for Oxygen Reduction.* Science, 2009. **323**(5915): p. 760-764.

10. Li, Y.G., et al., *An oxygen reduction electrocatalyst based on carbon nanotube-graphene complexes.* Nature Nanotechnology, 2012. **7**(6): p. 394-400.

11. Suntivich, J., et al., *Design principles for oxygen-reduction activity on perovskite oxide catalysts for fuel cells and metal-air batteries.* Nature Chemistry, 2011. **3**(7): p. 546-550.

12. Oh, S.H., et al., *Synthesis of a metallic mesoporous pyrochlore as a catalyst for lithium-O-2 batteries.* Nature Chemistry, 2012. **4**(12): p. 1004-1010.

13. Lefevre, M., et al., *Iron-Based Catalysts with Improved Oxygen Reduction Activity in Polymer Electrolyte Fuel Cells.* Science, 2009. **324**(5923): p. 71-74.

14. Deng, D.H., et al., *Iron Encapsulated within Pod-like Carbon Nanotubes for Oxygen Reduction Reaction.* Angewandte Chemie-International Edition, 2013. **52**(1): p. 371-375.

15. Cui, C.H., et al., *Ternary Heterostructured Nanoparticle Tubes: A Dual Catalyst and Its Synergistic Enhancement Effects for O-2/H2O2 Reduction.* Angewandte Chemie-International Edition, 2010. **49**(48): p. 9149-9152.

16. Serov, A. and C. Kwak, *Review of non-platinum anode catalysts for DMFC and PEMFC application.* Applied Catalysis B-Environmental, 2009. **90**(3-4): p. 313-320.

17. Kruusenberg, I., et al., *Non-platinum cathode catalysts for alkaline membrane fuel cells.* International Journal of Hydrogen Energy, 2012. **37**(5): p. 4406-4412.

18. Wang, Y.J., et al., *Alkaline polymer electrolyte membranes for fuel cell applications.* Chemical Society Reviews, 2013. **42**(13): p. 5768-5787.

19. Robertson, N.J., et al., *Tunable High Performance Cross-Linked Alkaline Anion Exchange Membranes for Fuel Cell Applications.* Journal of the American Chemical Society, 2010. **132**(10): p. 3400-3404.

20. Sleightholme, A.E.S., J.R. Varcoe, and A.R. Kucernak, *Oxygen reduction at the silver/hydroxide-exchange membrane interface.* Electrochemistry Communications, 2008. **10**(1): p. 151-155.

21. Guo, J.S., et al., *Improving Oxygen Reduction Reaction Activities on Carbon-Supported Ag Nanoparticles in Alkaline Solutions.* Journal of Physical Chemistry C, 2010. **114**(10): p. 4324-4330.

22. Chatenet, M., et al., *Oxygen reduction on silver catalysts in solutions containing various concentrations of sodium hydroxide - comparison with platinum.* Journal of Applied Electrochemistry, 2002. **32**(10): p. 1131-1140.

23. Seo, M.H., et al., *The graphene-supported Pd and Pt catalysts for highly active oxygen reduction reaction in an alkaline condition.* Electrochemistry Communications, 2011. **13**(2): p. 182-185.

24. Jiang, L., et al., *Oxygen Reduction Reaction on Carbon Supported Pt and Pd in Alkaline Solutions.* Journal of the Electrochemical Society, 2009. **156**(3): p. B370-B376.

25. Lee, Y., A. Loew, and S.H. Sun, *Surface- and Structure-Dependent Catalytic Activity of Au Nanoparticles for Oxygen Reduction Reaction.* Chemistry of Materials, 2010. **22**(3): p. 755-761.

26. Yin, H.J., et al., *Facile Synthesis of Surfactant-Free Au Cluster/Graphene Hybrids for High-Performance Oxygen Reduction Reaction.* Acs Nano, 2012. **6**(9): p. 8288-8297.

27. Asazawa, K., et al., *Study of Anode Catalysts and Fuel Concentration on Direct Hydrazine Alkaline Anion-Exchange Membrane Fuel Cells.* Journal of the Electrochemical Society, 2009. **156**(4): p. B509-B512.

28. Tanaka, H., et al., *The Platinum-free Anionic Fuel Cells for Automotive Applications.* Proton Exchange Membrane Fuel Cells 8, Pts 1 and 2, 2008. **16**(2): p. 459-464.

29. Savadogo, O., et al., *New palladium alloys catalyst for the oxygen reduction reaction in an acid medium.* Electrochemistry Communications, 2004. **6**(2): p. 105-109.

30. Shao, M.H., K. Sasaki, and R.R. Adzic, *Pd-Fe nanoparticles as electrocatalysts for oxygen reduction.* Journal of the American Chemical Society, 2006. **128**(11): p. 3526-3527.

31. Cui, C.H. and S.H. Yu, *Engineering Interface and Surface of Noble Metal Nanoparticle Nanotubes toward Enhanced Catalytic Activity for Fuel Cell Applications.* Accounts of Chemical Research, 2013. **46**(7): p. 1427-1437.

32. Yano, H., et al., *Particle-size effect of nanoscale platinum catalysts in oxygen reduction reaction: an electrochemical and Pt-195 EC-NMR study.* Physical Chemistry Chemical Physics, 2006. **8**(42): p. 4932-4939.

33. Kinoshita, K., *Particle-Size Effects for Oxygen Reduction on Highly Dispersed Platinum in Acid Electrolytes.* Journal of the Electrochemical Society, 1990. **137**(3): p. 845-848.

34. Lim, B., et al., *Pd-Pt Bimetallic Nanodendrites with High Activity for Oxygen Reduction.* Science, 2009. **324**(5932): p. 1302-1305.

35. Chen, Z.W., et al., *Supportless Pt and PtPd nanotubes as electrocatalysts for oxygen-reduction reactions.* Angewandte Chemie-International Edition, 2007. **46**(22): p. 4060-4063.

36. Xiao, L., et al., *Activating Pd by Morphology Tailoring for Oxygen Reduction.* Journal of the American Chemical Society, 2009. **131**(2): p. 602-608.

37. Zhang, J.L., et al., *Controlling the catalytic activity of platinum-monolayer electrocatalysts for oxygen reduction with different substrates.* Angewandte Chemie-International Edition, 2005. **44**(14): p. 2132-2135.

38. Zhang, J.L., et al., *Mixed-metal Pt monolayer electrocatalysts for enhanced oxygen reduction kinetics.* Journal of the American Chemical Society, 2005. **127**(36): p. 12480-12481.

39. Greeley, J., et al., *Alloys of platinum and early transition metals as oxygen reduction electrocatalysts.* Nature Chemistry, 2009. **1**(7): p. 552-556.

40. Bing, Y.H., et al., *Nanostructured Pt-alloy electrocatalysts for PEM fuel cell oxygen reduction reaction.* Chemical Society Reviews, 2010. **39**(6): p. 2184-2202.

41. Song, Y., K. Liu, and S. Chen, *AgAu bimetallic Janus nanoparticles and their electrocatalytic activity for oxygen reduction in alkaline media.* Langmuir, 2012. **28**(49): p. 17143-52.

42. He, G.Q., et al., *Electrocatalytic Activity of Organically Functionalized Silver Nanoparticles in Oxygen Reduction.* Science of Advanced Materials, 2013. **5**(11): p. 1727-1736.

43. Liu, K., Y. Song, and S.W. Chen, *Electrocatalytic activities of alkyne-functionalized copper nanoparticles in oxygen reduction in alkaline media.* Journal of Power Sources, 2014. **268**: p. 469-475.

44. Liu, K., et al., *Platinum nanoparticles functionalized with acetylene derivatives: Electronic conductivity and electrocatalytic activity in oxygen reduction.* Journal of Electroanalytical Chemistry, 2013. **688**: p. 143-150.

45. Zhou, Z.Y., et al., *Enhancement of the electrocatalytic activity of Pt nanoparticles in oxygen reduction by chlorophenyl functionalization.* Chemical Communications, 2012. **48**(28): p. 3391-3393.

46. Gloaguen, F., et al., *Kinetic-Study of Electrochemical Reactions at Catalyst-Recast Ionomer Interfaces from Thin Active Layer Modeling.* Journal of Applied Electrochemistry, 1994. **24**(9): p. 863-869.

47. Markovic, N.M., et al., *Oxygen Reduction Reaction on Pt and Pt Bimetallic Surfaces: A Selective Review.* Fuel Cells, 2001. **1**(2): p. 105-116.

48. Wang, R.Y., et al., *Nanoporous surface alloys as highly active and durable oxygen reduction reaction electrocatalysts.* Energy & Environmental Science, 2012. **5**(1): p. 5281-5286.

49. Shao, M.H., et al., *Structural dependence of oxygen reduction reaction on palladium nanocrystals.* Chemical Communications, 2011. **47**(23): p. 6566-6568.

50. Spanos, I., et al., *PtxCo1-x alloy NPs prepared by colloidal tool-box synthesis: The effect of de-alloying on the oxygen reduction reaction activity.* International Journal of Hydrogen Energy, 2014. **39**(17): p. 9143-9148.

51. Wang, C., N.M. Markovic, and V.R. Stamenkovic, *Advanced Platinum Alloy Electrocatalysts for the Oxygen Reduction Reaction.* Acs Catalysis, 2012. **2**(5): p. 891-898.

52. Tang, Q.W., et al., *Effect of Surface Manganese Valence of Manganese Oxides on the Activity of the Oxygen Reduction Reaction in Alkaline Media.* Acs Catalysis, 2014. **4**(2): p. 457-463.

53. Sun, X.P., S.J. Dong, and E.K. Wang, *One-step preparation and characterization of poly(propyleneimine) dendrimer-protected silver nanoclusters.* Macromolecules, 2004. **37**(19): p. 7105-7108.

54. Wang, X.C., et al., *A robust three-dimensional mesoporous Ag/TiO2 nanohybrid film.* Chemical Communications, 2005(17): p. 2262-2264.

55. Johansson, G., et al., *Calibration of electron spectra.* Journal of Electron Spectroscopy and Related Phenomena, 1973. **2**(3): p. 295-317.

56. Creighton, J.A. and D.G. Eadon, *Ultraviolet Visible Absorption-Spectra of the Colloidal Metallic Elements.* Journal of the Chemical Society-Faraday Transactions, 1991. **87**(24): p. 3881-3891.

57. McFarland, A.D. and R.P. Van Duyne, *Single silver nanoparticles as real-time optical sensors with zeptomole sensitivity.* Nano Letters, 2003. **3**(8): p. 1057-1062.

58. Link, S., Z.L. Wang, and M.A. El-Sayed, *Alloy formation of gold-silver nanoparticles and the dependence of the plasmon absorption on their composition.* Journal of Physical Chemistry B, 1999. **103**(18): p. 3529-3533.

59. Chen, W., et al., *Alkyne-Protected Ruthenium Nanoparticles.* Journal of Physical Chemistry C, 2010. **114**(42): p. 18146-18152.

60. Kang, X., et al., *Alkyne-functionalized ruthenium nanoparticles: ruthenium-vinylidene bonds at the metal-ligand interface.* J Am Chem Soc, 2012. **134**(3): p. 1412-1415.

61. He, G.Q., et al., *Oxygen Reduction Catalyzed by Platinum Nanoparticles Supported on Graphene Quantum Dots.* Acs Catalysis, 2013. **3**(5): p. 831-838.

62. Schumpe, A., I. Adler, and W.D. Deckwer, *Solubility of Oxygen in Electrolyte-Solutions.* Biotechnology and Bioengineering, 1978. **20**(1): p. 145-150.

63. Anastasijevic, N.A., Z.M. Dimitrijevic, and R.R. Adzic, *Oxygen Reduction on a Ruthenium Electrode in Acid Electrolytes.* Electrochimica Acta, 1986. **31**(9): p. 1125-1130.

64. Markovic, N.M., et al., *Oxygen reduction reaction on Pt(111): effects of bromide.* Journal of Electroanalytical Chemistry, 1999. **467**(1-2): p. 157-163.

65. Singh, P. and D.A. Buttry, *Comparison of Oxygen Reduction Reaction at Silver Nanoparticles and Polycrystalline Silver Electrodes in Alkaline Solution.* Journal of Physical Chemistry C, 2012. **116**(19): p. 10656-10663.

66. Zhang, J., *PEM fuel cell electrocatalysts and catalyst layers: fundamentals and applications*. 2008, London: Springer.

67. Vinayan, B.P., R. Nagar, and S. Ramaprabhu, *Synthesis and investigation of mechanism of platinum-graphene electrocatalysts by novel co-reduction*

techniques for proton exchange membrane fuel cell applications. Journal of Materials Chemistry, 2012. **22**(48): p. 25325-25334.

68. Quaino, P., et al., *Why is Gold such a Good Catalyst for Oxygen Reduction in Alkaline Media?* Angewandte Chemie-International Edition, 2012. **51**(52): p. 12997-13000.

69. Suo, Y.G., L. Zhuang, and J.T. Lu, *First-principles considerations in the design of Pd-alloy catalysts for oxygen reduction.* Angewandte Chemie-International Edition, 2007. **46**(16): p. 2862-2864.

70. Wang, A.Q., et al., *A novel efficient Au-Ag alloy catalyst system: preparation, activity, and characterization.* Journal of Catalysis, 2005. **233**(1): p. 186-197.

71. Anderson, A.B., *O-2 reduction and CO oxidation at the Pt-electrolyte interface. The role of H2O and OH adsorption bond strengths.* Electrochimica Acta, 2002. **47**(22-23): p. 3759-3763.

72. Slanac, D.A., et al., *Atomic Ensemble and Electronic Effects in Ag-Rich AgPd Nanoalloy Catalysts for Oxygen Reduction in Alkaline Media.* Journal of the American Chemical Society, 2012. **134**(23): p. 9812-9819.

73. Lee, C.L., et al., *Carbon nanotubes-supported colloidal Ag-Pd nanoparticles as electrocatalysts toward oxygen reduction reaction in alkaline electrolyte.* International Journal of Hydrogen Energy, 2011. **36**(4): p. 2759-2764.

74. Jiang, L., et al., *A highly active Pd coated Ag electrocatalyst for oxygen reduction reactions in alkaline media.* Electrochimica Acta, 2010. **55**(15): p. 4506-4511.

75. Tsai, Y.L., et al., *Preparation and cyclic voltammetric dissolution of core-shell-shell Ag-Pt-Ag nanocubes and their comparison in oxygen reduction reaction in alkaline media.* International Journal of Hydrogen Energy, 2014. **39**(11): p. 5528-5536.

76. Cheng, Y.H., et al., *Modified multi-walled carbon nanotube/Ag nanoparticle composite catalyst for the oxygen reduction reaction in alkaline solution.* Electrochimica Acta, 2013. **111**: p. 635-641.

77. Lai, C.L., et al., *Lignin-derived electrospun carbon nanofiber mats with supercritically deposited Ag nanoparticles for oxygen reduction reaction in alkaline fuel cells.* Electrochimica Acta, 2014. **130**: p. 431-438.

78. Slanac, D.A., et al., *Bifunctional Catalysts for Alkaline Oxygen Reduction Reaction via Promotion of Ligand and Ensemble Effects at Ag/MnOx Nanodomains.* Journal of Physical Chemistry C, 2012. **116**(20): p. 11032-11039.

79. Lee, C.L. and C.C. Syu, *Electrochemical growth and oxygen reduction property of Ag nanosheet arrays on a Ti/TiO2 electrode.* International Journal of Hydrogen Energy, 2011. **36**(23): p. 15068-15074.